Measuring the Polarization of the Cosmic Microwave Background with Bicep3

Thesis by
Howard Hui

In Partial Fulfillment of the Requirements for the
Degree of
Doctor of Philosophy

Caltech

CALIFORNIA INSTITUTE OF TECHNOLOGY
Pasadena, California

2018
Defended May 25th, 2018

© 2018

Howard Hui
ORCID: 0000-0001-5812-1903

ACKNOWLEDGEMENTS

ABSTRACT

Inflation, a period of accelerated expansion in the early Universe, is postulated to answer the horizon, flatness and monopole problems in the standard model of the Universe. This inflationary scenario generically predicts the existence of primordial gravitational waves, which would leave an unique B-mode polarization pattern in the Cosmic Microwave Background. Detection of the primordial B modes at degree angular scales would be a direct evidence for inflation; and the amplitude, parametrized by the tensor-to-scalar ratio r, would allow us to probe the energy scale at 10^{-35} second after the Big Bang.

The BICEP/*Keck Array* experiment is a series of telescopes located at the Amundsen-Scott South Pole Station designed to measure the CMB polarization at degree angular scales. The latest result in BICEP/*Keck Array*, using data collected up to 2015, and combined with other external data, set upper limits on $r < 0.06$ at 95% confidence. BICEP3 is the latest addition in the experiment, deployed to South Pole in 2015, and started science observation in 2016. It is a 520 mm aperture, compact two-lens refracting telescope at 95 GHz. With 2500 detectors, it achieved instantaneous sensitivity of 9.1 $\mu K_{cmb}\sqrt{s}$ and 7.3 $\mu K_{cmb}\sqrt{s}$ for 2016 and 2017, respectively. After two year of observations, BICEP3 is estimated to reach a map depth of 3.8 μK_{cmb}-arcmin. This is the most sensitive polarization measurement at 95 GHz to date.

This dissertation provides an overview of the BICEP3 instrument design. In particular, the performance of the sub-Kelvin focal plane structure, antenna-coupled transition edge sensor and time domain multiplexing SQUID readout system. We discuss various calibration methods used to probe instrument sensitivity and systematics. Finally, we review the analysis pipeline, and some preliminary results from BICEP3.

PUBLISHED CONTENT AND CONTRIBUTIONS

H.H. is the core member in the Bicep/*Keck Array* collaboration, participated in the construction, calibration, and deployment for *Keck Array*. He led the design, construction, testing, and deployment of the Bicep3 receiver, focusing on sub-Kelvin stages, readout and detectors. He led the initial analysis in Bicep3 with J. Willmert, J.H. Kang, and K. Lau.

[1] P. Ade *et al.*, "Improved constraints on cosmology and foregrounds from bicep2 and keck array cosmic microwave background data with inclusion of 95 ghz band," *Phys. Rev. Lett*, vol. 116, p. 031 302, 2016.

[2] P. Ade, Z. Ahmed, R. Aikin, K. D. Alexander, D. Barkats, S. Benton, C. A. Bischoff, J. Bock, R. Bowens-Rubin, J. Brevik, *et al.*, "Bicep2/keck array. vii. matrix based e/b separation applied to bicep2 and the keck array," *The Astrophysical Journal*, vol. 825, no. 1, p. 66, 2016.

[3] J. Grayson, P. Ade, Z. Ahmed, K. D. Alexander, M. Amiri, D. Barkats, S. Benton, C. A. Bischoff, J. Bock, H. Boenish, *et al.*, "Bicep3 performance overview and planned keck array upgrade," in *Millimeter, Submillimeter, and Far-Infrared Detectors and Instrumentation for Astronomy VIII*, International Society for Optics and Photonics, vol. 9914, 2016, 99140S.

[4] H. Hui, P. Ade, Z. Ahmed, K. D. Alexander, M. Amiri, D. Barkats, S. Benton, C. A. Bischoff, J. Bock, H. Boenish, *et al.*, "Bicep3 focal plane design and detector performance," in *Millimeter, Submillimeter, and Far-Infrared Detectors and Instrumentation for Astronomy VIII*, International Society for Optics and Photonics, vol. 9914, 2016, 99140T.

[5] K. S. Karkare, P. Ade, Z. Ahmed, K. D. Alexander, M. Amiri, D. Barkats, S. Benton, C. A. Bischoff, J. Bock, H. Boenish, *et al.*, "Optical characterization of the bicep3 cmb polarimeter at the south pole," in *Millimeter, Submillimeter, and Far-Infrared Detectors and Instrumentation for Astronomy VIII*, International Society for Optics and Photonics, vol. 9914, 2016, p. 991 430.

[6] W. Wu, P. Ade, Z. Ahmed, K. Alexander, M. Amiri, D. Barkats, S. Benton, C. Bischoff, J. Bock, R. Bowens-Rubin, *et al.*, "Initial performance of bicep3: A degree angular scale 95 ghz band polarimeter," *Journal of Low Temperature Physics*, vol. 184, no. 3-4, pp. 765–771, 2016.

[7] P. A. Ade, N. Aghanim, Z. Ahmed, R. Aikin, K. D. Alexander, M. Arnaud, J. Aumont, C. Baccigalupi, A. J. Banday, D. Barkats, *et al.*, "Joint analysis of bicep2/keck array and planck data," *Physical review letters*, vol. 114, no. 10, p. 101 301, 2015.

[8] P. A. Ade, Z. Ahmed, R. Aikin, K. D. Alexander, D. Barkats, S. Benton, C. A. Bischoff, J. Bock, J. Brevik, I. Buder, *et al.*, "Bicep2/keck array v: Measurements of b-mode polarization at degree angular scales and 150 ghz by the keck array," *The Astrophysical Journal*, vol. 811, no. 2, p. 126, 2015.

[9] P. A. Ade, R. Aikin, M. Amiri, D. Barkats, S. Benton, C. A. Bischoff, J. Bock, J. Bonetti, J. Brevik, I. Buder, *et al.*, "Antenna-coupled tes bolometers used in bicep2, keck array, and spider," *The Astrophysical Journal*, vol. 812, no. 2, p. 176, 2015.

[10] P. A. Ade, R. Aikin, D. Barkats, S. Benton, C. A. Bischoff, J. Bock, K. Bradford, J. Brevik, I. Buder, E. Bullock, *et al.*, "Bicep2/keck array. iv. optical characterization and performance of the bicep2 and keck array experiments," *The Astrophysical Journal*, vol. 806, no. 2, p. 206, 2015.

[11] Z. Ahmed, M. Amiri, S. Benton, J. Bock, R. Bowens-Rubin, I. Buder, E. Bullock, J. Connors, J. Filippini, J. Grayson, *et al.*, "Bicep3: A 95ghz refracting telescope for degree-scale cmb polarization," in *Millimeter, Submillimeter, and Far-Infrared Detectors and Instrumentation for Astronomy VII*, International Society for Optics and Photonics, vol. 9153, 2014, 91531N.

[12] K. Karkare, P. A. Ade, Z. Ahmed, R. Aikin, K. Alexander, M. Amiri, D. Barkats, S. Benton, C. Bischoff, J. Bock, *et al.*, "Keck array and bicep3: Spectral characterization of 5000+ detectors," in *Millimeter, Submillimeter, and Far-Infrared Detectors and Instrumentation for Astronomy VII*, International Society for Optics and Photonics, vol. 9153, 2014, 91533B.

[13] R. O'Brient, P. Ade, Z. Ahmed, R. Aikin, M. Amiri, S. Benton, C. Bischoff, J. Bock, J. Bonetti, J. Brevik, *et al.*, "Antenna-coupled tes bolometers for the keck array, spider, and polar-1," in *Millimeter, Submillimeter, and Far-Infrared Detectors and Instrumentation for Astronomy VI*, International Society for Optics and Photonics, vol. 8452, 2012, 84521G.

[14] R. Ogburn, P. Ade, R. Aikin, M. Amiri, S. Benton, C. A. Bischoff, J. Bock, J. Bonetti, J. Brevik, E. Bullock, *et al.*, "Bicep2 and keck array operational overview and status of observations," in *Millimeter, Submillimeter, and Far-Infrared Detectors and Instrumentation for Astronomy VI*, International Society for Optics and Photonics, vol. 8452, 2012, 84521A.

TABLE OF CONTENTS

LIST OF ILLUSTRATIONS

LIST OF TABLES

Chapter 1

INTRODUCTION AND MOTIVATION

1.1   The Standard model of cosmology

The standard model of cosmology, also known as the ΛCDM cosmology. The energy density of the present universe primarily of a Cosmological Constant (Λ) driving an accelerated expansion of the universe and the Cold Dark Matter (CDM). The equation governing the model are built around the observation that the distribution of the energy density in the universe appears to be homogeneous and isotropic, which means that the Universe is the same at every point in space.

We describe an isotropic and homogeneous universe using the Friedmann-Robinson-Walker Metric [1]:

$$ds^2 = dt^2 - a\,(t)^2 \left[\frac{dr^2}{1 - Kr^2} + r^2 d\Omega^2 \right] \tag{1.1}$$

where K is the geometric curvature, $d\Omega = d\theta^2 + \sin^2 \theta d\theta$ is the volume element, r is the radial coordinate, t is the temporal coordinate, and $a\,(t)$ is the scale factor of the universe.

According to the measurement of the Cosmic Microwave Background (CMB), the geometry of the Universe is flat, $K = 0$ [2]. A positive curvature Universe has $K = 1$ and a negative curvature Universe has $K = -1$.

The expansion rate of the Universe $a\,(t)$ is changing over time, and so it is often useful to work in conformal time, τ.

$$\tau = \int \frac{dt}{a\,(t)} \tag{1.2}$$

and Equation 1.1 becomes:

$$ds^2 = a\,(\tau)^2 \left[d\tau^2 - \frac{dr^2}{1 - Kr^2} + r^2 d\Omega^2 \right] \tag{1.3}$$

Furthermore, Einstein's equation of general relativity relates the geometry of space-time to the energy and momentum:

$$G_{\mu\nu} \equiv R_{\mu\nu} - \frac{1}{2}Rg_{\mu\nu} = 8\pi G T_{\mu\nu} \tag{1.4}$$

here $G_{\mu\nu}$ is the Einstein tensor, $R_{\mu\nu}$ is the Ricci curvature tensor, R is the Ricci scalar. Left-hand side of equation 1.4 describes the geometry with metric $g_{\mu\nu}$, and the right-hand side of the equation is the energy-momentum tensor.

Applying the FRW metric to the Einstein equation, we can derive the Friedmann equation:

$$\left(\frac{\dot{a}}{a}\right)^2 = \frac{8\pi G\rho}{3} - \frac{K}{a^2} \tag{1.5}$$

where ρ is the energy density in the energy-momentum tensor and $K = 0$ describes a flat Universe.

From energy conservation $\nabla_\mu T_0^\mu = 0$, we calculate

$$\dot{\rho} = -3\frac{\dot{a}}{a}(\rho + p) \tag{1.6}$$

where p is the pressure. Combining the metric and the energy conservation, we form the acceleration equation:

$$\frac{\ddot{a}}{a} = -\frac{4\pi}{3}(\rho + 3p) \tag{1.7}$$

Given the Friedmann equation and the energy conservation relation, it leads to the equation of state: $p = \omega\rho$ relating the pressure and energy density, which related the energy density and the scale factor a from Equation 1.6.

$$\rho = \rho_0 a^{-3(\omega+1)} \tag{1.8}$$

We have $\omega = 0$ for non-relativistic matter, $\omega = 1/3$ for radiation, and a cosmological constant has $\omega = -1$.

Inserting these parameters back into the Friedmann equation, it shows the scale factor of the Universe a is proportion to:

$$a_\gamma(t) \propto t^{1/2} \tag{1.9}$$

$$a_M(t) \propto t^{2/3} \tag{1.10}$$

$$a_\Lambda(t) \propto \exp\left(\sqrt{\frac{\Lambda}{3}}t\right) \tag{1.11}$$

for a universe is dominated by radiation, matter and dark energy Λ respectively.

In order to derive the history of expansion of the Universe, we need to know what the universe is composed of today and how their densities change as a function of time. Planck Collaboration [3] reports that the universe is composed $\sim 70\%$ dark energy Λ and $\sim 30\%$ matter, which includes dark matter and baryons.

The energy density of radiation is proportional to a^{-4}, unlike matter which scales as a^{-3} and dark energy's contribution is constant. Because we know the energy densities of the cosmological fluids today, we can calculate that the Universe went through the epochs of radiation domination, matter domination, and currently dark energy dominated period.

We can define the Hubble parameter, which describes the rate of expansion as:

$$H(t) = \frac{da/dt}{a} = \frac{\dot{a}(t)}{a(t)} \tag{1.12}$$

The Friedmann equation relates the rate of change of the scale factor to the total energy density of the Universe and the geometry K, which we can use to define a critical energy density, ρ_c for a flat Universe ($K = 0$):

$$\rho_c = \frac{3H^2}{8\pi G} \tag{1.13}$$

We can define the total energy density as:

$$\Omega_{total} = \frac{\rho}{\rho_c} \tag{1.14}$$

and separate the energy density of the Universe down into:

$$\Omega_{total} = \Omega_\gamma + \Omega_m + \Omega_\Lambda + \Omega_K \tag{1.15}$$

The Hubble parameter can be related to the energy density today from each components as:

$$H(a)^2 = H_0^2 \left[\Omega_{0,m} a^{-3} + \Omega_{0,\gamma} a^{-4} + \Omega_{0,\Lambda} \right] \tag{1.16}$$

as $\Omega_{0,K} = 0$ in a flat Universe. We often write the equation in terms of redshift z:

$$a(t) = \frac{1}{1+z} \qquad (1.17)$$

and set the scale factor at present time, $a(t_0) = 1$. Then equation 1.16 becomes:

$$H(z)^2 = H_0^2 \left[\Omega_{0,m}(1+z)^3 + \Omega_{0,\gamma}(1+z)^4 + \Omega_{0,\Lambda} \right] \qquad (1.18)$$

This shows the mathematical description of the expanding Universe.

1.2 The Cosmic Microwave Background

According to the Hot Big Bang model, the early Universe had a temperature and density much higher than today. At a time about 380,000 years after the Big Bang; a plasma of protons, electrons and photons existed in equilibrium, and formed a tightly coupled baryon-photon fluid through Compton scattering. As the Universe cooled, it eventually reached a temperature that allowed protons and electrons to combine to form neutral hydrogen and helium, an epoch known as *recombination*.

During recombination, the density of free electron decreased, and the mean free path of photons increased [4]. Finally, the photons able to freely stream through the Universe, forming the surface of last scattering. The photons from this surface travel freely through the Universe and are known as the Cosmic Microwave Background (CMB).

The surface of last scattering is at a redshift of $z_{\text{rec}} = 1100$. The temperature of the CMB photons observed today cooled due to the expansion of the Universe. The CMB was first detected by Penzias and Wilson in 1965, and later the FIRAS experiment measured to a extremely well-described 2.725 K blackbody spectrum, which established the Big Bang expansion to be the standard model of cosmology (Figure 1.1).

Observation of the CMB indicate that the temperature is nearly identically same in all directions on the sky, and it is uniform to 1 part in 10,000.

Figure 1.2 shows the temperature anisotropy of the CMB measured by *Planck*. The hot and cold spots on the temperature anisotropy map corresponds to the over- and under-dense regions of photon-baryon fluid.

The temperature anisotropy of the CMB can be described in terms of spherical harmonics, Y_{lm}:
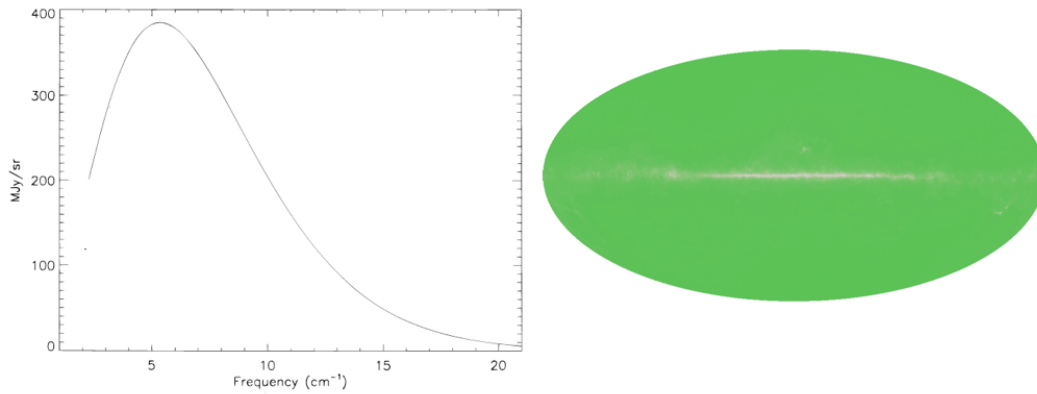
Figure 1.1: Full sky map and the spectral distribution of the CMB [5].
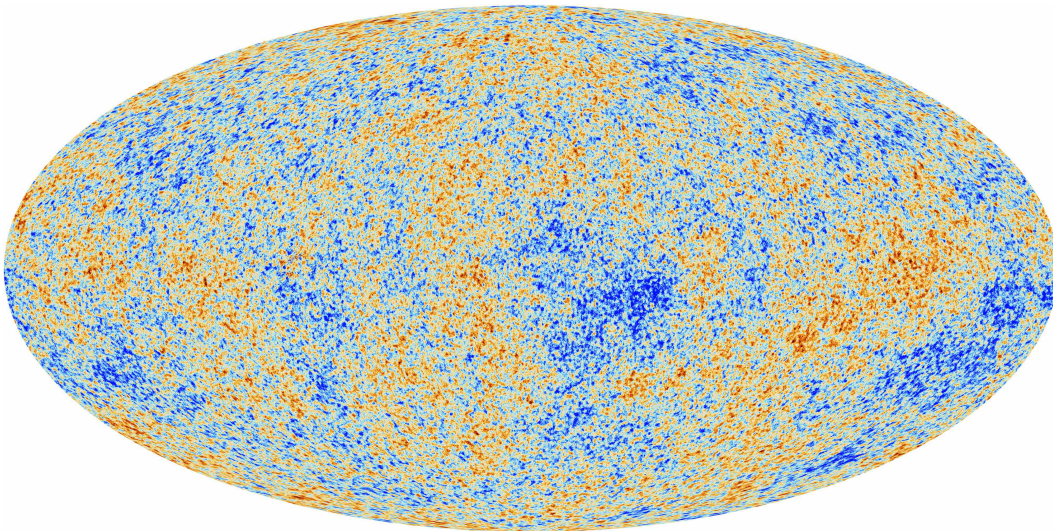
Figure 1.2: Full sky temperature anisotropy of the CMB measured by *Planck* [6].

$$\Delta T\left(\theta, \phi\right) = \sum_{l=1}^{\infty} \sum_{-m}^{l} a_{l,m}^{T} Y_{l,m}\left(\theta, \phi\right) \tag{1.19}$$

which we can compressed into an angular power spectrum for a random Gaussian field:

$$C_{l}^{TT} = \frac{1}{2l+1} \sum_{m=-l}^{l} \left(a_{l,m}^{T*} a_{l,m}^{T}\right) \tag{1.20}$$

The anisotropy of the CMB is a result of the acoustic oscillation of the baryon-photon fluid in the dark matter density background set in motion by the initial

conditions set by the scalar perturbations during inflation. Figure 1.3 shows the temperature power spectrum of the CMB. The peaks in correspond to the modes that are caught at maximum compression or rarefaction at recombination. For example, the first peak is the mode that just completed its first compression after entering the horizon, creating a high density of photons in the gravitational potential well. The second peak corresponds to modes that have gone through one compression and is maximally rarefied at recombination.
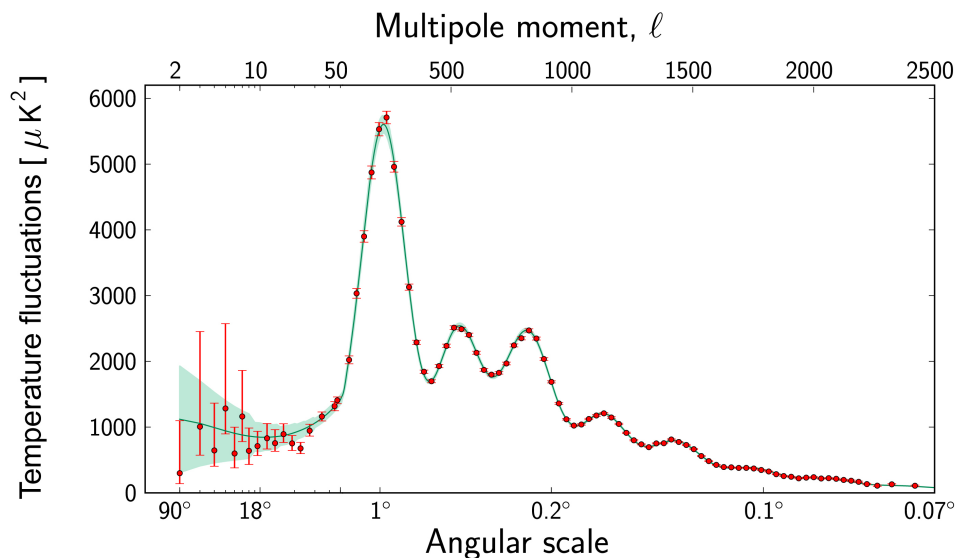
Figure 1.3: Power spectrum of temperature fluctuations in the Cosmic Microwave Background measured by *Planck*, low *l* data are limited by cosmic variance [3].

The power spectrum of the CMB temperature anisotropies can be fitted with the 6-parameters ΛCDM model. The location of the first peak serves at a standard ruler to constrain the mean spatial curvature Ω_K of the Universe, and deduce the value of Ω_Λ. The ratio of the second and third peaks provides constraints for dark matter and baryonic matter content in the Universe. The tilt of the temperature anisotropy spectrum relates to the tilt of the primordial spectrum n_s. A 5σ deviation from $n_s = 1$ supports the theory of inflation (Section 1.3), and the locations of the acoustic peaks supports an adiabatic perturbation as the initial condition of inflation.

1.3 Inflation

The theory of inflation was invented in 1981 by [7] to explain the Horizon problem and the Flatness problem in the standard model of cosmology.

In the Big Bang model, the horizon always increases in size in co-moving coordinates during matter and radiation domination, which means that the modes that entered the horizon in the beginning of the Universe should never in causal contact. But observations of the CMB have found its temperature is uniform to 1 part in 10,000 in all directions on the sky, supporting that there must be a period of time that they were in thermal equilibrium between the entire system. This is known as the *Horizon problem*.

In the standard Big Bang model, the expansion of the Universe causes the volume in casual contact in the observable Universe to increase in size and drives the total energy density Ω_{total} away from 1. Any deviation from a total flat geometry in the early Universe should have made it more curved today. However, current measurements of the curvature density Ω_K has shown that the Universe is close to spatially flat ($|\Omega_K| < 0.01$), which is known as the *Flatness problem*.

Inflation postulates a period of exponential expansion of ~ 60 *e*-folds before the standard Big Bang. This accelerated expansion resulted the horizon grows more slowly than the Universe's expansion, that the horizon shrinks in co-moving coordinates. The modes re-entering the horizon during recombination was inside the horizon during inflation, solving the Horizon problem. Inflation also solves the Flatness problem by stretching space out until the flatness in the early Universe meets the observation we see today.

Single field slow-roll inflation

The most generic model for inflation is the single field inflation [8]. It exists a scaler field ϕ, with potential $V(\phi)$. This field should have a cosmological constant like equation of state in order to drive inflation. We can write the density ρ and pressure p components from its energy-momentum tensor $T_{\mu\nu}$:

$$\rho = \frac{1}{2}\dot{\phi}^2 + V(\phi) \tag{1.21}$$

$$p = \frac{1}{2}\dot{\phi}^2 - V(\phi) \tag{1.22}$$

From energy conservation in Equation 1.6, we can derive the equation of motion of the field:

$$\ddot{\phi} + 3H\dot{\phi} = \frac{dV}{d\phi} \tag{1.23}$$

which is the equation of a simple damped harmonic oscillator, and H is the Hubble friction. From Friedmann equation, we obtain:

$$H^2 = \frac{1}{3M_{pl}} \left[\frac{1}{2}\dot{\phi}^2 + V \right] \tag{1.24}$$

For an accelerated expansion, inflation requires $\ddot{a} > 0$, which implies $\rho + 3p < 0$. Equation 1.23 shows this can be achieve by having $\dot{\phi} \ll V(\phi)$. It means the potential energy of the field drives inflation and need to be much bigger than the kinetic energy of the field. This is the first slow-roll condition:

$$\epsilon \equiv \frac{\dot{H}}{H^2} \ll 1 \tag{1.25}$$

shows the the potential of the field is close to flat.

From the equation of motion, it shows the first slow roll condition must be satisfied for a sufficiently long time, so the kinetic term does not grow too fast and overwhelms the potential term. So we have the second slow-roll condition:

$$\ddot{\phi} \ll \dot{\phi}H \tag{1.26}$$

and we can rewrite it as the second slow roll parameter:

$$\eta \equiv -\frac{\dot{\epsilon}}{H\epsilon} \ll 1 \tag{1.27}$$

The requirement for an inflation model is fairly weak, we only need the potentials in the models satisfy the slow roll condition in Equation 1.25 and Equation 1.27 with a minimum number of e-folding, N_e during inflation needed to solve the Horizon problem. Figure 1.4 shows a simple small field slow-roll inflation model.

For an exponential inflation, the e-folding N can be written as:

$$N \equiv \int_{a_i}^{a_f} d\ln a = \int_{t_i}^{t_f} H(t)\, dt \simeq \int_{\phi_{end}}^{\phi} \frac{V}{V'} d\phi \tag{1.28}$$

In order to solve the Horizon problem, the e-folding is estimate to be $50 - 60$. The exact number of e-foldings depends on the energy density at the reheating, that the inflation field is converted into kinetic energy and breaks the slow roll conditions near the end of inflation.
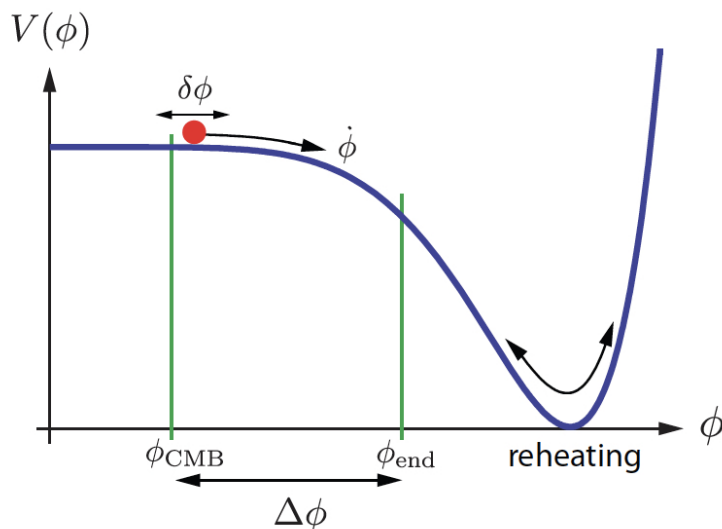
Figure 1.4: Example of an inflation potential, acceleration occurs when the potential energy of the field V dominates over its kinetic energy $\frac{1}{2}\dot{\phi}^2$. Inflation ends at ϕ_{end} when the slow-roll conditions are violated, and the energy density of the inflation is converted into radiation [9].

Perturbation in inflation

The homogeneous part of the inflation field tells us the conditions for the exponential expansion and end of inflation. But the perturbations during inflation provide the initial conditions for structure formation. These quantum fluctuations during inflation are zero-point vacuum fluctuations of the inflation field, which create a scale invariant spectrum of perturbations.

The inflation scalar field with a first order perturbation can be shown as:

$$\phi(\vec{x}, t) = \bar{\phi}(t) + \delta\phi(\vec{x}, t) \tag{1.29}$$

where $\bar{\phi}$ is the mean field and $\delta\phi$ is the perturbation.

The metric perturbation then can be written as:

$$g_{\mu\nu}(\vec{x}, t) = \bar{g}_{\mu\nu}(t) + h_{\mu\nu}(\vec{x}, t) \tag{1.30}$$

that $\bar{g}_{\mu\nu}$ is the mean and $h_{\mu\nu}$ is the perturbation of the metric.

The perturbation of the metric could be decomposed into scalar, vector, and tensor components. Scalar perturbations lead to non-uniformity in the plasma density at the surface of last scattering, and are observed as the temperature anisotropies in the CMB. Vector perturbations decay away with expansion as $1/a^2$. Tensor

perturbation create gravitational waves, so the quantum fluctuations in the transverse and traceless part of the metric, and expect to leave an imprint in the *B*-mode polarization (Section 1.4) of the CMB.

Scalar Perturbations

Scalar perturbations create the initial conditions for the temperature anisotropies in the CMB, and the fluctuations in the matter distribution seeds the structure formation of the Universe.

From the perturbation of the inflation field, the Mukhanov-Sasaki equation for scalar perturbations is:

$$\frac{d^2 R_k}{d\tau^2} + \frac{2}{z}\frac{dz}{d\tau}\frac{dR_k}{d\tau} + k^2 R_k = 0 \tag{1.31}$$

where k is the wave number, τ is the conformal time and $z \equiv a\dot{\phi}/H$.

In the slow-roll condition, $q/aH \ll 1$, the solution is:

$$R_k(\tau) = \frac{\sqrt{-\pi\tau}}{2(2\pi)^{3/2} z(\tau)} e^{i\pi\nu/2 + i\pi/4} H^{(1)}(-k\tau) \tag{1.32}$$

where $\nu = 3/2 + 2\epsilon + \eta$, and ϵ, η are the slow-roll parameters in Equation 1.25 and 1.27.

Late in the inflation, the k dependence of R_k is

$$R_k^0 \propto k^{-\nu} = k^{-3/2 - 2\epsilon - \eta} \tag{1.33}$$

We can parametrize the scalar power spectrum with number k to

$$P_s(k) \equiv \left|R_k^0\right|^2 = A_s k^{n_s - 4} \tag{1.34}$$

Together with Equation 1.33 and 1.34, we have the relation between the scalar spectral index n_s and the slow-roll parameters:

$$n_s = 1 - 4\epsilon - 2\eta \tag{1.35}$$

A perfect scale invariant spectrum has $n_s = 1$, but most models of inflation predict n_s to be close but not exactly one.

Tensor Perturbations

Similar to the scalar perturbations in Equation 1.31, tensor perturbations D_k satisfies [10]:

$$\frac{d^2 D_k}{d\tau^2} + 2Ha\frac{dD_k}{d\tau} + k^2 D_k = 0 \tag{1.36}$$

In the limit of $q/aH \ll 1$ during for a slow-roll inflation, the solution D_k^0 is:

$$D_k = \frac{\sqrt{-\pi\tau}}{2(2\pi)^{3/2} z(\tau)} e^{i\pi\nu/2 + i\pi/4} H^{(1)}(-k\tau) \tag{1.37}$$

The spectral dependence of D_k is:

$$D_k^0 \propto k^{-\mu} = k^{-3/2-\epsilon} \tag{1.38}$$

We can parametrized the tensor spectrum $P_t(k)$ to:

$$P_t(k) = A_t k^{n_t - 3} \tag{1.39}$$

A invariant spectrum would give the tensor spectral index $n_t = 0$. We can also relate the slow-roll parameter and the tensor spectral index:

$$n_t = -2\epsilon \tag{1.40}$$

We define the tensor-to-scalar ratio r to be the ratio of the tensor to the scalar spectrum:

$$r \equiv \frac{4\left|D_k^0\right|^2}{\left|R_k^0\right|^2} \sim 16\left(\frac{\dot{H}}{H^2}\right) = 16\epsilon \tag{1.41}$$

The tensor-to-scalar ratio r provides a measurement of energy scale of inflation:

$$V^{1/4} \sim \left(\frac{r}{0.01}\right) 10^{16}\text{GeV} \tag{1.42}$$

A detection of the tensor-to-scalar ratio r would provide a measurement of gravitation waves from the early Universe. The energy scale shows that it is probing physics at the GUT scale.

Cosmic variance

Scalar perturbations generated during inflation create regions of over and under density in the plasma as they re-enter the horizon. During recombination, these non-uniformity of the plasma created the temperature anisotropy of the CMB shown in Section 1.2. The spectral tilt $n_s < 1$ was also measured at 5σ from the CMB

temperature. The measurement from CMB temperature alone is ultimately limit by cosmic variance at low l as there is only one Universe to observe from. The limit set be cosmic variance is:

$$\Delta C_l = \frac{2}{2l + 1} C_l^2 \tag{1.43}$$

as we can see at the low l region in figure 1.3.

1.4 Polarization of the Cosmic Microwave Background

Stokes Parameters

A polarized photon traveling in the $\hat{z}$ direction can be described by two transverse electromagnetic plane waves E [11]:

$$E(x, t) = E_x \cos(\omega t - \theta_x) \tag{1.44}$$

$$E(y, t) = E_y \cos(\omega t - \theta_y) \tag{1.45}$$

where ω is the frequency and θ is the phase of the wave. The electric field then can be decomposed into four Stokes parameters:

$$I = \left\langle E_x^2 \right\rangle + \left\langle E_y^2 \right\rangle \tag{1.46}$$

$$Q = \left\langle E_x^2 \right\rangle - \left\langle E_y^2 \right\rangle \tag{1.47}$$

$$U = 2\left\langle E_x E_y \right\rangle \cos(\theta_x - \theta_y) \tag{1.48}$$

$$V = 2\left\langle E_x E_y \right\rangle \sin(\theta_x - \theta_y) \tag{1.49}$$

Stokes parameter I is the intensity, Q and U are the plus $+$ and cross $\times$ polarization respectively, and V is the circular polarization. CMB Polarization is not expected to generated circular polarization through Thomson scattering. The rest of the chapter will focus on the Q and U polarization.

The Stokes parameters $[Q, U]$ are coordinate dependent. A rotation of the x and y axes by angle ϕ as:

$$(Q \pm iU)'(\hat{n})(\hat{n}) = e^{\mp 2i\phi}(Q \pm iU)(\hat{n}) \tag{1.50}$$

It is more useful to parametrize in terms of two coordinate invariant quantities E and B-modes. The polarization field can be decomposed into spin-2 spherical harmonics:

$$(Q \pm iU)(\hat{n}) = \sum_{l=1}^{\infty} \sum_{m=-l}^{l} a_{\pm 2, lm \pm 2} Y_{lm}(\hat{n}) \tag{1.51}$$

The E and B-modes coefficients are:

$$a_{lm}^{E} = -\frac{1}{2} \left(a_{2, lm} + a_{-2, lm} \right) \tag{1.52}$$

$$a_{lm}^{B} = \frac{i}{2} \left(a_{2, lm} - a_{-2, lm} \right) \tag{1.53}$$

The angular power spectrum of the E and B-modes are:

$$C_{l}^{EE} = \frac{1}{2l + 1} \sum_{m=-l}^{l} \left(a_{lm}^{E*} a_{lm}^{E} \right) \tag{1.54}$$

$$C_{l}^{BB} = \frac{1}{2l + 1} \sum_{m=-l}^{l} \left(a_{lm}^{B*} a_{lm}^{B} \right) \tag{1.55}$$

In here, E-modes are even (curl-free) and B-modes are odd (curl) under parity inversion, an analogy to a magnetic field.

Generation of CMB polarization

Polarization of the CMB is generated by Thomson scattering off free electrons by photons during the period of recombination. Thomson scattering can be shown as:

$$\frac{d\sigma}{d\Omega} \propto |\hat{\epsilon} \cdot \hat{\epsilon}'|^2 \tag{1.56}$$

where $\hat{\epsilon}$ is the incident polarization direction and $\hat{\epsilon}$ is the scattering polarization direction. As the incident photon hits an electron, it sets in motion the electron parallel to the direction of the incident electric field (Figure 1.5). An oscillating electron emits radiation normal to the direction of motion, therefore the scattered radiation peaks in the direction normal to the incident polarization. Polarization amplitude depends on the electron's local quadrupole anisotropy.
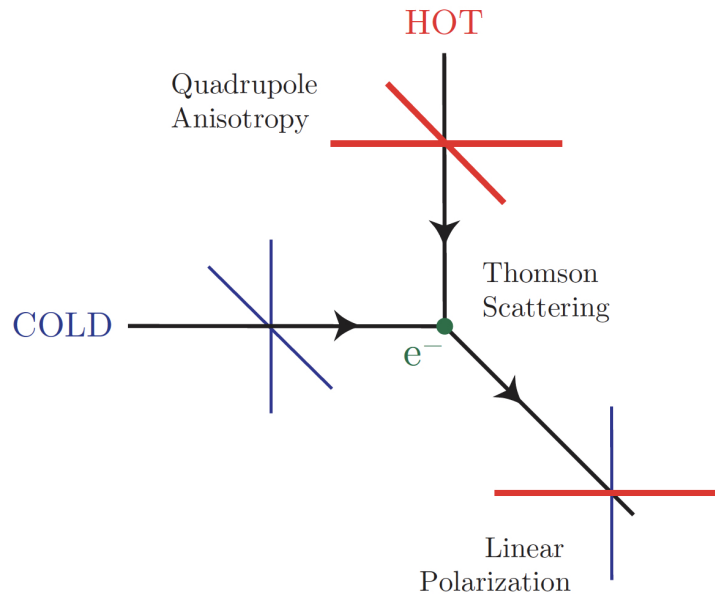
Figure 1.5: Thomson scattering of radiation with a quadrupole anisotropy generates linear polarization.

Quadrupole temperature anisotropy at recombination can be generated by higher and lower density region through the acoustic oscillation of the baryon-photon fluid (Density wave). In this case, the polarization created is perpendicular to the gradient of the polarization amplitude, scalar perturbation can only form a curl-free, E-mode pattern. Furthermore, because the scattering takes place during the transition from an opaque plasma to a transparent neutral hydrogen gas, the correlation length of the polarization should be of order the mean free path. The E-mode polarization is also correlated with the temperature anisotropy since the latter created the former.

The tensor perturbations described in Section 1.3 also enter the Horizon during recombination. The propagating form of the tensor perturbations are gravitational waves. The gravitational waves stretch and distort space-time as they travel, resulting non-rotational invariant quadrupole anisotropies around the direction of travel. Polarization generated by tensor perturbations would have a handedness to them. If the gravitational waves have a + polarization, then it generates E-modes, but if the gravitational waves have a $\times$ polarization, the polarization would be a curl, B-mode pattern (Figure 1.6). Because B-mode polarization cannot created by scalar modes, it does not suffer from the sample variance in E-mode polarization.

Since gravitational waves travel at the speed of light, about $\sqrt{3}$ faster than the speed
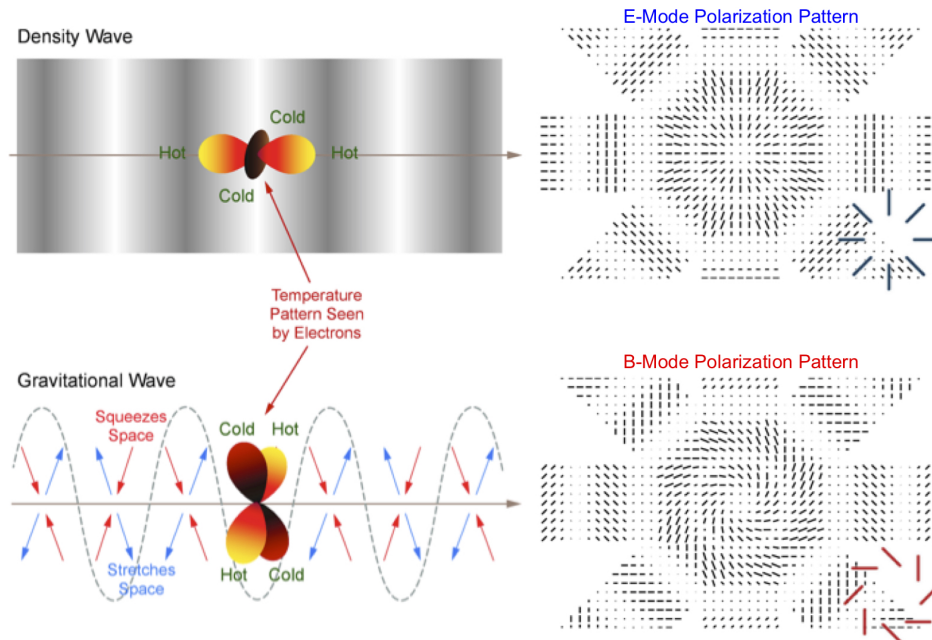
Figure 1.6: Example of a E and B mode polarization created by density and gravitational waves. Scalar perturbations can only create polarization that is even under parity inversion (E-mode). Tensor perturbation produced from gravitational wave stretch and distort space time as they travel, which is not rotational invariant around the direction of travel, and can reate polarization that has a handiness, or odd under parity inversion (B-mode).

of sound of the baryon-photon fluid created the temperature and E-mode anisotropy, the first peak of the B-mode power spectrum is expected to locate at a larger angular scale of $l \sim 100$.

1.5 Probing B-mode polarization

A detection of B-mode polarization generated by primordial gravitational waves would be a direct evidence of the theory of inflation. Figure 1.7 shows the published constraints and measurements of B-mode polarization.

At small angular scale, lensing B modes are first detected by the South Pole Telescope in cross-correlation with cosmic infrared background [12][13], and the lensing BB spectrum measured by the POLARBEAR collaboration [14]. For degree-scale measurement, the most sensitive constrain on B-mode comes from BICEP experiment. The three year BICEP1 result showed an upper limit of $r < 0.7$ [15]. In 2014, BICEP2 published a 5σ detection of degree-scale B-mode polarization at 150 GHz [16]. BICEP2 is a single frequency telescope which relied on other experiments for
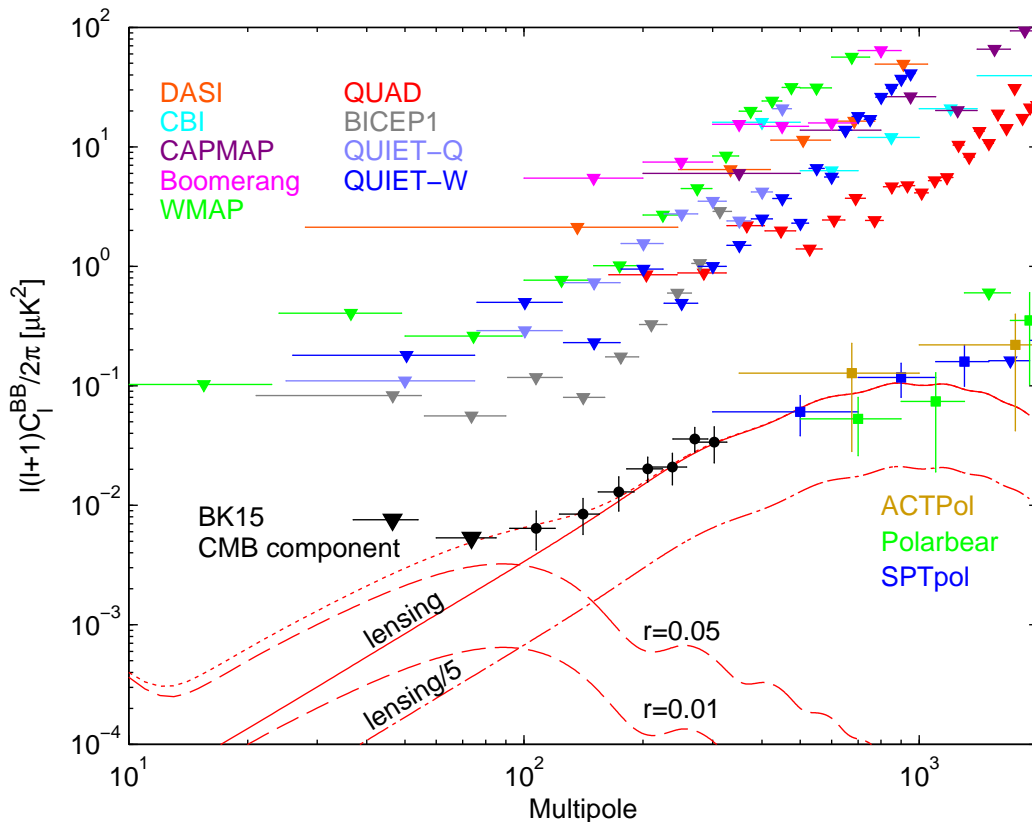
Figure 1.7: Published *B*-mode polarization measurement by different experiments. Lensing *B*-mode has been detected by Bicep, SPT, Polarbear, and ACT collaboration.

foreground subtraction. Subsequent cross-correlation with *Planck* high-frequency data showed the polarized Galactic dust emission could account for the excess signal at 150 GHz measured by Bicep2. A joint analysis between Bicep2 and *Planck* later improved the upper limit of $r < 0.12$ at 95% confidence with a multifrequency, multicomponent analysis [17].

Since then, combination with Bicep2 and the *Keck Array*, we improved the upper limits on $r < 0.07$ at 95% confidence ($r < 0.06$ in conjunction with *Planck* temperature measurements and other data) through multifrequency, foreground-cleaned data. Currently, the *Keck Array* is deployed with multiples receivers at high-frequency to measure polarized dust at high significance, while Bicep3, with 2500 detectors continues to make deep measurements at the foreground cleared 95 GHz channel. Starting from 2019, the new Bicep Array will gradually replace the *Keck Array* with Bicep3 class receivers in full range of frequency, allow us to probe the inflationary gravitational wave amplitude of $\sigma(r) < 0.004$ when finish.

1.6 Outline of the dissertation

The outline of the dissertation is structured as follow: Chapter 2 is an overview of the BICEP experiment, describing the overall design concept, observation site, location, and evolution of the program.

Chapter 3 describes the BICEP3 instrument design, including the optics, cryogenic performance, focal plane and detectors. In particular, we focus on the modular detector packaging, antenna-coupled transition edge sensor bolometers, and the time-domain multiplexing SQUIDs readout.

Chapter 4 describes the instrument characterization for BICEP3. Many of the measurements are focused on detector performances, including its spectral response, optical efficiency, and noise at observation and high frequencies. We also discussed the magnetic pick up at the readout electronic from Earth's field, and how much it affects the quality of the data.

Chapter 5 is a review of the analysis pipeline used in BICEP, and changes we made to accommodate the bigger field obverved in BICEP3 compare to previous telescopes. We show the procedure of map making from time-stream data, and matrix based techniques we use to minimize E to B leakage due to partial sky coverage and filtering of the data.

Chapter 6 is a summary of the current cosmological constraint from the latest result in BICEP, and forecast improvement after adding the current two years observation data from BICEP3. Finally, we give a brief introduction of the next generation BICEP ARRAY which largely based on the design of BICEP3.

Chapter 2

THE BICEP/*KECK ARRAY* EXPERIMENT

The Cosmic Microwave Background is first discovered in 1965. Since then many more features in the CMB are detected. For example, the temperature anisotropy and perfect blackbody signature; the amplitude and location of the acoustic peaks of the power spectrum; and the faint polarization signature in the CMB. Through these discoveries, we have learned the age, content, and geometry of the Universe; which allows us to explain the evolution of the Universe through a 6-parameters ΛCDM standard model.

A forthcoming and ambitious science goal in the CMB is to detect the degree scale B-mode polarization from the inflationary gravitational waves. The Bicep/*Keck Array* experiment is a series of telescopes located at the South Pole, Antarctica, in attempt to measure this signal. This chapter gives an overview of the fundamental design aspects of the experiment, from general telescope design (Section 2.1), site selection (Section 2.2), to scan strategy (Section 2.4).

2.1   Overview of the Bicep/*Keck Array* Experiment

Starting with Bicep1 in 2006, through Bicep3 which deployed in 2015, to the future Bicep Array, the Bicep/*Keck Array* experiment is designed to have a single science goal: to detect the degree scale B-mode polarization of the Cosmic Microwave Background arised from the primordial gravitation waves. If detected, this allow us to probe the very early universe, and learn about high energy physics beyond any man-make accelerators. The signal can be quantify by the tensor-to-scalar ratio r (Section 1.5).

The *B*-mode signature is expected to peak at degree scale ($l \sim 80$), but the strength of the signal is much smaller than the measured *E*-mode polarization. Since resolution is less important than sensitivity, the Bicep/*Keck Array* experiment is a series of cold, compact on-axis refracting telescope, with beam size of about 0.5 degrees. This low photon loading design, plus the small patch sky observation (Section 2.4), allows for high sensitivity measurement.

We use dual polarization sensitive antenna-couple transition edge sensor (TES) bolometers (Starting from Bicep2 in 2009) for these telescopes. Each individual
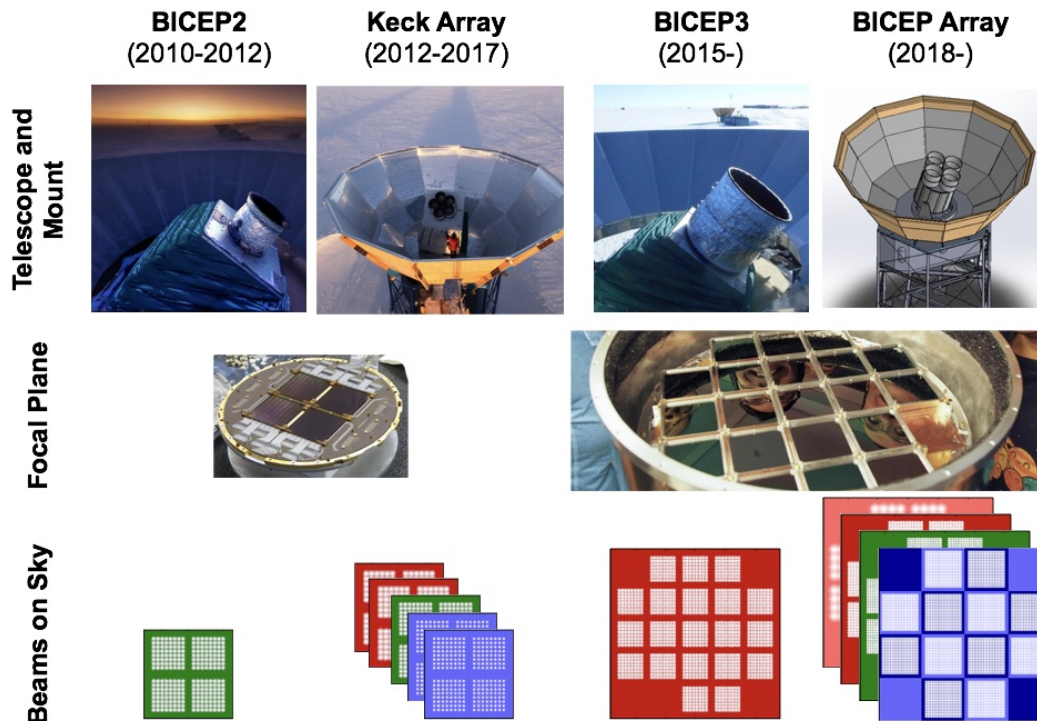
Figure 2.1: The BICEP/*Keck Array* development history. All of these utilized antenna couple TES bolometers. BICEP2 has 500 detectors at 150 GHz, BICEP3has 2400 detectors at 95 GHz, and the future BICEP ARRAY will have 10,000+ detectors from 30 to 270 GHz.

receiver observes at a single frequency. BICEP2 has a single receiver with 500 detectors at 150 GHz, while *Keck Array* has five BICEP2 like receivers installed in a single mount, observing from 90 to 270 GHz throughout multiple seasons. BICEP3 replaced BICEP2 in 2015, with ~2500 detectors at 95 GHz in a single receiver. BICEP ARRAY composed of four BICEP3 like receivers, will replace the *Keck Array*in 2018, and will house more than 10,000 detectors from 30 to 270 GHz. Figure 2.1 and Table 2.1 show the deployment history of the experiment.

The compact, modular receiver design, enables us to simplify the anti-reflection design in the optics, yet allows us to observe in multiple frequencies. For example, the experiment is focused on 150 GHz in the first several years of the observation, but gradually switches to other frequencies to further understand the foreground in the sky. The optically symmetric design also maximizes throughput and minimizes polarization systematics. The small telescope size simplified assembly procedure and allows full boresight rotation to reduce telescope systematics. Each telescope is installed with a co-moving baffle and ground shield to reduce sidelobes and ground

Year	Receiver	Frequency (GHz)	# of detector
2010	Bicep2	150	500
2011	Bicep2	150	500
2012	Bicep2	150	500
	Keck Array Rx0	150	500
	Keck Array Rx1	150	500
	Keck Array Rx2	150	500
	Keck Array Rx3	150	500
	Keck Array Rx4	150	500
2013	*Keck Array* Rx0	150	500
	Keck Array Rx1	150	500
	Keck Array Rx2	150	500
	Keck Array Rx3	150	500
	Keck Array Rx4	150	500
2014	*Keck Array* Rx0	95	272
	Keck Array Rx1	150	500
	Keck Array Rx2	95	272
	Keck Array Rx3	150	500
	Keck Array Rx4	150	500
2015	*Keck Array* Rx0	95	272
	Keck Array Rx1	220	500
	Keck Array Rx2	95	272
	Keck Array Rx3	220	500
	Keck Array Rx4	150	500
2016	Bicep3	95	2400
	Keck Array Rx0	210	500
	Keck Array Rx1	220	500
	Keck Array Rx2	210	500
	Keck Array Rx3	220	500
	Keck Array Rx4	150	500
2017	Bicep3	95	2400
	Keck Array Rx0	210	500
	Keck Array Rx1	220	500
	Keck Array Rx2	210	500
	Keck Array Rx3	220	500
	Keck Array Rx4	270	500

Table 2.1: Bicep/*Keck Array* deployment history, receiver names, nominal number of optically-coupled detectors, and frequencies. *Keck Array* and Bicep3 were first deployed in 2011 and 2015, respectively, but their first year's engineering run data were not used in the science data analysis. The 95 GHz detector number in *Keck Array* is limited by increase of pixel size, while the high frequency focal planes are limited by existing readout electronic.

28.7" diameter

96" top to bottom

10x Reflective IR Filters
50K Alumina IR Filter

HDPE Window

Pulsetube Cryocooler

4K Alumina Objective Lens
4K Nylon IR filter

Pulsetube
Heatstraps

Vacuum Jacket (300K)
50K stage
4K stage

4K Alumina Field Lens
4K Nylon IR filter
250mK Detectors / Focal Plane

Diameter expansion area and
structural G10 truss

Sub-Kelvin Fridge

Pentagon Basering (electrical feedthrough interface)

Figure 2.2:   Cutaway view of the Bicep3 cryostat receiver. The entire receiver is cryogenic, with the optics tube cooled to 4 K with a pulse tube cooler, and the focal plane structure cooled to 250 mK with a 3-stages, helium sorption fridge.

pickup. Figure 2.2 shows the Bicep3 receiver design, and Figure 2.3 shows the relative size for the different receivers.

Detail of the instrument design of Bicep2 can be found in [18], with the science result in [16][17][19]. *Keck Array* is described in multiple conference proceedings [20][21][22].

2.2   Telescopes site

The Bicep/*Keck Array* experiment is located at the Amundsen-Scott South Pole Station in Antarctica. It is the location for many millimeter-wave experiments because of its stability and low precipitable water vapor. The ~10,000 ft altitude with cold weather make the Antarctic plateau one of the driest places on earth (Figure 2.4). During the winter season, the 6-months of continuous darkness also provides extremely stable atmosphere.
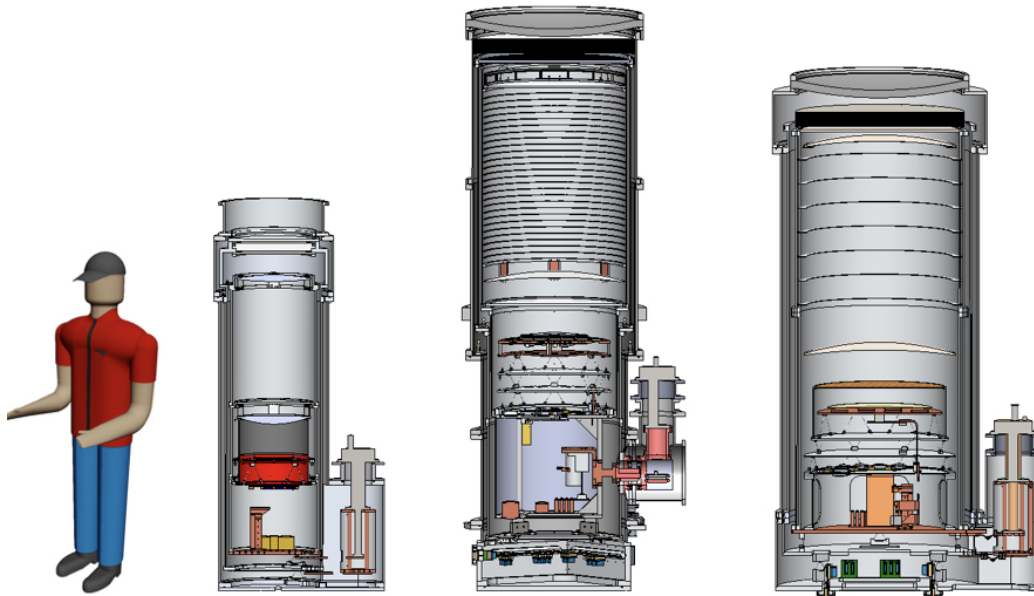
Figure 2.3: Receivers in Bicep/*Keck Array*. The left most is a model of the *Keck Array* receiver (Bicep2 is almost identical, but without the pulse tube cooler). The middle is Bicep3, and the right is the design for Bicep Array.
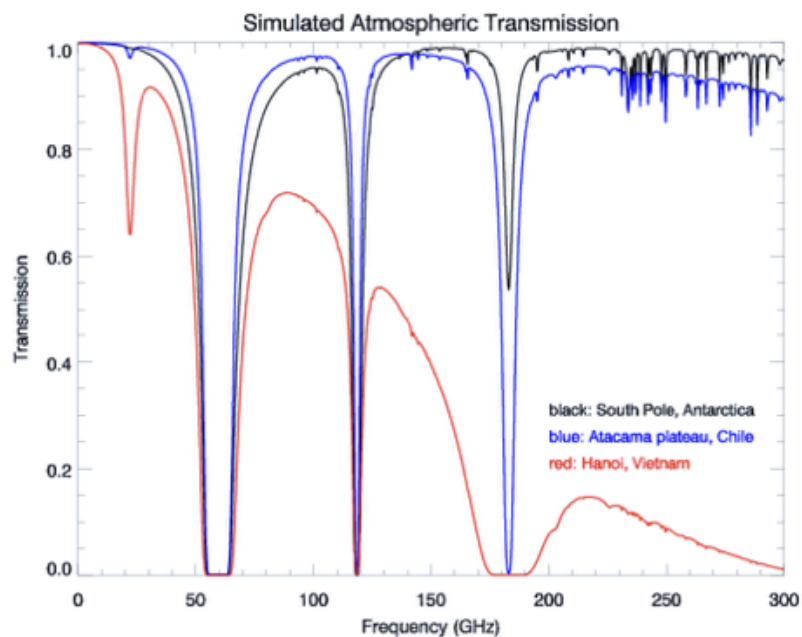
Figure 2.4: Simulated atmospheric transmission in the South Pole, Atacama, and Vietnam. Most CMB experiments observe at 90, 150 and 220/270 GHz bands, which the South Pole has one of the best atmospheric transmission in the world.
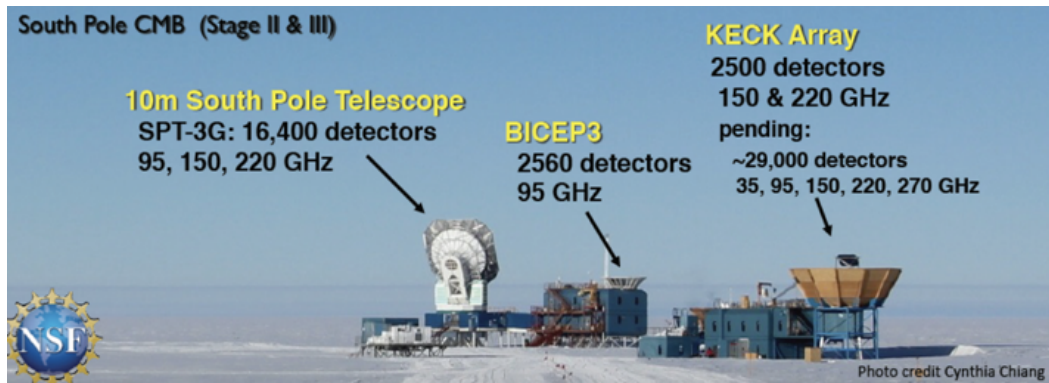
Figure 2.5: MAPO and DSL at the South Pole, these buildings housed the BI-cEP/*Keck Array* and the South Pole telescope (Credit: C. Cheng).

BICEP/*Keck Array* observed about 1 % of the sky with small elevation changes (Section 2.4). Since the sky at the South Pole simply rotates about zenith, we observed our patch of the sky at all times and scanned at a constant elevation with a simple ground template subtraction.

Keck Array is located in the Martin A. Pomerantz Observatory, BICEP3, alone with the South Pole Telescope are installed in the Dark Sector Lab (Figure 2.5). Both buildings are about one kilometer away from the NSF South Pole Station (Figure 2.6). We deploy to the station during the austral summer, between November and February, to install, upgrade, and calibrate the instruments; while the rest of the winter brings many month of excellence observing conduction with stable weather and low $1/f$ noise.

2.3   Frequency coverage

The joint analysis between the BICEP and *Planck* collaboration on B-mode shows that the first detection of degree scale B-mode measured by BICEP2 is contaminated by polarized galactic dust. We are now limited by uncertainty in foreground separation, which will require sensitive polarization maps in a broad range of frequencies to differentiate them from the CMB signal. Figure 2.7 shows the spectral dependence of polarized dust and synchrotron, multifrequency polarization observations will be needed to separate the foreground components from the CMB.

While *Planck* has multifrequency, polarization data of the sky. The noise in the high frequency maps from *Planck* are above the current limit on r to successfully separating the polarized dust from the CMB. In order to cleanly extract the CMB B-mode signal, it is necessary to observe the sky at high frequency with comparable

Figure 2.6: The Amundsen-Scott South Pole Station, the Dark Sector where all the telescopes housed are located on the right. The *Keck Array* and the future BICEP ARRAY are installed in the Martin A. Pomerantz Observatory, the BICEP3 telescope and the South Pole Telescope are installed in the Dark Sector Lab. Left side of the picture is the station, separated by the airplane runway.
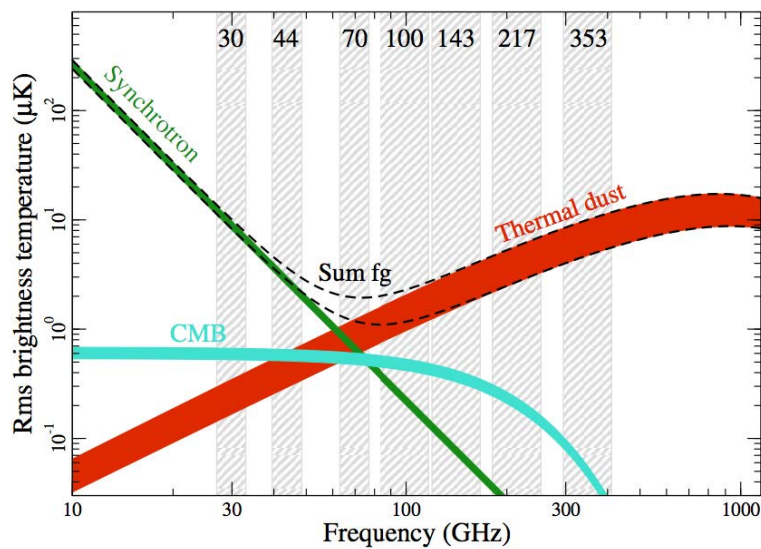
Figure 2.7: Foreground contributions as a function of frequency. The dash lines indicate foreground levels with $f_{sky} = 73\%$. Credit: *Planck* Collaboration

sensitivities to Bicep2.

In the last few years, benefiting from the modular design, *Keck Array* has been gradually switching from all 150 GHz receivers configuration into high frequencies 'dust telescope', observing at 210, 220, and 270 GHz, while the newly additional of Bicep3 continues to probe the low foreground, 95 GHz channel. The future Bicep Array will follow the same strategy, with additional channel at 30/40 GHz, allowing us to separate the synchrotron signal from CMB.

2.4 Observation strategy

The inflationary *B*-mode signature is expected to peak at $l \sim 100$ in the power spectrum, which in turn set our science band at $20 < l < 200$. The minimum sky coverage is limited by the largest mode in the science band [23]:

$$\Delta C_l = \sqrt{\frac{2}{(2l + 1) f_{\text{sky}}}} [C_l + N_l] \tag{2.1}$$

where f_{sky} is the sky fraction, with noise N_l.

We choose to scan on a small ($\sim 1\%$) patch of sky that is exceptionally free of dust and synchrotron foregrounds in total intensity (Figure 2.8), so that we can create a deep polarization maps in that region. Bicep/*Keck Array* scans right ascension $-60° < \text{RA} < 60°$ and declination $-70° < \delta < -40°$.

Bicep3's larger optical FOV results in an effective sky area of $\sim 600\text{deg}^2$, compare to the $\sim 400\text{deg}^2$ in previous experiments in the program. The fundamental observing block is a constant-elevation scanset of 50 back-and-forth, 2.8 deg/s fixed-center azimuth scans spanning 64.4°. Each scanset is bookended by a elevation nod of 1.3° peak to peak for airmass-based detector gain calibration and a partial detector loadcurves to monitor detector performance, for a total of ~ 50 minutes. The azimuth center is adjusted every other scanset to track the changing RA of the sky patch, and the elevation is staggered by 0.25° steps offset.

For Bicep3, the observation schedules are repeated on a two and three sidereal day cadence in 2016 and 2017 onward, respectively. Each schedule containing CMB-targeted and Galactic plane scansets, and cryogenic service. Table 2.2 lists the phases included in each schedule, and Figure 2.9 shows the mount motion during that time.
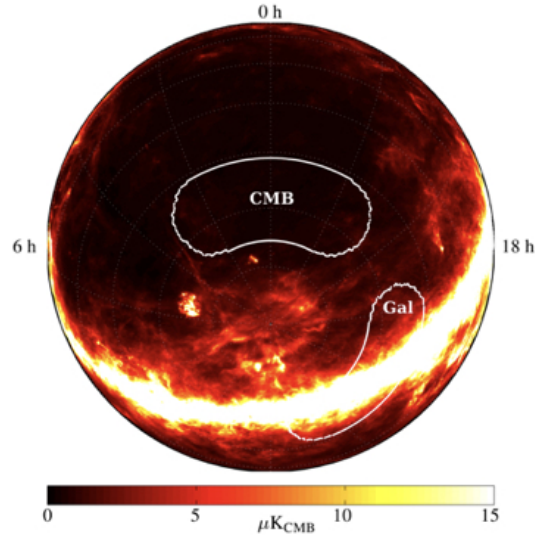
Figure 2.8: The sky patch measured by the BICEP experiment. This 400 deg^2 and 600 deg^2 for *Keck Array* and BICEP3 respectively. It is chosen to be one of the cleanest foreground patch of the sky.
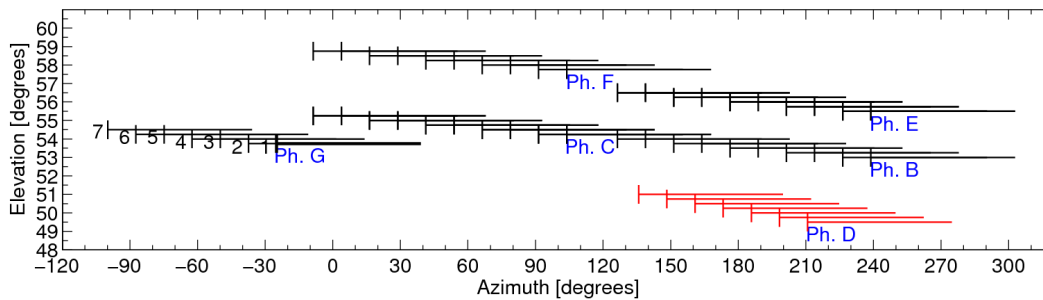
Figure 2.9: Observation pattern of a typical three-day schedule.

Each full observation cycle uses one of four (8 for *Keck Array*) boresight angles to constrain polarization systematics: two sets of 180° opposing orientation, offset from each other by 45°, and clocked to optimize coverage symmetry of both the Stoke Q and U polarizations on the sky.

A signal with frequency f corresponds to multipole $l = 240f$, which results 0.05 - 1 Hz corresponds to the science band of $20 < l < 200$.

The list below shows the terminology used in this dissertation, as described in [24]:

- **Halfscans:** During normal observations, the telescope scans in azimuth at a constant elevation. The scan speed of 2.8 deg s^{-1} in azimuth places the

Table 2.2: BICEP3's observation schedule. Start times are listed by Local Sidereal Time (LST). Phase G, H and I are not used in 2016 season due to a two days cryogenic cycle.

Phase	LST	Field	No. of Scansets
A	Day 0 23:00	Fridge re-cycling	
B	Day 1 05:00	CMB	10
C	Day 1 14:00	CMB	10
D	Day 1 23:00	Galactic	7
E	Day 2 05:00	CMB	10
F	Day 2 14:00	CMB	10
G	**Day 2 23:00**	**CMB**	**6**
H	**Day 3 05:00**	**CMB**	**10**
I	**Day 3 14:00**	**CMB**	**10**

targeted multipoles of $20 < l < 200$ at temporal frequencies less than 1 Hz. Each scan covers 64.4 degrees in azimuth, at the end of which the telescope stops and reverses direction in azimuth and scans back across the field center. A scan in a single direction is known as a 'halfscan'.

- **Scansets:** Halfscans are grouped into sets of 50 back-and-forth halfscans, which are known as 'scansets'. The scan pattern deliberately convers a fixed range in azimuth within each scanset, rather than a fixed range in right ascension. Over the course of the 50 minute scanset, Earth's rotation results in a relative drift of azimuthal coordinates and right ascension of about 12.5 degrees. At the end of each scanset the elevations is offset by 0.25 degrees and a new scanset commences. The telescope steps in 0.25 degree elevation increments between each scanset. All observations take place at 20 elevation steps, with a boresight pointing ranging in elevation between 55 and 59.75 degrees. The geographic location of the telescope, near the South Pole, means the elevation and declination are approximately the same.

- **Phases:** Scansets are grouped together into sets known as 'phases'. The CMB phases are grouped into seven types and each type has a unique combination of elevation offset and azimuthal position. Each phase contains between 6 to 10 scansets (Table 2.2).

- **Schedule:** All the telescopes in BICEP/*Keck Array* have a third degree of freedom in the telescope mount, which is a rotation about the boresight,

referred to as 'deck rotation'. The polarization angles relative to the cryostats are fixed, so rotating in deck angle allows detector pairs to observe at multiple polarization angles. A schedule consists of a set of phases at a particular deck angle. The deck angle is rotated between schedules. There is typically one schedule per fridge cycle, occurring every ~3 days for BICEP2 and BICEP3 and 2 days for *Keck Array*.

C h a p t e r   3

THE BICEP3 INSTRUMENT

BICEP3 is the latest telescope in the BICEP/*Keck Array* collaboration deployed to the South Pole. It is a 520 mm aperture, compact two-lens refractor designed to observe the polarization of the CMB at 95 GHz. It was first installed in 2014-15 austral summer, with science observation starting in 2016.

This chapter details the receiver design of the telescope. Section 3.1 shows the optic design, its infrared filtering and in-band optical loading. The overview of the cryostat design, with housekeeping electronic, RF and magnetic shielding architecture is described in Section 3.2.

With 2400 detectors, BICEP3 has more than a factor of eight detectors compared to a single *Keck Array* receiver of the same frequency. Section 3.3 shows the compact, modular focal plane design, and magnetic shielding to prevent sensitive readout electronic affected by external magnetic pickup. Section 3.4 gives an overview of the antenna-couple TES bolometer that used in all the instruments in BICEP, and Section 3.5 describes the new MUX11 style time domain multiplexing readout.

3.1   Optics

Optical design

BICEP3 follows the Bicep2/*Keck Array* strategy of compact, on-axis, two-refractor optical design to target the degree-scale primordial *B*-mode CMB polarization. It has an aperture of 520 mm and beam width given by the Gaussian radius $\sigma \sim 8.9'$. Both of the lenses, and most of the filters, are held at cryogenic temperatures inside of the cryostat receiver in order to minimize excess in-band photon load. Only the HDPE plastic cryostat window and the stack of IR filters directly behind it are mounted at room-temperature. Together with faster optics design, and doubling the aperture diameter, BICEP3 achieves ~10× higher optical throughput and detector count compared to a single *Keck Array* receiver at the same frequency. Table 3.1 shows the optical design parameters as compared to the previous generation BICEP2/*Keck Array* receivers.

The ray diagram and full optical chain is shown in Figure 3.1. The radially symmetric optical design allowed well-matched beams for two idealized orthogonally polarized

Table 3.1: Optical design parameters for a single Bɪᴄᴇᴘ2-class receiver and Bɪᴄᴇᴘ3.

	Bɪᴄᴇᴘ2/ Keck Array	Bɪᴄᴇᴘ3
Aperture dia.	264 mm	520 mm
Field of view	15°	27.4°
Beam width σ	12′	8.9′
Speed	$f/2.2$	$f/1.7$

detectors at the focal plane.

After the 31.75 mm thick HDPE window and the stack of IR filters (Metal-mesh filters in 2016, zotefoam filters in 2017 onward), there sits a 10 mm thick 50 K alumina IR filter and a single metal-mesh IR filter directly behind it. The photons then arrive at the 4 K stage which includes two refractive lenses and two IR-absorptive Nylon filters to further shield the sub-Kelvin focal plane: a 5 mm thick filter between the lenses and a 9.5 mm thick filter between the field lens and the focal plane. Finally, low-pass, hot-pressed metal-mesh filters designed by [25] with a 4 cm^{-1} (120 GHz) cutoff are mounted on the topmost surface of the detector modules to prevent any above-band radiation coupling to the bolometers (blue leaks). The cold aperture stop is defined just skyward of the objective lens with a microwave-absorptive annulus.

A warm, absorptive forebaffle extends skyward beyond the cryostat receiver (see Figure 3.2) to intercept stray light outside the designed field-of-view. It is mounted directly to the receiver and therefore comoving with axes of motion of the telescope. The forebaffle is constructed from a large aluminum cylinder, 141 cm in diameter and 129 cm in height, with the inner-face lined by microwave-absorptive Eccosorb HR-25/AN-75 and weatherproofed with Volara foam. It is also installed with heater tape to keep the forebaffle above ambient temperatures to avoid snow accumulation.

The telescope is surrounded by a stationary reflective ground shield which redirects off-axis rays to the cold sky. The combination of the baffle and the ground shield is designed such that off-axis rays must diffract twice before it hits the ground.

Vacuum window and membrane

The first optical element in the receiver is the vacuum window. This needs to be low-loss and mechanically strong to survive deflection under vacuum. Previously,
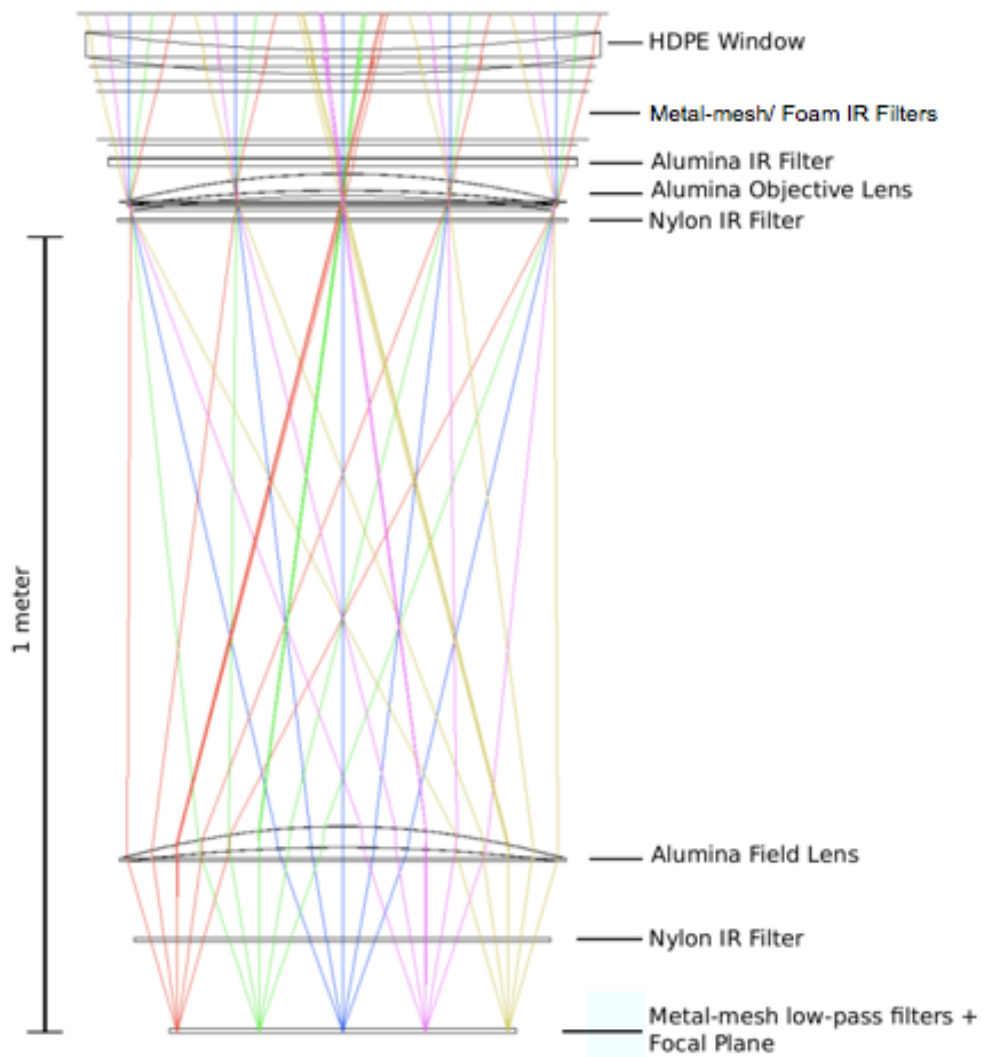
Figure 3.1: Ray diagram including the elements of the optical chain. The 300 K metal-mesh filters are replaced by HD-30 foam filters in 2017, to minimizing both the IR loading and in-band optical load.

Figure 3.2:   View of Bicep3 from the roof of DSL, showing the green insulating boot, comoving forebaffle, and reflective ground shield. The forebaffle intercepts radiation $> 14°$ from the telescope boresight. The larger *Keck Array* ground shield is visible in the background and the main Amundsen-Scott station extends along the horizon.

Keck Array used laminated HD-30 foam, but this is not strong enough for Bicep3's larger aperture. Hence, a 73 cm diameter, 31.75 mm thick HDPE window is used. The surfaces of the HDPE window are coated with a $\lambda/4$ anti-reflective (AR) layer made of Teadit 24RGD (expanded PTFE sheet). The AR coating is adhered to the window with a thin layer of low-density polyethylene (LDPE) plastic in a vacuum oven press.

In front of the window is a 22.9 μm thick biaxially oriented polypropylene (BOPP) membrane that protects the window from snow and creates an enclosed space below, which is slightly pressurized with room temperature dry nitrogen gas to prevent condensation on the window surface. The gas flow in between the membrane and window is controlled to minimize vibration.

Infrared loading

The room-temperature HDPE plastic window emits ~110 W of infrared power onto the first cryogenic stage (the absorptive 50 K alumina IR filter), but the pulsetube cryocooler is rated for less than 40 W while maintaining necessary base temperatures. This discrepancy in thermal budget necessitates that infrared power be rejected before reaching the colder cryogenic stages. Table 3.2 shows the power deposited onto each cryogenic stages.

Multiple styles of thermal filters at 300 K mounted just behind the cryostat window are experimented to reject the majority of the IR load in Bicep3:

Table 3.2: Infrared loading on each temperature stages in Bicep3

Stages	Power in 2016 [W]	Power in 2017 [W]
Window	~110	~110
50 K optics tube	19	12
4 K optics tube	0.18	0.15
350 mK stage	9×10^{-5}	8.4×10^{-5}
Focal Plane (250 mK)	3.5×10^{-6}	3.35×10^{-6}

- Stack of thin film, IR-reflective, capacitive metal-mesh filters in 2016.

- Stack of HD30 foam filters starting in 2017.

Alumina optics and filters are used in both the 50 K and 4 K stages. High emissivity in the thermal IR spectrum provides absorptive IR filtering, allow us to eliminate the thick teflon filters previously used in *Keck Array*. The higher thermal conductivity in ceramic also minimizes the temperature gradient across the lenses to less than 1 K and speeds cryostat cooldown time.

Two additional nylon filters are placed in the 4 K stage of the receiver to reduce thermal loading on the sub-Kelvin focal plane by absorbing infrared radiation.

The dominant noise source in Bicep3 is the photon noise of the in-band signal power, minimizing non-CMB photon load is therefore a major instrumentation consideration. Table 3.3 summarizes the various contributions to the total predicted per-detector photon load by considering the temperature transmission properties of each element. The compact optical design allows cryogenic operation of both refractive lenses and the absorptive infrared filters, thereby minimizing the excess photon load due to those elements' emissivity in-band. The thick plastic cryostat window must remain at room temperature and in doing so contributes a significant fraction of the non-CMB photon load from the cryostat itself. The other significant contributor from the cryostat was the scattering off each metal-mesh IR-reflective filters before replacement in 2017 with HD-30 foam filters. We see a significant in-band loading reduction from both the filters and forebaffle.

Large-diameter IR filters

The 2016 season metal-mesh filters were 3.5 μm Mylar or 6 μm polypropylene/polyethylene (PP/PE) film, pre-aluminized to ~ 40 nm deposition thickness

Table 3.3: Per-detector in-band optical load during the 2016 (2017) season, quantified as both incident power and Raleigh-Jeans temperature.

Source	Load [pW]	T_{RJ} [K]
4K lenses & elements	0.15	1.0
50K alumina filter	0.12	0.9
Metal-mesh (HD-30 foam) filters	0.63 (0.10)	5.2 (0.8)
Window	0.69	5.9
Total cryostat internal	1.6 (1.1)	13 (8.6)
Forebaffle	0.31 (0.14)	2.7 (1.14)
Atmosphere	1.1	9.9
CMB	0.12	1.1
Total	3.2 (2.5)	27 (21)

[26]. The 95 GHz, in-band transmission is around 99.5% through each filter, which resulted a total loss of 8% through the entire stack. Majority of the loss is due to scattering off the filters.

In order to avoid loading from metal-mesh filter scattering, the metal-mesh filters are replaced with a stack of 10, HD-30 foam filters (Figure 3.3) in 2017. The foam filters are made with nitrogen-expanded polyethylene foam with >99 % transmission at 95 GHz. Thermal measurement shows the temperature gradient at 50 K tube reduced from 6 K to less than 4 K after switching these filters, implies a 50 K absorbed IR power from 18 W to 12 W, or ~9× reduction of 300 K infrared loading. Through a room temperature transmission measurement, we calculated a 8 % in-band improvement comparing the foam filter stack to the metal-mesh filter.

The filter frames are stacked and mounted inside the cryostat receiver just behind the HDPE window, heatsunk to the room-temperature vacuum jacket. Table 3.4 details the individual filter used in BICEP3. One 3.5 μm metal-mesh mylar filter behind the 50K alumina filter is kept during the replacement to provide additional IR filtering.

Alumina optics and filters

BICEP3 uses alumina ceramic for several of the optical elements. Both lenses and the 50 K IR filter are made of 99.6% pure alumina sourced from CoorsTek[1]. Moving from the previous-generation HDPE plastic optical elements allow much thinner

---

[1]CoorsTek, Golden, CO 80401, USA (www.coorstek.com)
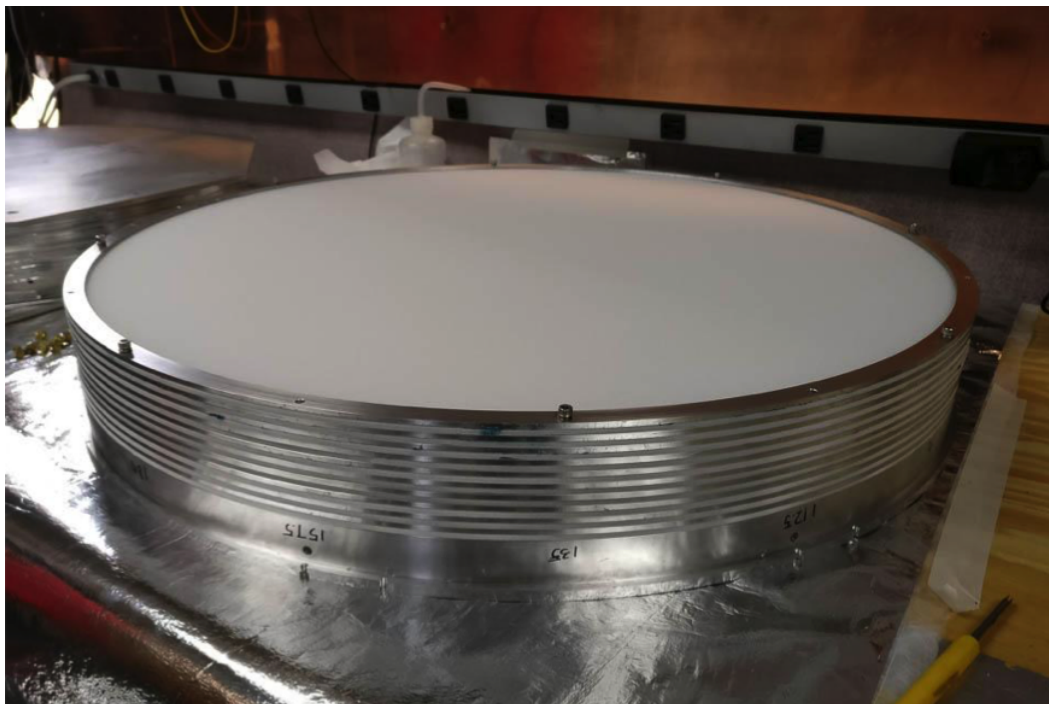
Figure 3.3: Stack of 10 layers of foam filters installed in BICEP3. Each layer is a 1/8" thick HD-30 foam, glued onto aluminum frame with 1/8" spacing. The total filter stack height is 2.5". These filters will be replace for every cryogenic run.

Table 3.4: IR filters installed for BICEP3. The main stack of 10 filters behind the window are listed in order beginning with the closest filter to the window.

Location	2016 Substrate	Square/pitch [μm]	2017 Substrate
Behind window	3.5 μm Mylar	50/80	HD-30 foam
($\sim$ 290 K)	3.5 μm Mylar	40/55	HD-30 foam
	3.5 μm Mylar	50/80	HD-30 foam
	3.5 μm Mylar	40/55	HD-30 foam
	3.5 μm Mylar	90/150	HD-30 foam
	6 μm PP/PE	40/55	HD-30 foam
	3.5 μm Mylar	50/80	HD-30 foam
	3.5 μm Mylar	40/55	HD-30 foam
	3.5 μm Mylar	50/80	HD-30 foam
	3.5 μm Mylar	90/150	HD-30 foam
Behind 50 K Alumina filter	3.5 μm Mylar	90/150	3.5 μm Mylar
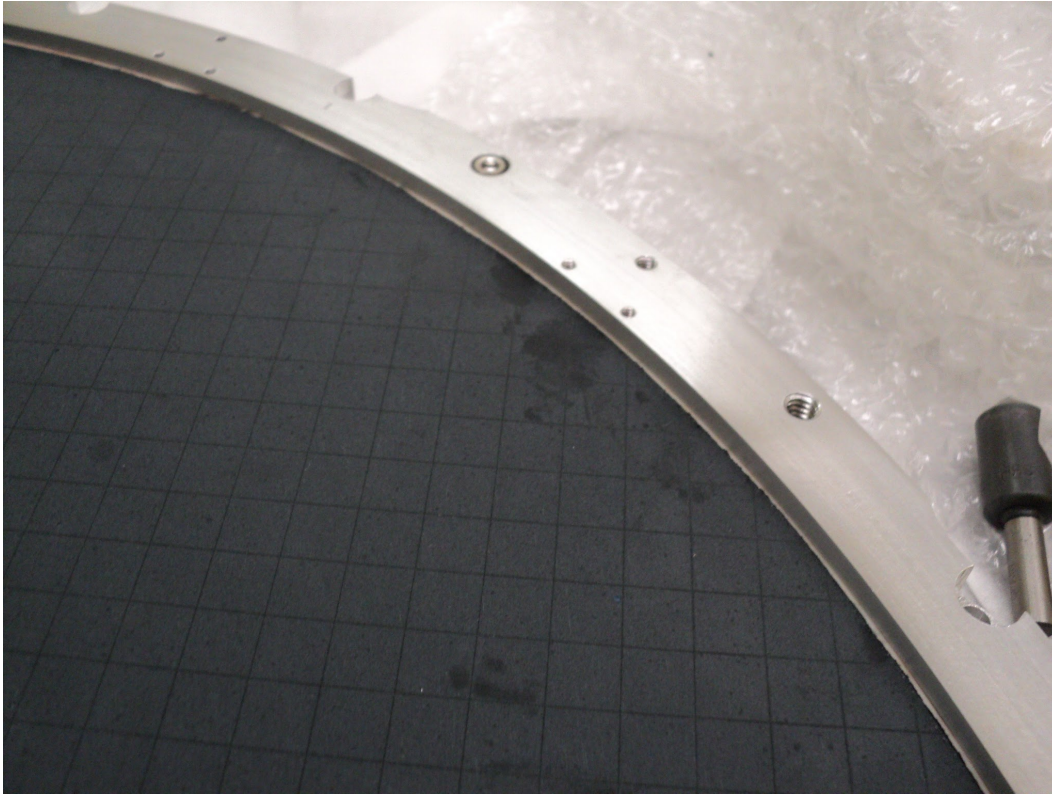
Figure 3.4: AR-coated alumina filter in BICEP3. The alumina filter is coated with a mix of Stycast 1090 and 2850FT. The epoxy is machined to the correct thickness and laser diced to 1 cm squares with avoid differential thermal contraction between alumina and the epoxy.

(2–3 cm instead of 6–10 cm) lens shape for BICEP3's 580 mm diameter elements, owing to alumina's higher in-band index of refraction ($n = 3.1$).

We developed an epoxy AR coating for all the alumina elements [27]. Stycast 1090 and 2850FT are vacuum mixed to obtain a homogeneous refractive index of $n = 1.74$, similar to the tunable epoxy mixing demonstrated in [28]. The epoxy is poured and rough-molded to 1 mm thickness on the alumina surface, then either machined (lenses) or abrasively ground (flat filter) to the final 0.452 mm thickness. Thickness of the alumina are controlled to less than 25 μm tolerance by referencing pre-coating surface measurements of the alumina. To avoid the fracturing and peeling of the epoxy AR coating due to differential thermal contraction during cryogenic cycling, the finished epoxy layer is laser diced into 1 cm squares with 30 μm-wide cuts across the entire area of the AR-coated lens and filter to achieve this stress-relieving square pattern (Figure 3.4).

Metal mesh edge filter

Metal mesh low-pass edge filters with a cutoff at 4 cm^{-1} are added to reject out-of-band signal [25]. These filters are made out of multiple randomly orientated metal grid layers, each of them is a thin polypropylene substrate coated with copper film, and hot-pressed fused together to form a shape cut-off edge filter.

The largest filter can be made is smaller than the require size for the BICEP3 focal plane [29]. In order to make sure all detectors are covered and protected, multiple filters are cut to small, 3" by 3" pieces, and they are individually placed directly on top of each detector module, and cooled to 280 mK. Combination of the fabrication process and increase machining on the filter's edges, we found delamination on the filter in 2016, which degrades the efficiency and shows non-uniform in band spectral response. All the metal-mesh filters are redesigned and replaced prior to 2017 season (Figure 3.5); Fourier Transform Spectroscopy shows the new filter gives a uniform in-band respond (Section 4.1) and increase in optical efficiency measurements indicate functioning filter.

3.2 Cryostat receiver

Cryostat

As shown in Figure 2.2, the BICEP3 cryostat receiver is a compact, concentric-cylinder design, that allows for large optical path while maintaining sub-Kelvin focal plane temperatures [27][30][31]. The outermost aluminum vacuum jacket is around 2.4 m tall along the optical axis and 74 cm in diameter (not including the extension supporting the pulsetube cryocooler). The cryostat weighs around 540 kg fully populated, without attached electronics subsystems. It maintains a high vacuum (~0.01 mTorr at base temperature) for thermal isolation and is capped at one end by the HDPE plastic window, as described in Section 3.1.

Cryogenic and thermal architecture

Within the room-temperature vacuum jacket are the nominal 50 K and 4 K stages, each comprised of cylindrical aluminum radiation shields and cooled by the 1st and 2nd stages of the pulsetube cryocooler, respectively. The stages are mechanically supported off each other and the vacuum jacket by low thermal-conductivity, G10 fiberglass members (a central truss and axial constraints at the ends of each cylindrical stage). Multi-layer insulation (aluminized mylar) minimizes the radiative heat transfer between the vacuum jacket and cryogenic stages.
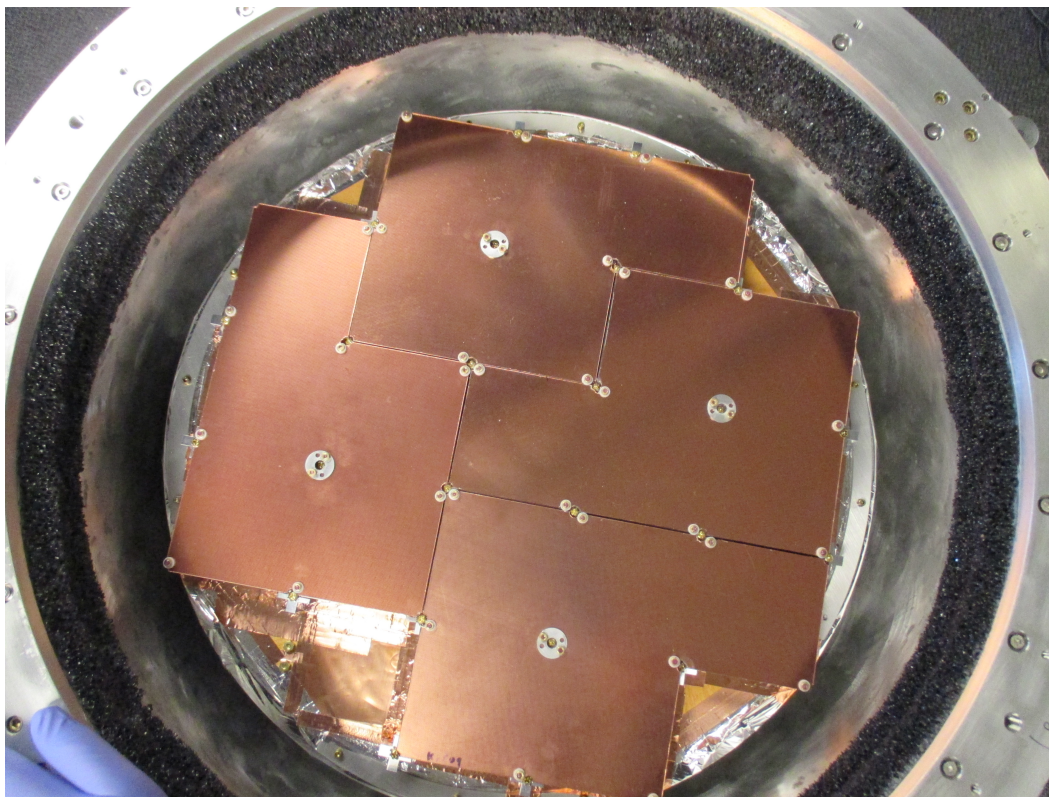
Figure 3.5: Metal-mesh filters mounted on BICEP3 in 2017. The filters are cut to bigger piece, each covering 5 detector modules to minimize the machining required for each filter. Mounting holes are carefully slotted to account for differential thermal contraction. New fabrication process is used for these filters, and each of them are cold tested before installing into BICEP3.

BICEP3 uses a single PT-415 pulsetube cryocooler[2], which provides continuous cooling to 35 K at the 1st stage under typical 26 W load and 3.3 K at the 2nd stage under 0.5 W load. A non-continuous, three-stage (He-4/He-3/He-3) helium sorption fridge[3] is heat sunk to the nominal 4 K stage and cooled the sub-Kelvin focal plane and supporting structures. The sorption fridge provided continuous sub-Kelvin operation on the focal plane for > 48 and > 80 hours for the 2016 and 2017 season, respectively, with 6 hours of recycling time. These hold time allow us to have a continuous two and three day observation schedule.

The focal plane and ultra-cold (UC) stage (nominal 280 mK) is a planar copper assembly mounted in a vertical stack on two buffer stages (nominal 350 mK and 2 K), each supported and isolated by carbon fiber trusses. The UC stage is comprised

---

[2]Cryomech Inc., Syracuse, NY 13211, USA (www.cryomech.com)
[3]Chase Research Cryogenics Ltd., Sheffield, S10 5DL, UK (www.chasecryogenics.com)

of the 9 mm thick, 46 cm diameter copper focal plane plate that supports the detector modules and a thinner secondary copper plate. The two plates are separated by seven 5 cm tall stainless steel blocks that serve as low-pass thermal filters and dampen thermal fluctuations before reaching the focal plane. Both the focal plane and the secondary UC stage are actively temperature controlled with resistive heaters to 274 mK and 269 mK, respectively. Thermal fluctuations on the focal plane during CMB observation are monitored and controlled by multiple temperature control modules (TCMs). The TCMs include two Germanium NTD thermistors, two heaters, bias and readout circuitry. The JFET readout for the NTDs is located in a readout module mounted to the 4 K baseplate.

Housekeeping

General thermometry uses silicon diode thermometers (Lakeshore[4] DT-670) and sub-Kelvin stages are measured with thin-film resistance temperature detectors (Lakeshore Cernox RTDs). Germanium NTD thermistors are mounted directly to the detector tile substrates for more sensitive measurements of the TES thermal bath temperatures, and they are used on both the focal plane and secondary UC stage for the active temperature control input (TCMs). The thermometry, heater, and thermal control signals interface to an external electronics 'backpack' mounted directly to the cryostat vacuum jacket that provides biasing, signal pre-amplification, and buffering. A BLASTbus2 ADC system [32] interfaces between the control computers and the backpack. Figure 3.6 shows the housekeeping schematic in BICEP3.

RF shielding

Several levels of RF shielding are designed into the 4 K stage and sub-Kelvin structure to prevent RF coupling to the detector signal. Except for the short length of flex ribbon cables that connect the detector modules to the focal plane, all cabling in the cryostat are twisted pair. The ribbon cables are caged by the detector module, copper focal plane module cutout, and the ground plane of the wiring board that accepts the cable. Upon exiting the cryostat, all of the detector signal lines immediately interface with a low-pass filtered connection on the MCE readout electronics box. The 4 K non-optics volume is designed as a Faraday enclosure, with all seams taped, and all cabling passing through additional low-pass filtered connectors. The cage continuously encloses the stack of sub-Kelvin stages by wrapping and sealing a single layer of aluminized mylar between the 4 K stage and

---

[4]Lake Shore Cryotronics, Westerville, OH 43082, USA (www.lakeshore.com)
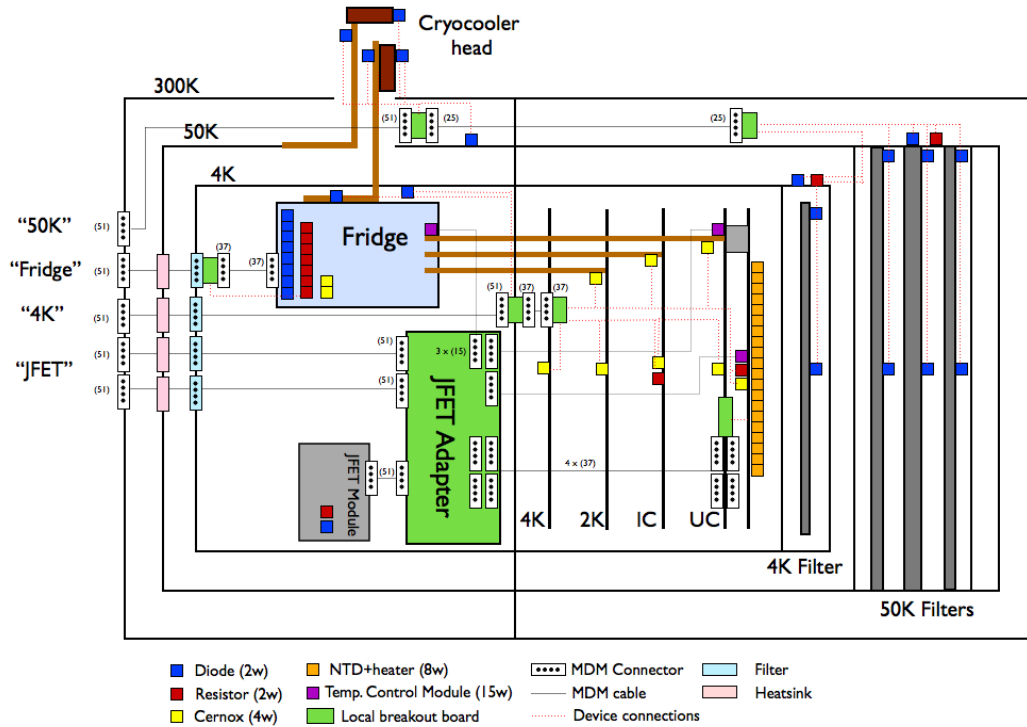
Figure 3.6: BICEP3 housekeeping schematic.

the edge of the focal plane (Figure 3.10). Finally, the niobium enclosure of each detector module, and detector tile ground plane, enclose the SQUID amplifier/MUX chips.

The cryostat tube acts as a waveguide with microwave frequency cutoff. But the larger diameter in BICEP3 is found to be susceptible to 450 MHz interference from the South Pole station radio system. The interference introduced an azimuth-synchronous signal, as well as transient disturbances to the feed-back based detector readout, and potentially contributed to increased $1/f$ noise within the science band. Reduced output power and installation of a directional antenna at the main South Pole station emitter in 2017 reduced the radio signal by 35 dB, resulting in the RF signal to be a sub-dominate effect in the science band.

Magnetic shielding

Magnetic shielding is crucial to minimize coupling to the SQUID amplifiers while the telescope scans through the Earth's field. Cryostat-level shielding is composed of cylindrical, high-permeability Amuneal[5] A4K layers, with open ends to avoid

---

[5]Amuneal Manufacturing Corp (www.amuneal.com)
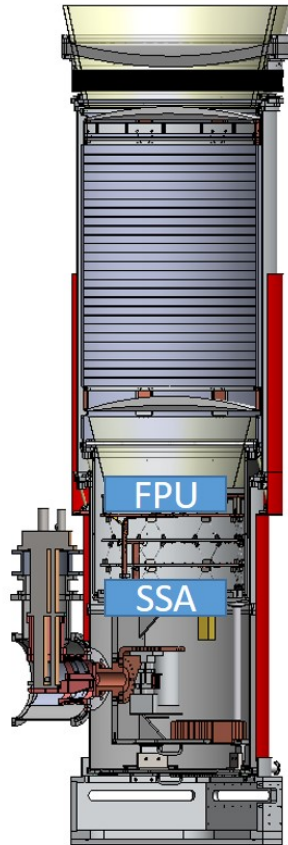
Figure 3.7:   Magnetic shield in BICEP3. The 50 K A4K is highlighted in red (the 300 K vacuum jacket are not shown), as the location of the second-stage SQUID series array (SSA), and the first-stage SQUIDs inside the detector module. The SSA are packaged in niobium boxes and further shielded by Metglas.

interference with the optics and allow data cabling at the bottom. There is one layer on the inner surface of the vacuum jacket spanning the length of the cryostat, and a second, shorter layer on the 4 K stage surrounding the focal plane (Figure 3.7). Laboratory Helmholtz coil measurements of these cylindrical shields in BICEP3 shows a shielding factor of ~30 along the optical axis. The niobium detector module housing provides further shielding of the first-stage SQUID amplifier chips on the sub-Kelvin focal plane, as described in Section 3.3. The second-stage SQUID series arrays on the 4 K stage are packaged in niobium boxes and additionally wrapped with ~10 layers of Metglas 2714A[6]. Section 4.6 shows the magnetic shielding performance in BICEP3.

---

[6]Metglas Inc., (www.metglas.com)
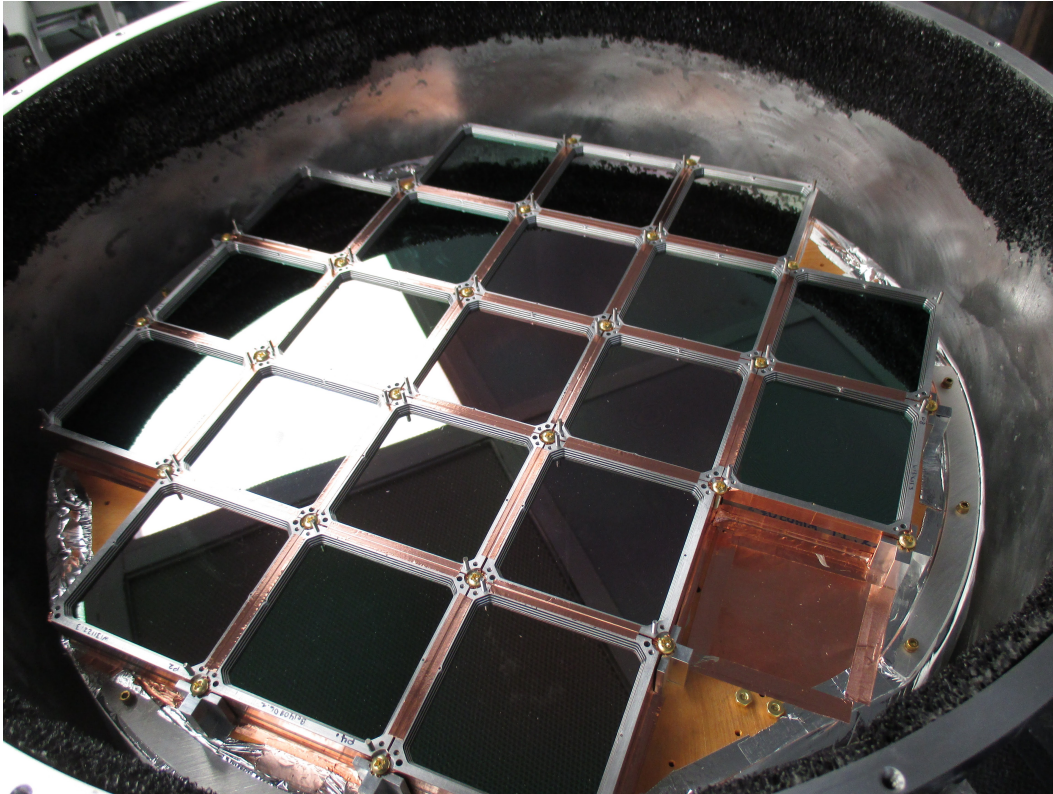
Figure 3.8: Bicep3 focal plane with 20 tiles.

3.3 Focal Plane

Bicep3 has 2560 detectors, more than a factor of eight greater than a single *Keck Array* receiver in the same frequency. These detectors are fabricated onto 20 silicon tiles, each housed 128 polarization sensitive transition-edge sensors. We use a modular packaging design of detector tile and readout hardware on the focal plane. It is constructed to provide the necessary thermal stability, magnetic shielding and mechanical alignment to operate the detectors, while at the same time allow us to replace individual tile without affecting the well-performed, existing one.

The detectors, sub-Kelvin readout electronic, and wire bonding are contained in the $79 \times 79 \times 22$ mm detector module which the footprint is dominated by the detector tile itself. This self-contained, compact design, allows us to maximize the focal plane real estate for the detector pixels [33]. Furthermore, each detector module can be quickly connect and heatsink to the main focal plane by its connectorized flex cables and mechanical fasteners, allowing true modularity and *ex situ* repairs.
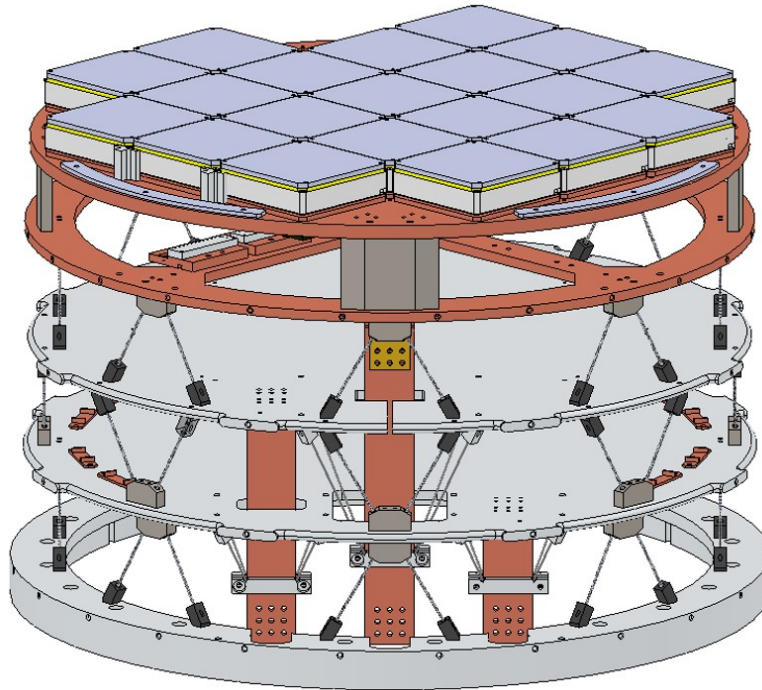
Figure 3.9: Sub-Kelvin structure in Bɪᴄᴇᴘ3. The bottom ring is connected to the 4 K structure of the receiver. The two middle plate is at 2 K and 350 mK, respectively. The copper structures are thermally connected to the 250 mK stage of the fridge. Each of these temperature stages are thermally isolated by 8 pairs of carbon fiber trusses. 7 stainless steel standoff, are mounted between the two copper plates as an thermal low pass filter.

Sub-Kelvin structure and copper plate

The sub-kelvin structure is mounted on the space above the sorption fridge. It contains three different thermal stages, at 2 K, 350 mK (IC), and 280 mK (UC). Each stages are thermally isolated using 8 pairs of carbon fiber truss structure. Copper heat straps are connected between the sorption fridge to these three stages. All the readout and housekeeping cables are heatsunk onto these stages to reduce the thermal load at the focal plane, which is temperature controlled at 280 mK (Figure 3.9).

All the detector modules are mounted to a support plate made from a gold-plated, oxygen-free high thermal conductivity copper (OFHC) plates, which itself is mounted to a second plate separated by stainless steel passive thermal filters. Active temperature control modules are placed onto both copper plates to maintain sub-millikelvin stability over observation cycles. The entire enclosure is then warped and sealed with a single layer of aluminized mylar to form a Faraday enclosure (Fig-
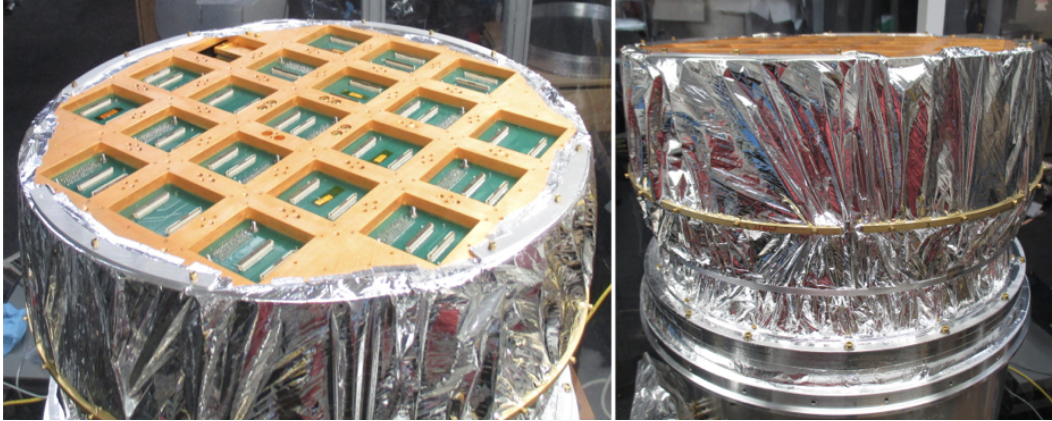
Figure 3.10: Faraday enclosure in BICEP3 sub-Kelvin stages. The entire sub-Kelvin stages is enclosed by a thin layer of aluminized. All the cabling coming out from the bottom of the stages are pass through a filter. The readout circuit boards at the top of the stage have a ground plate installed.

ure 3.10).

Modular packaging

The detector module consists of a quartz anti-reflection coating, detector tile, niobium (Nb) $\lambda/4$ backshort, A4K magnetic shield, 1st stage superconducting quantum interference device (SQUID) chips, and the readout circuit boards (Figure 3.11).

A single silicon tile contains 124 detectors in a 8×8 dual polarization format. Each tile, the detectors at the four corners are left dark. Dark detectors consists of the complete TES island structure, but are not connected to the slot antenna array. They allow us to measure detector properties without the influence of incoming optical power (Section 4.3). Eight dark SQUID channels in each tile are also connected to calibrate readout noise and crosstalk level.

The readout circuit board inside the module connects between the MUX and NYQ chips (Section 3.5) and the detector wafer. It consists of a standard FR4/Cu PCB with two 60-pin, 0.5 mm pitch, zero-insertion force (ZIF) surface-mount connectors, and a alumina circuit board with superconducting aluminum traces (Figure 3.12).

The MUX/ NYQ chips are mounted onto a 0.01" thick alumina circuit board, the similar coefficient of thermal expansion between silicon and alumina allow us to directly mount these chips onto the circuit board. Although in reality the chips are installed on top of a alumina carrier to create a bigger distance between the chips and the high-μ magnetic shield behind the alumina board. The superconducting

Cu Heatsink

External Nb Shield

Nb Housing

PCB Circuit Board
w/2x 60pin connectors

Alumina Circuit Board

SQUIDs & Nyquists
On Alumina Carriers (6 Columns)

High μ magnetic shield

$\lambda/4$ Nb Backshort

Detector Tile (8x8 pixels)

Z-cut Quartz AR Tile

Aluminum Detector Frame
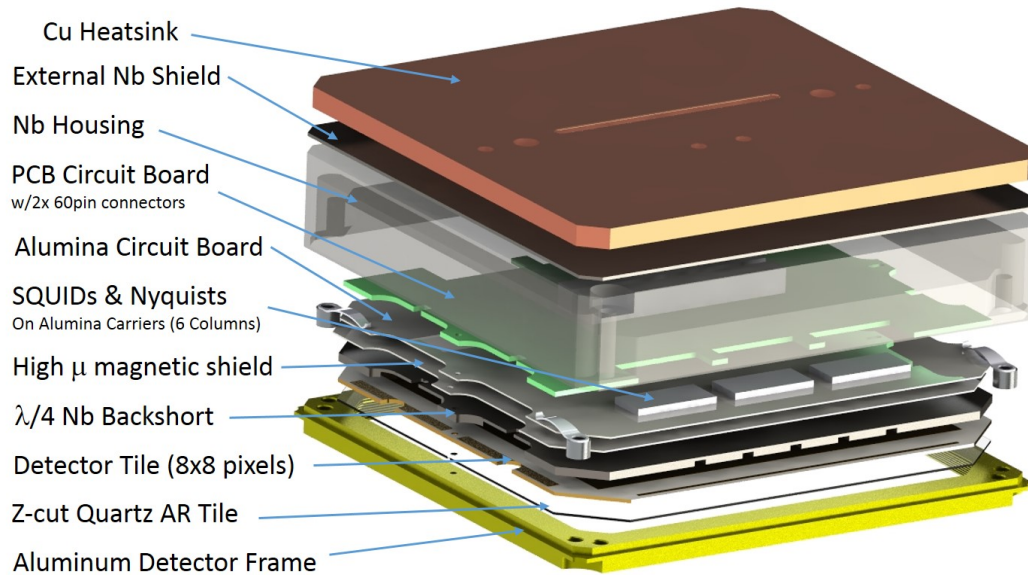
Figure 3.11: Exploded view of the BICEP3 detector module. Sky-side is facing downward in this diagram. The multiplexing SQUIDs and circuit boards are mounted directly behind the detector wafer, separated by a $\lambda/4$ Nb backshort and A4K magnetic shield. The backside is enclosed by a Nb cover and plate for magnetic shielding performance.
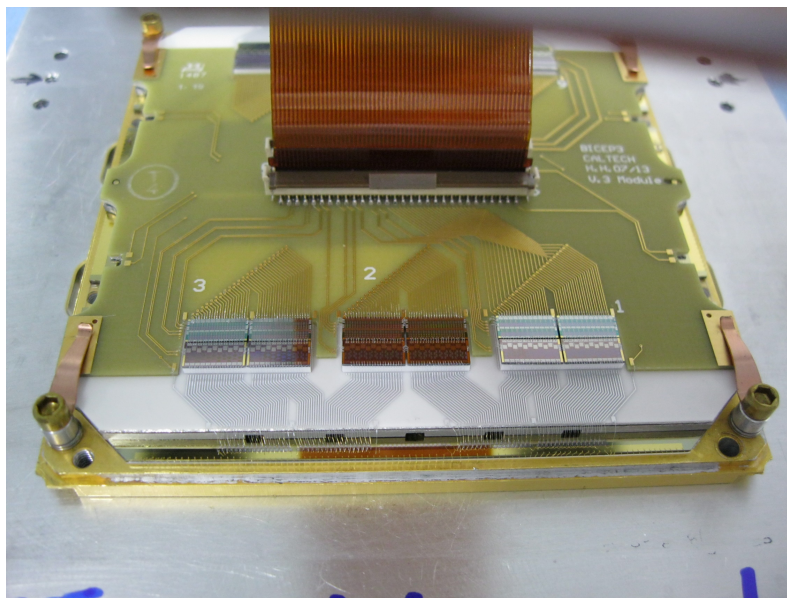
Figure 3.12: Backside of the detector module. Aluminum wirebonds connected the detectors to SQUIDs chips via an alumina circuit board. Two 60-pins Kapton/Cu flex-circuit ribbon cables connected to the ZIF connectors and traveled out of the niobium casing through a thin slot to matching connectors on the focal plane.

aluminum traces between the chips and detector wafer ensure no extra resistance is added from the TES to the SQUID amplifier. The alumina board are too fragile to install the connector soldering, an extra FR4/Cu PCB is added into the circuit layout.

This focal plane design utilized the entire optically illuminated focal plane area, and at the same time kept the diameter of the overall cryostat compact. The absence of a tower-like structure similar to SPT makes the overall height of the cryostat smaller, allow faster cool down and easier procedure [34]. One of the challenges in this design is the connection between the detector wafer and the alumina circuit board. These two components are separated by the $\lambda/4$ backshort, and a 508 μm magnetic shield. Together they resulted the wirebond from the detector to the alumina at $\sim$ 2mm.

Thermal sinking and magnetic shielding

The detector tiles are thermally sunk to the aluminum frame with ~500 gold wire-bonds at all four sides to maintain a stable and uniform bath temperature for the TES bolometers. The gold wirebonds are densely packed to create an RF-tight shield between the aluminum frame and the detector wafer. The module is mounted to a copper heat-sinking piece at the back of the housing only making thermal contact at the center of the niobium. This contact point ensures the niobium transitions into the superconducting stage starts from the center, then expands outward to avoid trapped magnetic flux during cool down.

Combination of the niobium housing and a sheet of high-μ Metglas 2714A inside the module provides a low-field environment around the SQUID chips. Simulation using COMSOL Multiphysics[7] showed the residual magnetic field is <1 % at the location of the SQUID chips (Figure 5.2).

Corrugation frame

The interaction between the slot antenna and the surrounding metal frame causes a differential pointing between the polarization detectors. This causes >15% near field mismatch on the pixel closest to the metal frame. Although most of these systematics are removed during analysis [35], a corrugated frame is designed to minimize the pointing offset (Figure 3.14).

The corrugated wall acts as an open circuit to the nearby antenna structure. Simula-

---

[7]COMSOL, Inc., Burlington, MA 01803 (`www.comsol.com`)
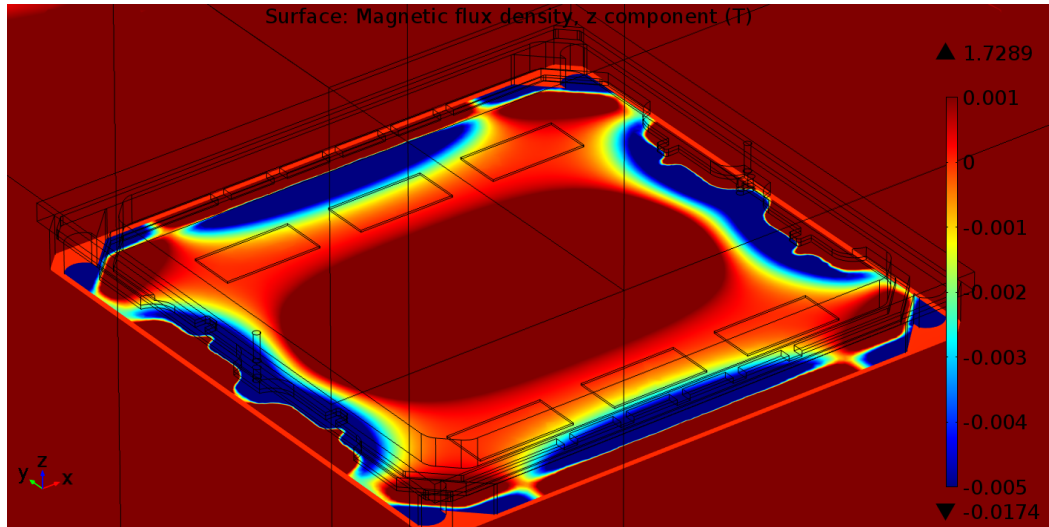
Figure 3.13: COMSOL Multiphysics simulation. The simulation shows the residual magnetic field is <1 % at the location of the SQUID chips
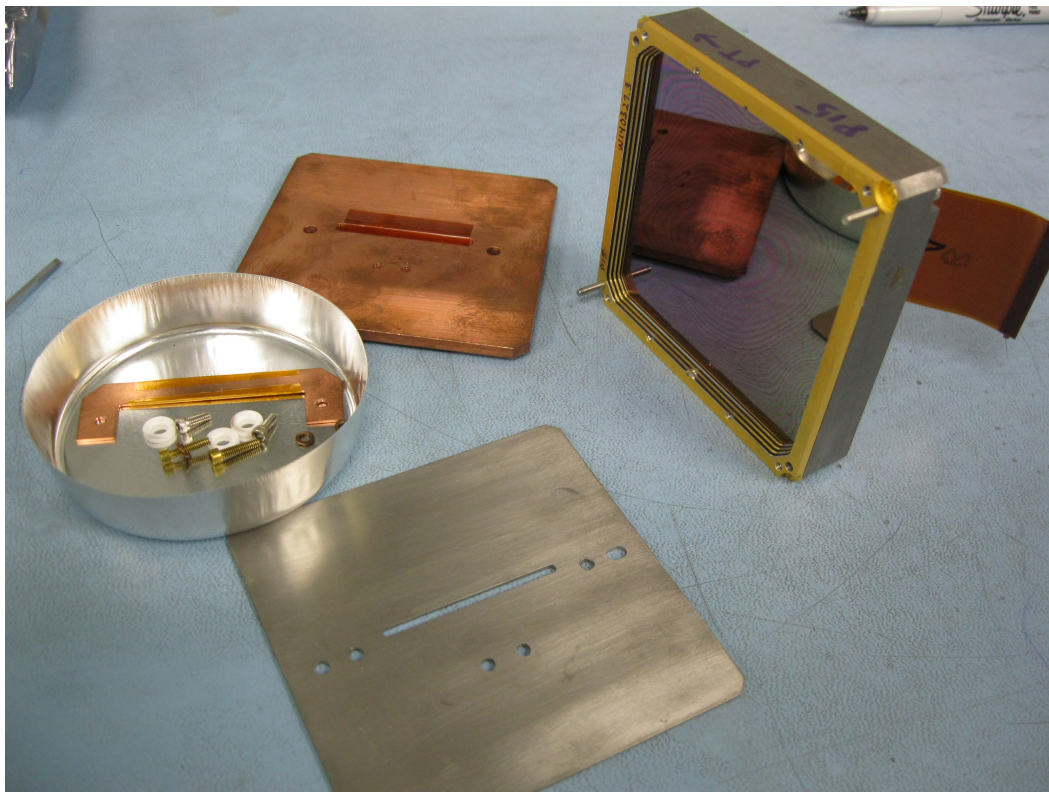
Figure 3.14: Front side of the module, and copper heat sink. The corrugation is visible on the frame. The back copper and niobium plate are uninstalled, the slot in these plate allow the flex cables feeding.

tion shows a ~6% near field pointing offset over 25% bandwidth after implementing this design.

3.4 Detectors

We use Antenna-couple transition edge sensor (TES) bolometers fabricated at Caltech/JPL [36][37][38][39]. These detectors are entirely planar and do not require horns and other coupling optics. The optical power couples to two co-located, orthogonally polarized 8×8 planar antenna arrays, each composed of slot sub-radiators patterned in a superconducting niobium (Nb) ground plane. All slots of a given orientation are coherently combined through a microstrip summing tree to synthesize a single equivalent antenna for that polarization orientation. Power from each antenna is passed through an on-chip band-defining filter before being dissipated on a suspended bolometer island. A TES voltage biased into its superconducting-normal transition on that island detects variations in the power received by the antennas. The bolometer design are detailed in [40], this section focuses on the tapering modification used in BICEP3.

Tapered antenna networks

The antenna slots in each detector are spaced to Nyquist sample the focal plane surface to avoid grating lobes:

$$s \leq \frac{\lambda_{o,\min}}{\sqrt{\epsilon_r}} \left(1 - \frac{1}{N} \right) \tag{3.1}$$

where $\lambda_{o,\min}$ is the minimum wavelength of operation, ϵ_r is the relative permittivity of the surrounding medium, and N is the number of elements per linear dimension. For BICEP3, the detectors are fabricated on silicon ($\epsilon_r = 11.8$), with the upper band edge at 110 GHz, in a 8×8 dual-slot cub-arrays tile format (Figure 3.15). The slots are 900 μm apart, and the offset slot-pair geometry allows the two orthogonally polarized antenna arrays within each detector pair to be co-located.

We oriented the tiles with the silicon substrate side toward the sky and then terminated the back response on the vacuum side with a $\lambda/4$ backshort, since it is energetically more favorable for the antennas to receiver power thought silicon.

The simplest design to couple optical radiation to our detectors through a planar phased antenna array, used in BICEP2/*Keck Array*, drive each of the array's sub-antennas with equal field strength, synthesizing a top-hat illumination and thus a sinc pattern in the far field. Such a pattern has side-lobes with peak levels at -13 dB
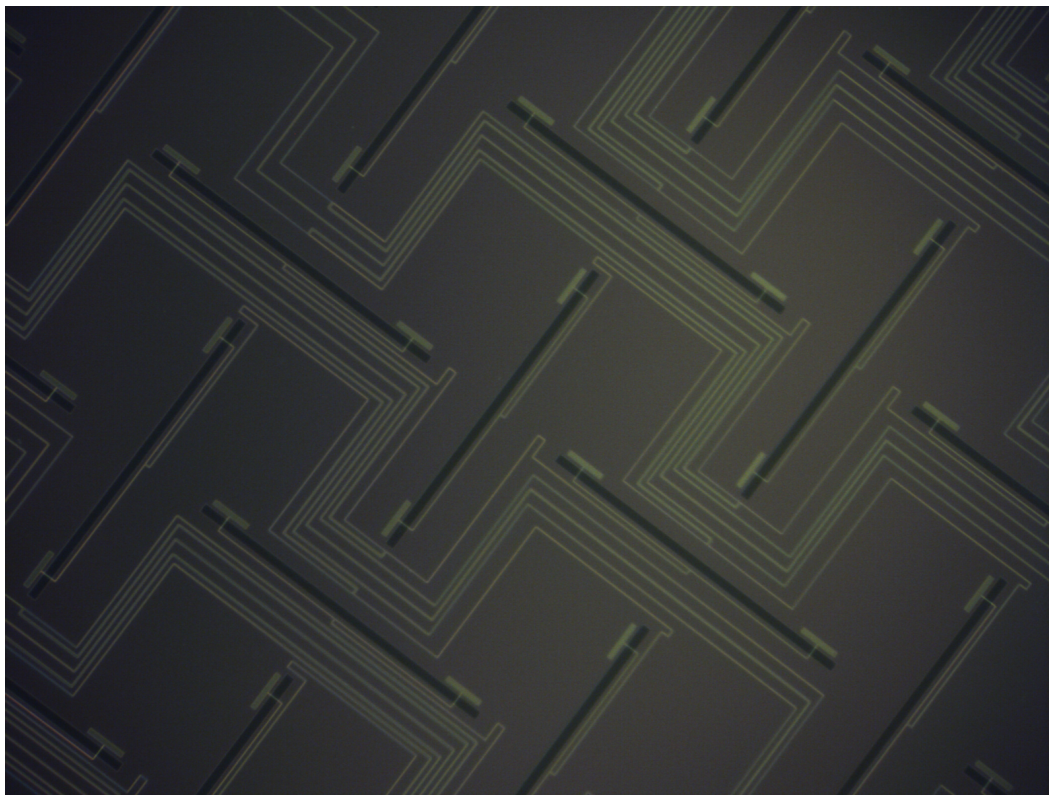
Figure 3.15: Microscope photograph of antenna network. Most of the space is occupied by the summing tree network. The dual polarization slot antennas are shown in black in the photograph.

below the main lobe. In these instruments, those side-lobes are terminated onto a 4 K stop with limited impact on the sensitivity.

Programmatically, some instruments would benefit from lower side-lobe levels and BICEP3 is used to advance this capability. The side-lobe levels of antenna arrays can be controlled by tapering the illumination such that the central radiators couple to higher intensity than those at the edge. We can generalize the array factor with non-uniform illumination E_m as

$$
\begin{aligned}
A(\theta) &= \sum_{m=-(N-1)/2}^{(N-1)/2} E_m e^{-jmk\sin(\theta)s} \\
&\simeq \int_S dx'\,dy'\,E(x',y')e^{j(k_x x'+k_y y')}
\end{aligned}
\tag{3.2}
$$

where the last line approximates the sum as an integral across the antenna's total aperture. k_x and k_y are the components of the tangential free-space wavevector $k\sin(\theta)$.
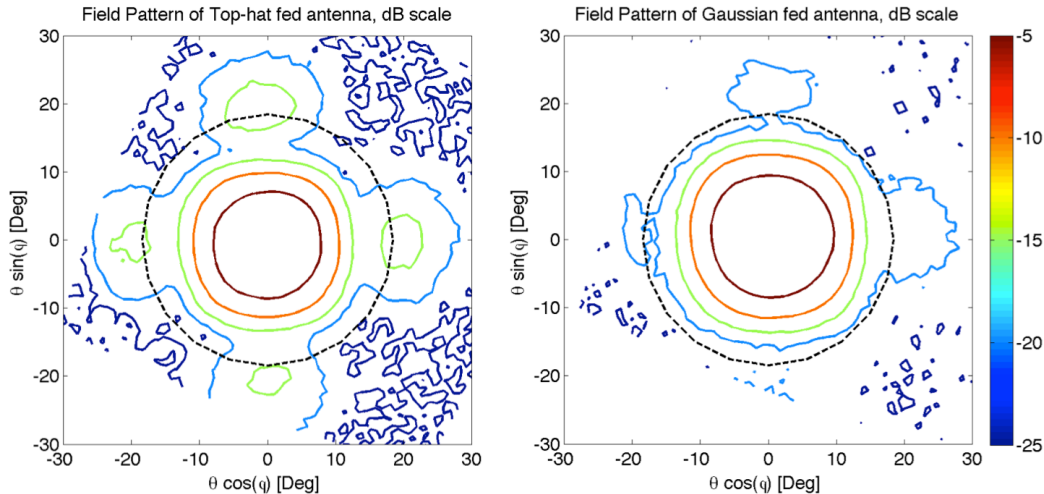
Figure 3.16: Measured far-field detector pattern. These beam patterns are mapped with a thermal source, and no imaging optics, thus show the far-field response of the detector. Left: A typical detector response from *Keck Array*. The antenna slots are uniformly illuminated. Right: A tapered antenna design used in BICEP3. The main beam is widened, but the sidelopes level are suppressed. The dotted lines in the figure show the design optical stop in the telescope.

This expresses the far-field antenna pattern, incident upon the camera's stop, as the fourier transform of the illumination pattern. For BICEP3, we have designed antenna feeds that generate a gaussian illumination with an electric field waist radius of 6.3 mm; compared to the physical aperture size of 7.5×7.5 mm. This reduces the side-lobe levels to -16 dB and the integrated spillover to 13% compared to the 17% that would have been achieved with a uniform feed (Figure 3.16). The result is an illumination that is close to uniform, as the instrument's 4 K stop requires, but also allows us to develop flexibility for other instruments.

The illumination pattern is controlled through the microstrip feed network that sums waves from the sub-antennas to deliver power to the TES bolometer. Were our 8x8 sub-antennas fed uniformly, all microstrip-T junctions would have summed power with equal weighting. Instead, the power ratios required are numerically chosen to synthesize the required gaussian profile.

Band-defining filters

Each microstrip feed contains an integrated band-defining filter between the antenna feed and bolometers. We use a three-pole design filter, shown in Figure 3.17. We realize the resonators with lumped components, which do not suffer from the high
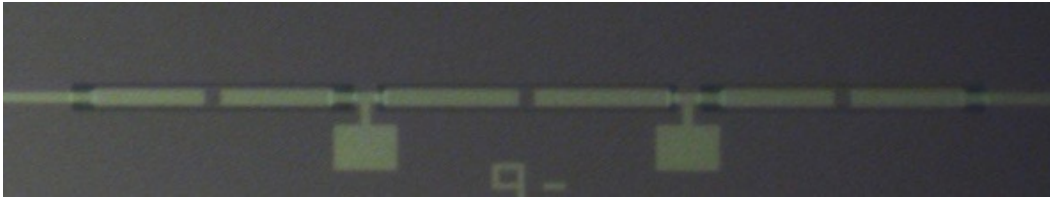
Figure 3.17: Microscope photograph of filter

frequency resonant leaks present in $\lambda/2$ or $\lambda/4$ transmission line resonators.

Each pole is a series LC resonator, the inductors are short stretches of high-impedance coplanar waveguide (CPW). The series capacitors are parallel-plate metal-insulator-metal between upper and lower niobium films using the microstrip SiO_2 as the dielectric.

TES bolometers

TES bolometer review

A TES bolometer measures the radiation coupled from the antenna and read out the temperature. This section gives an overview of TES theory, largely following the review in [41]. TES bolometer uses the non-linear relationship between resistance and temperature of a superconducting material during transition. During the transition, the resistance is steeply depend on the temperature, such that a small temperature change results in a large resistance change.

When the TES is biased at a constant voltage, it is stably in negative electro-thermal feedback. An incoming photon hits the bolometer, resulting in an increase of the detector temperature. This causes increase in resistance, thus decrease in current, which decreases the power dissipated on the TES from electrical Joule power and the TES remains in transition.

In this strong electro-thermal feedback stage, the change in optical power is nearly equal to the change in electrical power. The response s of the current I of the TES is linear to the changes in optical power P:

$$s = \frac{dI}{dP} = \frac{-dI}{dP_J} = -\frac{1}{V} \tag{3.3}$$

The response of the TES is determined by the thermal and electrical differential equations. The thermal equation determines the temperature T and the electrical
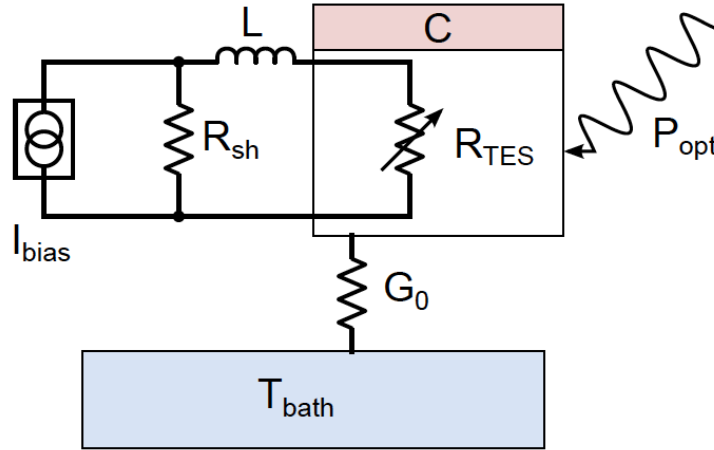
Figure 3.18: Sample TES bolometer diagram. The TES is biased at a constant voltage by being wired in parallel to a shunt resistor much smaller than TES resistance. The bolometer island is weakly couple to the thermal bath with conductance G set by the legs and heat capacity C by the thick gold film [42].

equation shows the current I. Conservation of energy governs the thermal equation:

$$C\frac{dT}{dt} = -P_{\text{bath}} + P_{\text{opt}} + P_J \tag{3.4}$$

where C is the thermal capacity, P_{bath} is the thermal power from the weak coupling from the bath, P_{opt} is the optical power, and P_J is the electrical Joule power.

The electrical differential equation is Ohm's law:

$$L\frac{dI}{dt} = (I_{\text{bias}} - I)\, R_{sh} - IR_{\text{TES}} \tag{3.5}$$

where L is the inductance, I is the current through the TES, I_{bias} is the bias current, R_{sh} is the shunt resistor, R_{TES} is the electrical resistance of the TES, which generally is a function of both temperature and current.

In small-signal limit around the steady-state values of resistance, temperature, and current (R_0, T_0, I_0); the thermal power flow to the bath is a function of the thermal conductance G connecting the bath with the island, and temperature T:

$$P_{\text{bath}} = K\left(T^n - T_{\text{bath}}^n\right) \approx P_{\text{bath}_0} + G\delta T \tag{3.6}$$

where the exponent $n = \beta + 1$ that β is the thermal conductance exponent, the prefactor $K = G/n(T^{n-1})$ with thermal conductance G and $\delta T = T - T_0$.

We can define the logarithmic derivative of the resistance and current versus temperature as:

$$\alpha = \frac{\partial \log R}{\partial \log T} \tag{3.7}$$

$$\beta = \frac{\partial \log I}{\partial \log T} \tag{3.8}$$

The resistance of the TES R_{TES}, becomes

$$R_{\text{TES}} = R_0 + \alpha \frac{R_0}{T_0} \delta T + \beta \frac{R_0}{I_0} \delta I \tag{3.9}$$

and the dynamic resistance R_{dyn} at a constant temperature is

$$R_{\text{dyn}} = \frac{\partial V}{\partial I} = R_0 (1 + \beta) \tag{3.10}$$

The Joule power P_J can be expanded to first order around the steady-state

$$P_J = I^2 R \approx P_{J_0} + 2 I_0 R_0 \delta I + \alpha \frac{P_{J_0}}{T_0} \delta T + \beta \frac{P_{J_0}}{I_0} \delta I \tag{3.11}$$

with electro-thermal feedback loopgain $\mathcal{L}$:

$$\mathcal{L} = \frac{P_J \alpha}{G T_0} \tag{3.12}$$

and natural thermal time constant τ:

$$\tau = \frac{C}{G} \tag{3.13}$$

Together, we get the linearized differential equation, which can be represented in matrix format:

$$\frac{d}{dt} \begin{pmatrix} \delta I \\ \delta T \end{pmatrix} = - \begin{pmatrix} \frac{1}{\tau_{el}} & \frac{\mathcal{L} G}{I_0 L} \\ -\frac{I_0 R_0 (2+\beta)}{C} & \frac{1}{\tau_I} \end{pmatrix} \begin{pmatrix} \delta I \\ \delta T \end{pmatrix} + \begin{pmatrix} \frac{\delta V}{L} \\ \frac{\delta P}{C} \end{pmatrix} \tag{3.14}$$

that $\delta P = P - P_0$ and $\delta V = V_{\text{bias}} - V_0$ shows the small power changes and the result small voltage bias changes around the steady-state, respectively. $\tau_{el} = \frac{L}{R_L + R_{\text{dyn}}}$ is when the limit of $\mathcal{L} = 0$, and in the limit of $\delta I = 0$, $\tau_I = \frac{\tau}{1-\mathcal{L}}$.

Bolometer design

In BICEP3, the millimeter-wave power are terminated and thermalized on a released bolometer island in a meandered lossy gold microstrip (Figure 3.19). The power is
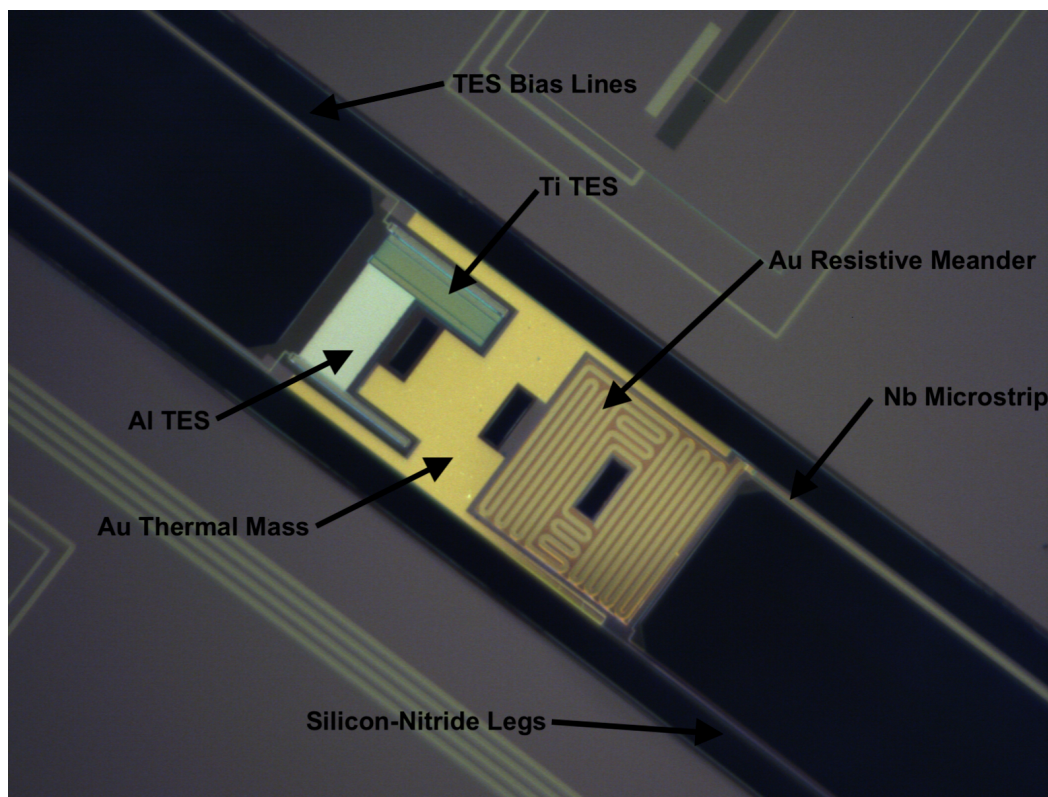
Figure 3.19: A TES bolometer in BICEP3. The gold-meandered microstrip termination is at the right of the photograph and the TESs at left. The thick gold in the middle ensures thermal stability. The bolometer island is suspended from the tile by four isolation legs.

constrained to propagate through a length of several wavelengths and has less than -20 dB return loss.

The bolometer island is suspended from the tile by four isolation legs: one carrying the microstrip from the antenna, and two carrying the TES DC bias lines. The thermal conductance G of the bolometer is determined by the geometry of the supporting legs. It is important to design a high enough G so the detectors do not saturate under typical sky loading. At the same time, phonon noise is the largest noise source in the bolometer after photon noise, which increase with thermal conductance.

The thermal power flowing to the bath P_{bath}, or the saturation power of the detector, can be written in terms of bath temperature T_0 and transition temperature T_c:

$$P_{\text{bath}} = P_{\text{sat}} = G_c T_c \frac{1 - (T_0/T_c)^{n+1}}{n+1} \tag{3.15}$$

where the conductance G_c is evaluated at the transition temperature, the exponent n

shows the thermal carriers in the thermal legs, $n = 1$ represents a electrons dominate and $n = 3$ correspond to phonons in 3D material, our deceives are described $n \sim 2.1$. We also added thick evaporated gold to the bolometer islands to boost the heat-capacity, so the time constant $\tau = C/G$ is about a millisecond.

The typical on-sky loading condition for Bicep3 is about 2 pW at 95 GHz, the detector is designed to have a safety factor of 2.5, resulting in designed $G_c = 30$ pW/K and the saturation power $P_{\text{sat}} = 5$ pW.

The termination is in close thermal contact with two TESs. The aluminum TES with a transition temperature $T_c \sim 1.2$ K for lab tests and a ~ 60 mΩ titanium TES with $T_c \sim 0.5$ K for science observations. The aluminum T_c allows the bolometer a high saturation power for use under a room temperature background, but the titanium T_c has better noise performance for sky observation.

The TESs are voltage biased into the transition at half the normal resistance R_n, using a 3 mΩ shunt resistor at the Nyquist chip in the SQUIDs package, and the changes in the TES current are readout by the time-domain multiplexing SQUID architecture (Section 3.5).

3.5 Detector Readout

Bicep3 uses a time-domain multiplexed (TDM) system developed at NIST for the bolometer readout [43]. The readout electronics consist of the Nyquist chips (NYQ), SQUID multiplexing chips (MUX) and the SQUID series array (SSA). The NYQ chips are used to voltage bias the detectors with a 3 mΩ shunt resistor with a 2 μH inductors to limit the bandwidth. The MUX chips contain the first stage of the SQUID multiplexer, and the SSAs provide the final SQUID amplifier stage. The NYQ and MUX chips are located inside the module cooled to 280 mK, while the SSAs are attached to the 4K temperature stage. A Multi-Channel Electronic (MCE) system developed by the University of British Columbia controls the bias and readout of all the channels [44].

The multiplexing architecture is $22 \times 30 \times 5$: 22 TESes are read out in a multiplexer row and there are 30 multiplexer columns to form a MCE unit. Each set of the NYQ-MUX chip corresponds to a signal column and 11 rows, 2 chips are connected to form the 22 row multiplexing set, and 6 of these sets are mounted inside each module. 5 modules connect to a circuit board behind the focal plane (distribution board) to group all 30 columns. The row select lines are wired in series for every 5 modules. Superconducting niobium-titanium, twisted-pair cables connect the focal
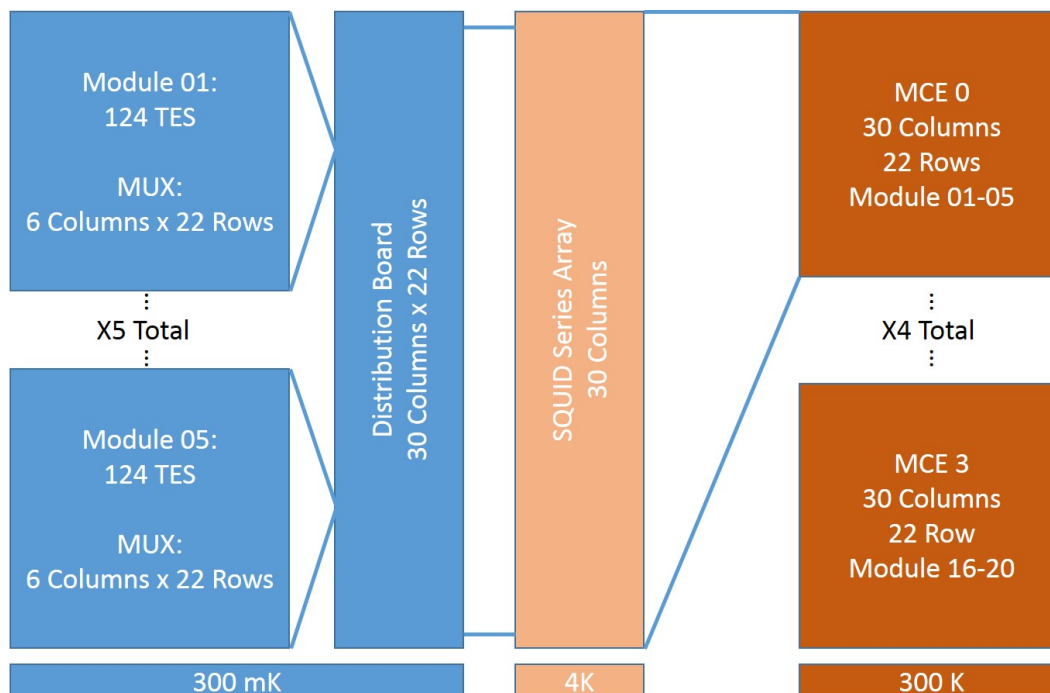
Figure 3.20: Readout schematic of BICEP3. Every 5 modules are grouped and connected to a distribution board behind the focal plane at 280 mK, then to the SSA at 4 K, and connected to the room temperature MCE. 4 MCEs are used to readout all 20 tiles (2560 channels).

plane, and SSAs at 4 K. They are readout by a MCE unit attached to the cryostat at 300 K. Four independent MCE units read out all 20 modules. Figure 3.20 shows the block diagram of the readout schematic.

SQUID Amplifier and Multiplexer

The SQUIDs play several simultaneous roles in our readout system. They amplify the small current output of the TESes while adding noise sub-dominant to the TES itself. They transform the small ~60 mΩ impedance of the TES to levels that warm amplifiers can match. Lastly, they have sufficient bandwidth to allow multiplexing of several detectors on common readout lines.

Each independent detector is inductively coupled to a signal SQUID array (SQ1) by an input coil and the amplifier is operated in flux-lock loop to linearize the periodic output and increase the dynamic range of the SQUIDs response. As the flux from the input coil changes in response to the TES current, a compensating flux is applied by the feedback coil to cancel it. This flux feedback serves as the output of the TES channel. The SSA provides an additional stage of amplification that
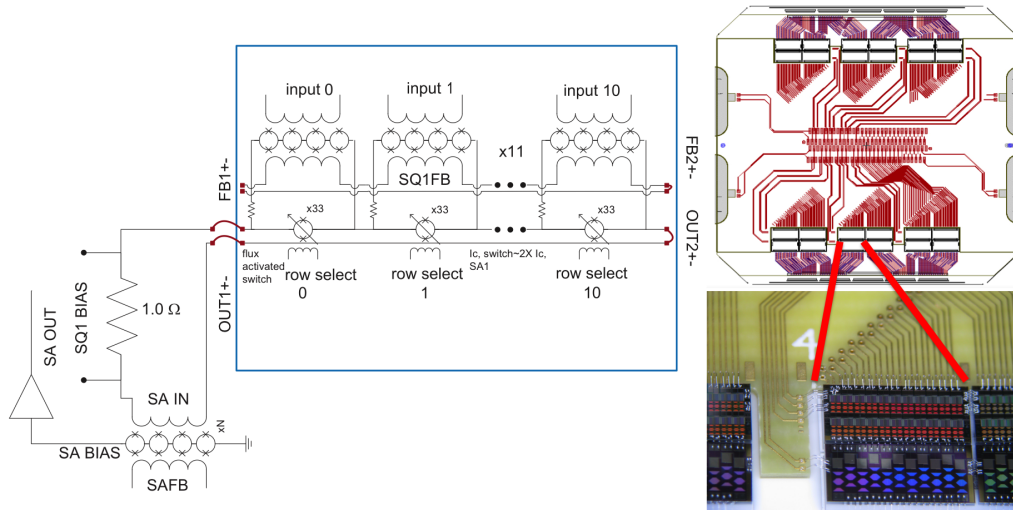
Figure 3.21: Simplify readout circuit diagram for Bɪᴄᴇᴘ3.

provides the aforementioned impedance matching between the first stage SQUIDs and room temperature MCE, providing $\sim 1\Omega$ dynamic resistance for a $\sim 100\Omega$ output impedance. Figure 3.21 shows a simplified schematic of the SQUID amplifier system. A similar design is used Bɪᴄᴇᴘ2/*Keck Array* and many other experiments.

Time Domain Multiplexing is possible because the SQ1 will not generate output signal when it is biased below its critical current I_{min}. Each SQ1 couples a TES to a shared common readout amplifier (SSA). While the TESes are continuously biased, they are only sampled when the corresponding SQ1 channel is biased. This allows our readout system to sequentially read 22 detectors in a common column, revisiting frequently enough to nyquist sample the highest relevant frequencies in the time-stream.

Each SQ1 bias in a signal column is controlled by a superconducting-to-normal flux activated switch that biases in parallel with the SQ1 and is controlled by the 22 row-select (RS) input lines. This design differs from that in Bɪᴄᴇᴘ2/*Keck Array* where the RS input lines separately biased each row of SQ1s, requiring an extra per-column intermediate summing coil and SQUID (SQ2) before reaching the SSA.

The flux activated switch is designed to switch at twice the critical current of the SQ1s, allowing the switches to share the same bias line with SQ1 in Bɪᴄᴇᴘ3. This ultimately reduces the electrical wiring going into the cold stage of the focal plane.

Control of the MUX system and feedback-based readout of the TES data are via

Table 3.5: Summary of multiplexing parameters used in Bicep3.

Raw ADC sample rate	50 MHz
Row dwell	90 samples
Row switching rate	556 kHz
Number of rows	22
Sample-row revisit rate	25.3 kHz
Internal downsample	168
Output date rate per channel	150 Hz
Software downsample	5
Achieved data rate	31.1 Hz

the room temperature Multi-Channel Electronics (MCE) systems. The multiplexing speed needs to be quick enough for the Nyquist frequency to exceed the noise bandwidth to avoid aliasing penalty. Bicep2/*Keck Array* shows the optimal multiplexing speed is 25 kHz with a 2 μH bandwidth limiting inductor. The data are filtered and down sampled in the MCE before being output to the computer software. The MCE uses a fourth-order digital Butterworth filter before down-sampling by a factor of 168, the control software applies a second stage of filtering using an acausal, zero-phase-delay FIR filter to down sampled by another factor of 5, giving a final sample rate of 31.1 Hz. The full multiplexing parameters used in Bicep3 are shown in Table 3.5. We described the performance of the SQUID readout in 4.5. Figure 3.22 shows the SSA module installed at the 4 K stage of the cryostat, above the 3He fridge.
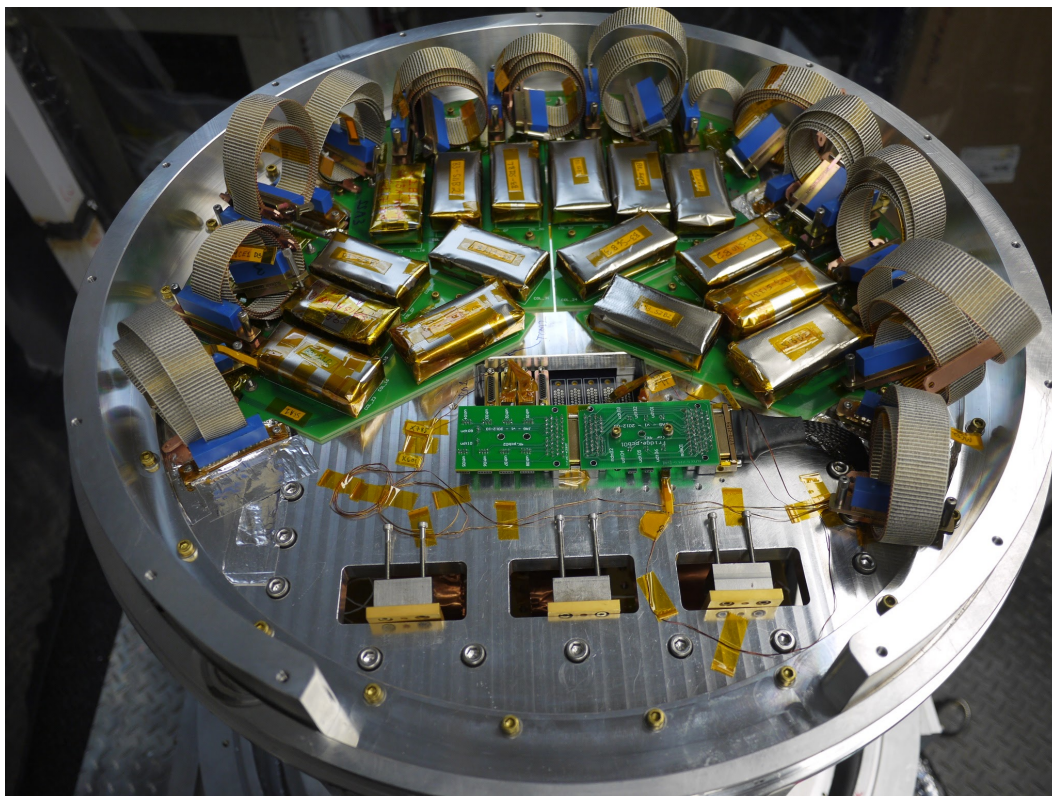
Figure 3.22:   SSA modules and circuit boards in BICEP3. This is installed above the 3He fridge, and separated into four identical parts, each connected to one MCE. Each board has 4 SSA modules, together providing 32 columns of readout. They are connected to the focal plane via three 100-way NbTi cables on each board. The bottom of the picture also shows the disconnected sub-Kelvin heat straps, and some housekeeping thermometry circuit boards.

Chapter 4

BICEP3 INSTRUMENT CHARACTERIZATION

Measurement of CMB polarization requires careful characterization of the instrument. We conducted a number of calibration measurements on BICEP3, both in-lab and at the South Pole. This chapter describes some of the critical measurements, focusing on efficiency and noise performance of the telescope, and various aspect that would limit our systematic control.

4.1 Detector spectral response

The end-to-end detector spectral response is a combination of the antenna, band-defining filter and low pass edge filter (Section 3.4 and 3.1). The band is chosen to avoid the board oxygen absorption band around 60 GHz, as well as the spectral lines of oxygen at 118.8 GHz.

Spectra of each detector are measured *in situ* with a custom-built Martin-Puplett Fourier Transform Spectrometer (FTS) mounted above the cryostat window while in the telescope mount (Figure 4.1). The FTS uses a chopped liquid nitrogen source, and an automated translation stage to efficiently measure the large number of detectors across; the system is previously described in [45].

The power P received by a detector with effective area A_{eff} and source with frequency dependent $S(\nu)$ is:

$$P(\nu) = \frac{1}{2} \int_{4\pi} A_{\text{eff}}(\theta, \phi) S(\nu, \theta, \phi) \, d\Omega \tag{4.1}$$

but when the source is a blackbody in the Rayleigh-Jeans limit and fills the beam, it becomes:

$$S(\nu, \theta, \phi) = B(\nu) = \frac{2kT}{\lambda^2} \tag{4.2}$$

The effective area of a single-moded antenna is:

$$A_{\text{eff}} = \frac{\lambda^2}{4\pi} \tag{4.3}$$

and the power $P(\nu)$ becomes simply kT.

We record the detector's interferogram by moving the mirror in the FTS. The frequency response of the detector is obtained by Fourier transformed the interferogram
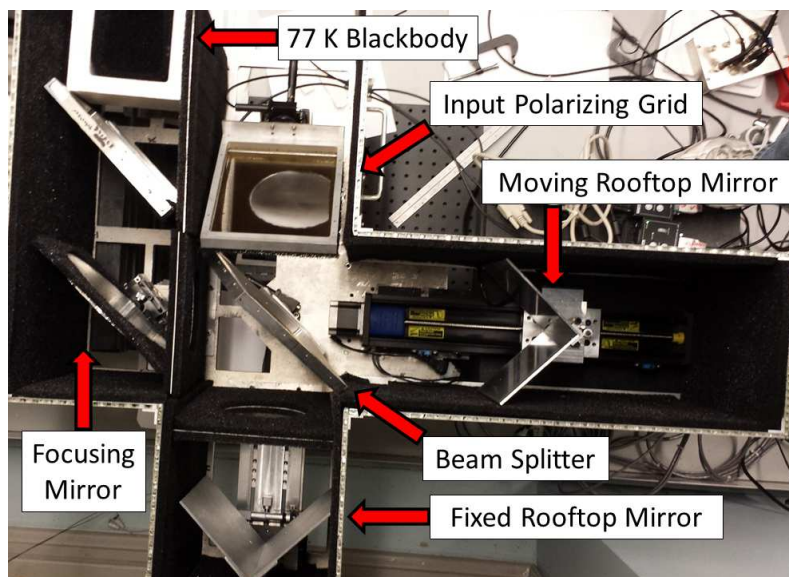
Figure 4.1: FTS setup in lab. In the time-reverse sense, the detector beam enters the FTS via the input grid, split into two polarizations, travels different path lengths, then recombined and terminates on either a room-temperature blackbody or a 77 K blackbody. Figure from [45].

after it's being low-pass filtered and aligned the path length difference. The band center of the detector is defined as

$$\langle v \rangle = \int v S(v) \, dv \tag{4.4}$$

where $S(v)$ is the frequency response, and its bandwidth, defined as

$$\Delta v = \frac{\left(\int S(v) \, dv \right)^2}{\int S^2(v) \, dv} \tag{4.5}$$

Bicep3 average band center is 96.1 ± 1.5 GHz and with average band width of 26.8±1.3 GHz, corresponding to a fractional spectral bandwidth of 27 %. Figure 4.2 shows the average frequency responds of Bicep3 with atmospheric transmission from the South Pole.

Spectral features non-uniform between modules are found in the 2016 spectra (Figure 4.3). These are ultimately understood to be generated from delamination of the low-pass edge filters mounted on top of the detector module. All edge filters are replaced before the 2017 season and no longer shown non-uniformity in the detector spectral response.
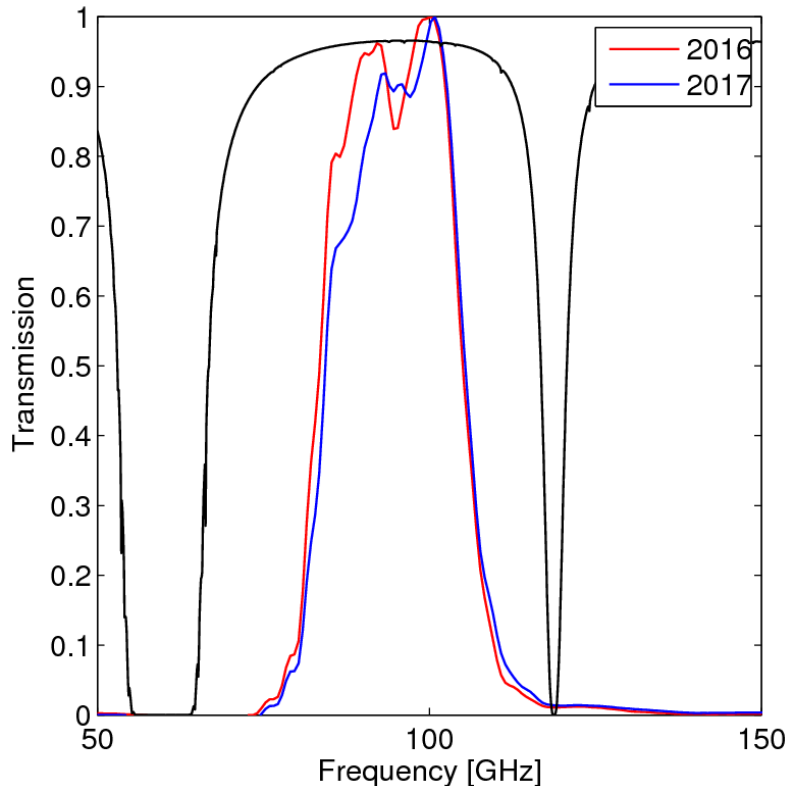
Figure 4.2: The average band pass of Bɪᴄᴇᴘ3. Red shows the spectral responds in 2016, and blue shows the responds in 2017. Black line is the atmospheric transmission at the South Pole. Five of the detector modules and all the metal mesh filters are changed between these two seasons.

Higher frequency blue leaks are also measured using a chopped liquid nitrogen source and an assortment of thick-grill filters with varying low-pass cutoffs. There is a known, measurable sensitivity to above-band radiation via direct coupling to the TES bolometer islands. Measurements showed transmission amplitudes of approximately 0.76% above 120 GHz edge, 0.61% above the 170 GHz edge, and 0.55% above the 247 GHz edge.

4.2 Optical efficiency

The optical efficiency of the receiver is the fractional amount of light absorbed by the detector compared to the total possible. The end-to-end efficiency dependent on the losses in the optics, antenna network, and the detectors.

The saturation power of a TES is shown in TES load curves, in which the TES bias current is stepped down from the normal-resistance to superconducting regime, are performed to measure the incident optical power on the detectors under a 77 K and
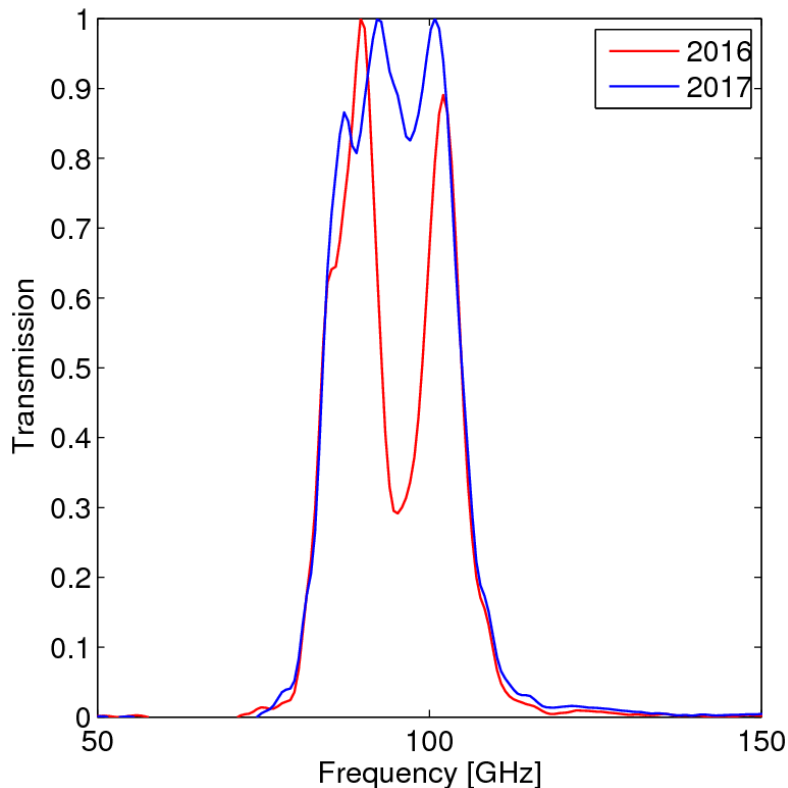
Figure 4.3: FTS measurement of tile 12 in Bɪᴄᴇᴘ3. Red line is data taken from 2016 showing the dip in-band resulted from the faulty metal-mesh edge filter. Blue line shows the 2017 measurement, with a more uniform spectrum after the replacement of the filter.

ambient temperature load. We compare the saturation power of the measurements against the computed optical loading from an aperture-filling load held a fixed temperatures to calculate the end-to-end optical efficiency. Additionally, observing the sky and a mirrored sheet provide in-band temperature estimates of the atmosphere and the internal cryostat photon load.

Figure 4.4 shows sample load curve data for different sources. Change in optical loading between ambient temperature (266 K) and 74.2 K is obtained by placing a 3×3 ft Zotefoam pool, containing an absorptive Eccosorb layer, directly over the cryostat window. The pool is first allowed to equilibrate with the outdoor air and then filled with liquid nitrogen (Figure 4.5). Similar to the spectral measurement, for an aperture-filling, the power deposited on a single-moded polarization-sensitive detector is

$$P_{opt} = \frac{\eta}{2} \int d\nu \lambda^2 S(\nu) B(\nu, T) \tag{4.6}$$
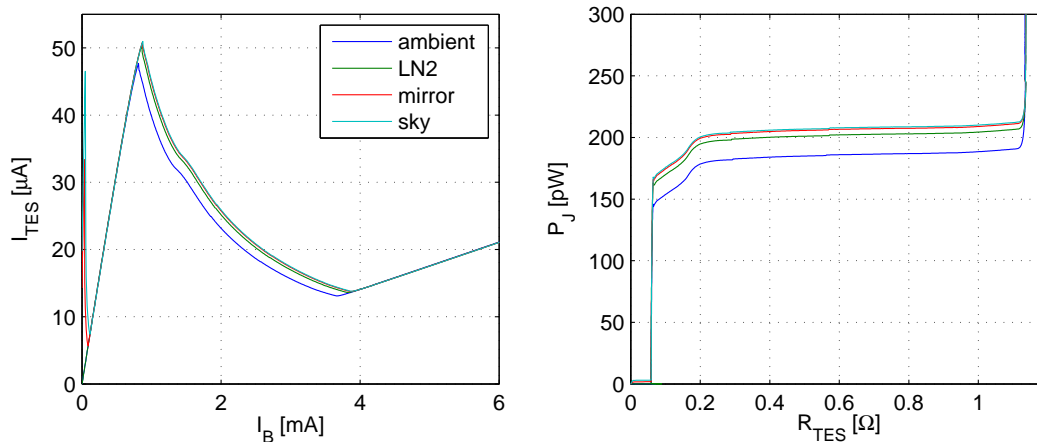
Figure 4.4: Load curves and power plot for a single TES detector going through the aluminum transition, with four different aperture-filling sources. Left: current through the TES versus TES bias current (through both the TES and shunt resistor). The titanium transition is also visible squeezed along the left border for the two colder sources. Right: same data transformed to power axes showing Joule power in the TES versus the TES resistance [46].

where v is the optical efficiency, $B(v)$ is the Planck blackbody spectrum at temperature T, and $S(v)$ is the detector response in frequency.

In the Rayleigh-Jeans limit ($hv \ll kT$) and that the integral over a diffraction limited beam, Equation 4.6 reduces to

$$P_{opt} = kT\eta \int dv S(v) = kT\eta\Delta v \tag{4.7}$$

where Δv is the fractional bandwidth and η is the optical efficiency of the system.

The measured change in loading is compared to the expected results to obtain the optical-efficiency distribution shown in Figure 4.6. The average end-to-end efficiency measurements show 0.08 pW/K and 0.11 pW/K, representing efficiency of 23% and 29% in 2016 and 2017, respectively. The improvement from 2016 to 2017 is due to replacing 4 out of the 20 detector modules in the receiver, and the change of 300 K thermal filters reduced the loading of the instrument.

4.3   Measured detector properties

All the detectors are screened prior to deployment to ensure that they have the correct parameters and yield. Similar to the procedure of optical efficiency test, we can measure the thermal conductance G_o, thermal conductance exponent n, and transition temperature T_c by taking the load curve of the detector. This measurement
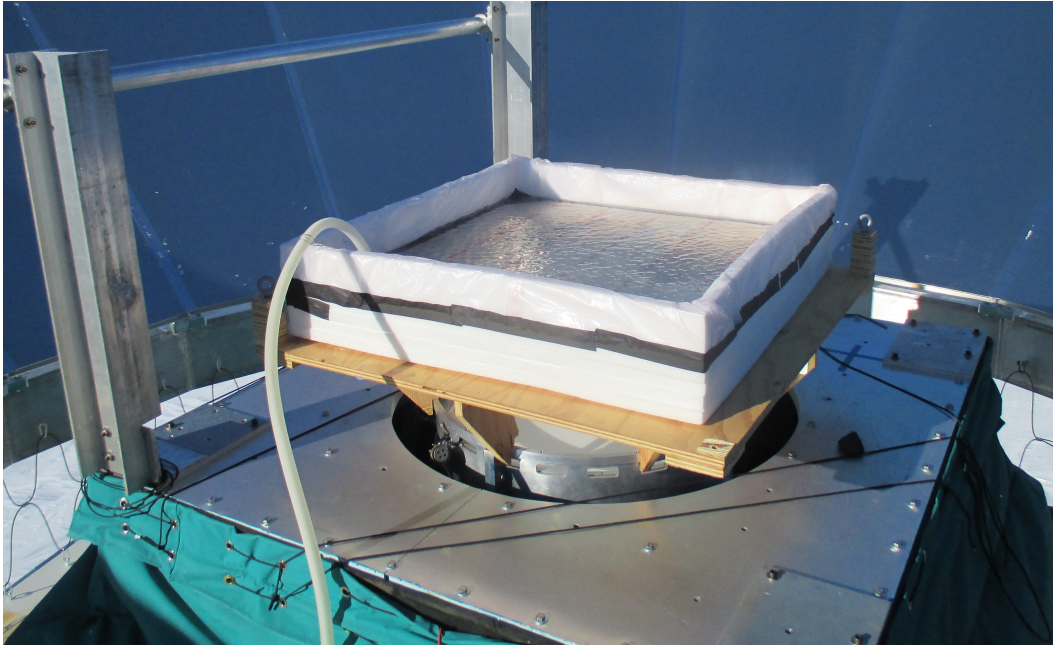
Figure 4.5:   Optical efficiency measurement setup
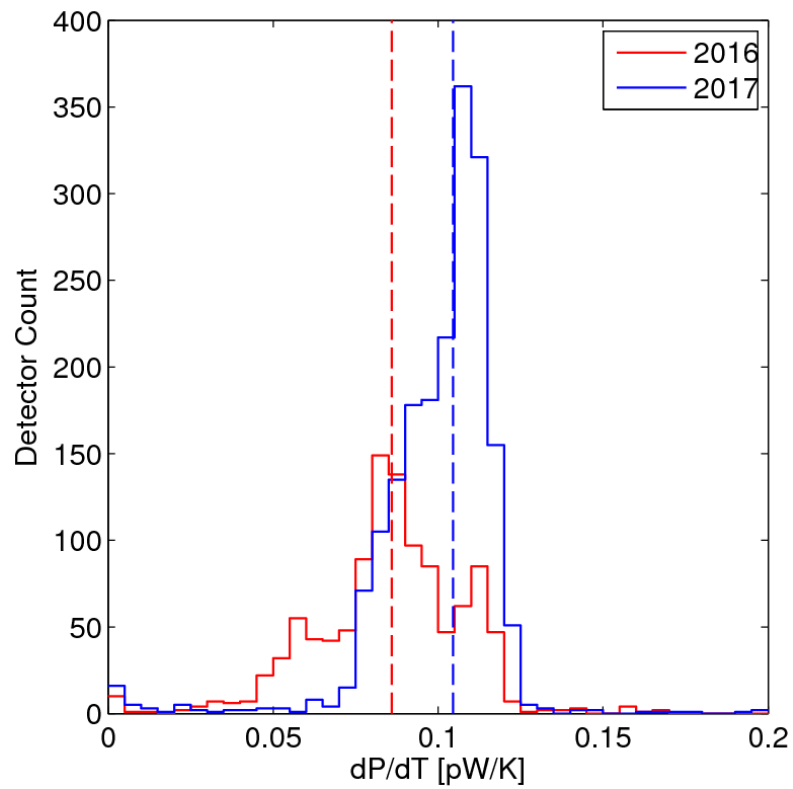
Figure 4.6:   Optical efficiency in BICEP3 in 2016 and 2017. The median efficiency is 0.085 pW/K and 0.11 pW/K, about 23% and 29% in 2016 and 2017, respectively.
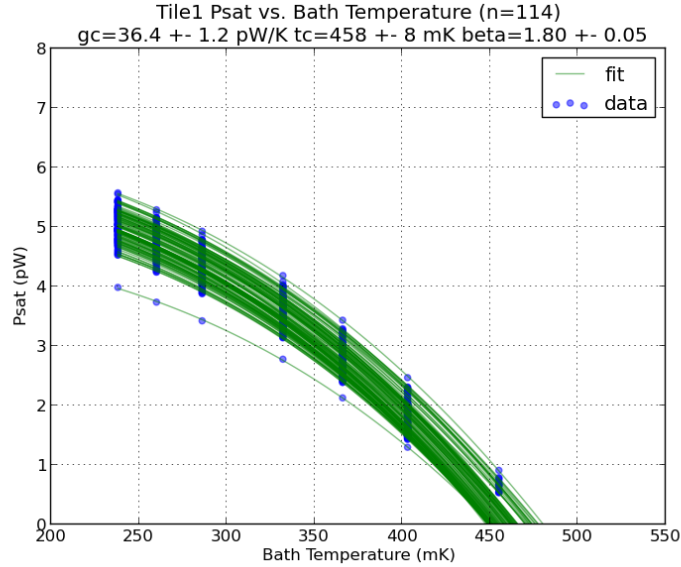
Figure 4.7: Saturation power of the detector with different bath temperature. The data can be fitted to calculate multiple detector parameters. This measurement is done in a dark cryostat, without any input optical power. Each green line represents a TES in the detector tile, the tight grouping shows good uniformly across the tile, while $n = 114$ shows this tile has 114 out of possible 120 working detectors.

is generally performed in a dark cryostat, the detector modules are covered by a microwave-blacken plate so no optical power are transmitted to the detector. In this case, the saturation power of the detector P_{sat} is

$$P_{\text{sat}} = G_o T_o \frac{(T_c/T_o)^{n+1} - 1}{n + 1} \tag{4.8}$$

By taking load curves at multiple bath temperatures T_0, and calculating the saturation power at these temperatures, we can fit these detector parameters (Figure 4.7). Table 4.1 summarizes these detector parameters.

4.4 Detector bias

The detector is designed to operated in strong electrical thermal feedback, this gives the responsivity of the detector with voltage as

$$\frac{dI}{dP} \approx \frac{dI}{dP_{\text{elec}}} = \frac{1}{V} \tag{4.9}$$

This shows the responsivity increase with lower biasing voltage. However, increase in responsivity also increases noise. The usable bias is also limited by the detector

Table 4.1: Average detector parameters in 2017 Bicep3

Detector Parameters	Value
Normal resistance, R_N	72 mΩ
Saturation power, P_{sat}	4.7 pW
Optical loading, P_{opt}	1.9 pW
Thermal conductance, G_c	32 pW/K
Transition temperature, T_c	474 mK
Thermal conductance exponent, β	1.77
Optical efficiency, η	29%

becomes unstable at low bias, and the safety margin of the detector before saturation decreases at high bias.

We calculated the sensitivity of the detectors at each possible bias set point in the beginning of the observing season to select the optimal bias. The NET is calculated using five minutes of noise data with the telescope at zenith with different detector biases. This measurement, while not giving us the absolute sensitivity of the receiver since the assumed sky temperature of $\sim$ 9 K is used, allows us to determine the best bias value for each detector.

Figure 4.8 shows the NET as a function of bias point for one module. Due to the multiplexing design, we use one bias voltage for all detectors in the same column with 22 bolometers.

4.5 SQUID multiplexing readout

Section 3.5 shows Bicep3's time-domain multiplexing design using SQUIDs. This section discusses optimizing the SQUID readout for data taking. Section 4.6 details the magnetic shielding of the instrument, which is mainly targeted for the SQUID readout.

Bicep3 uses 2-stage SQUID. Each stage of the SQUID needs to be properly bias and have flux-feedback to place the amplification in a linear part of $V - \phi$ curve. Generally, the response of the SQUID is:

$$V = \frac{R}{2}\sqrt{I^2 - (2I_c \cos(\pi\Phi/\Phi_0))^2} \qquad (4.10)$$

where $\Phi_0 = h/2e = 2.07 \times 10^{-15} Wb$ and the respond is the steepest when the flux $\phi = \Phi/\Phi_0$ at the periodic of $1/2$, and the current I is just larger than the critical
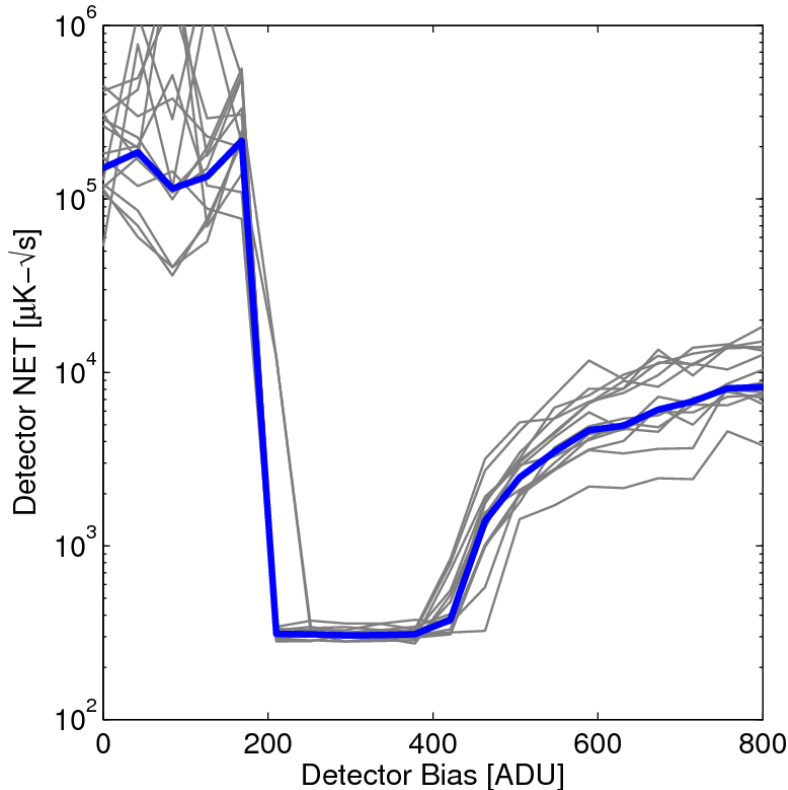
Figure 4.8: One column of detector NET as a function of TES biases, blue shows the median NET in this column. A single detector bias value is shared with all the detector in the same column. The relatively flat region at low biases show minimal TES excess noise in this tile.

current I_c. But the SQUIDs are highly non-linear, we set a feedback loop to cancel change in SQUID flux to linearize the readout. The flux and current bias point must be carefully selected to maintain high dynamic range and avoid non-linearity (Figure 4.9).

The tuning procedure of BICEP3 is to first pick an appropriate bias and flux position of the SSA, and flux by sweeping the SSA flux feedback line, and reading the output signal (Figure 4.10). This is generally not a problem since we can individually pick the bias and flux point for each SSA.

The next tuning step is SQ1, which the response is asymmetric due to self-feedback. Furthermore it mixes SQ1 and SSA curves if the SQ1 feedback are ramp on open-loop. This is fixed by sweeping the SQ1 flux feedback line and readout by servoing the SSA. All the SQ1s in a single column (22 per column) share a common bias, so the chosen bias must be a compromise across the column (Figure 4.11).
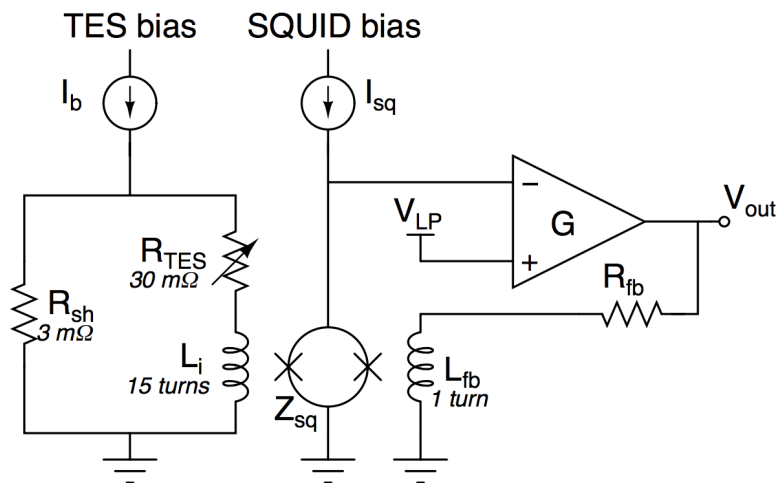
Figure 4.9: SQUID Readout diagram of a single bolometer. The left shows the biased TES bolometer. The right shows a single SQUID amplifier schematic. In reality this SQUID is chained to another stage of amplification and multiplexing system.
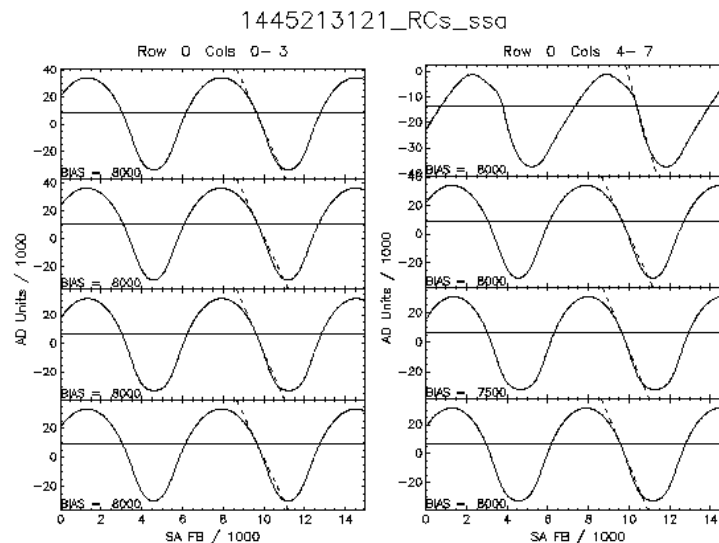
Figure 4.10: SSA $V - \phi$ curves. The voltage bias determine the peak-to-peak of the curve, while the flux lock point (horizontal line) determine the slope, or the responsively (dash line). We also want to avoid picking lock point with structure, for example Column 4 in the figure for non-linear responds.
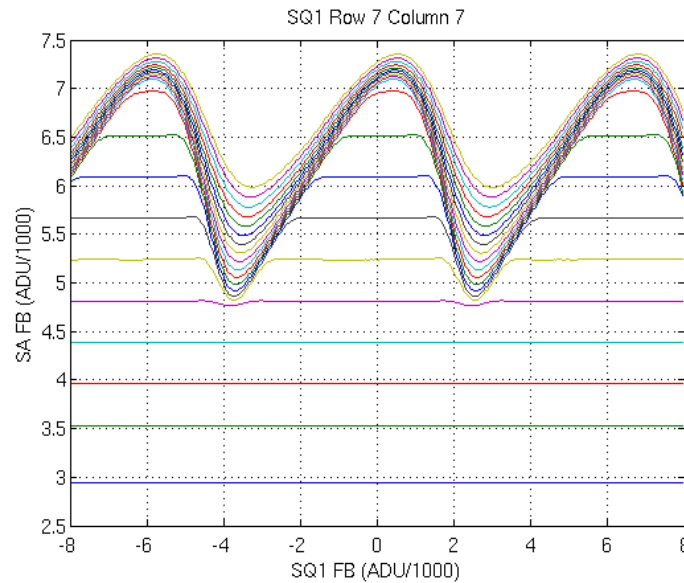
Figure 4.11: SQ1 $V - \phi$ with different biases. Each color shows a different bias, low bias decrease the peak-to-peak of the curves, while too high of a bias voltage saturates the curves (flat line).

Enabling the time-domain multiplexing in the SQUID is done with the superducting-to-normal flux-activated switches (RS switch). They share the same bias voltage as the SQ1 by wire in parallel with the SQ1, this design allows the reduction of wiring count going to the focal plane, thus reducing the heat load. However, it limits the flexibility for an optimal tuning by sharing the bias line.

At zero flux input, the RS switches are designed to remain superconducting, this shorts the bias current around the SQ1 (off stage), and high resistance compared to SQ1 at half flux quanta ϕ (on stage). The tuning for this step is to pick out the proper flux for the stages. The switches are designed to remain off as long as the resistance is much less than the SQ1 (Figure 4.12).

SQUID crosstalk

The RS switches and SQ1 are shared with the same bias, while the higher bias generally increase the dynamic range of the SQ1, too high of a bias results in the RS off-stage resistance becoming too high, creating leakage from a supposedly off detector.

As the final tuning procedure, all the RS switches in the column are set to zero flux as the 'on-stage'. With all the RS being turned off, none of the SQ1 will be sufficiently biased to produce voltages, except for the column with switches not fully
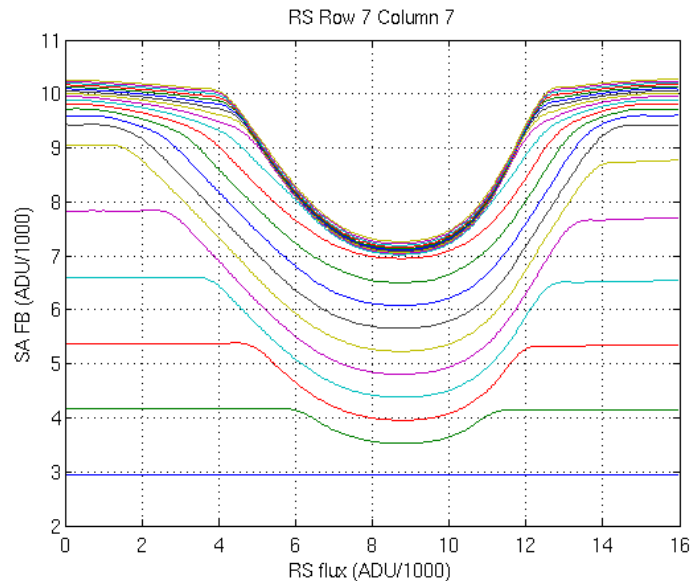
Figure 4.12: RS $V - \phi$ with different biases. Each color shows a different bias. At zero flux, the switch is at a superconducting stage, and shorted the detector readout of that channel. At maximum (around 900 ADU), the detector bias current is readout by the SQUID.

turned off. We then adjust the bias voltage of the appropriate column to try to avoid crosstalk (Figure 4.13).

Another behavior in early development stage of BICEP3 is RS switches stayed on, even without bias voltage, due to damage MUX chips during installation (Figure 4.14). This is corrected by noting the corresponding channels and manually unpluging the wirebonds from those channel (Figure 4.15). This procedure usually occurs at the South Pole, is difficult and high risk because of the insufficient equipment and potential ESD damage from the extreme dry environment.

4.6 Magnetic pickup

SQUID amplifiers are used to readout signals from the detector, they are designed to operate in a magnetically quiet environment. It is important to shield any source of external magnetic field that could potential interfere with them. The biggest external factor is the Earth's magnetic field. In theory, this signal being ground fixed, the ground subtraction step in the analysis pipeline (Section 5.1), should fully removed this component from the science data. We did extensive magnetic pickup measurement, both in lab with a Helmholtz coil, and assessing the dark SQUID response during sky observation.
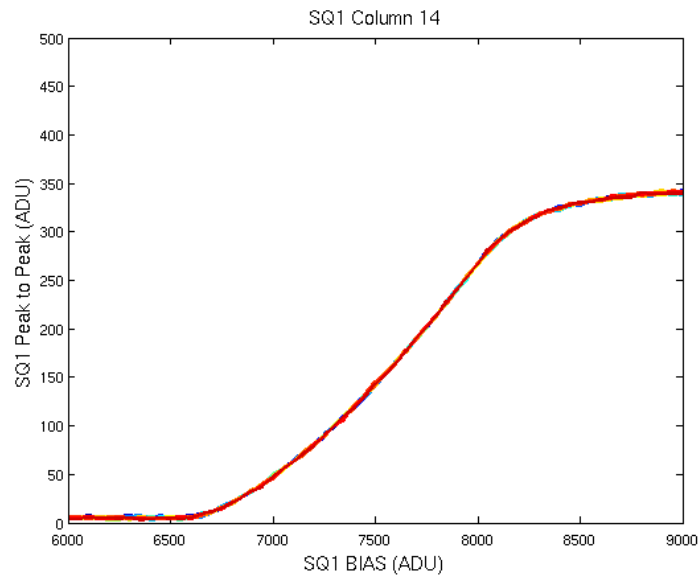
Figure 4.13: Crosstalk at different SQ1/RS bias. This shows the SQ1 responses while setting all the RS to 'off' stage at different biases. Anything above zero indicates crosstalk in the column. This figure shows the minimum voltage bias we can set for SQ1 and RS, for this column is 6500 ADU, even this might not be the optimal bias for the SQ1.
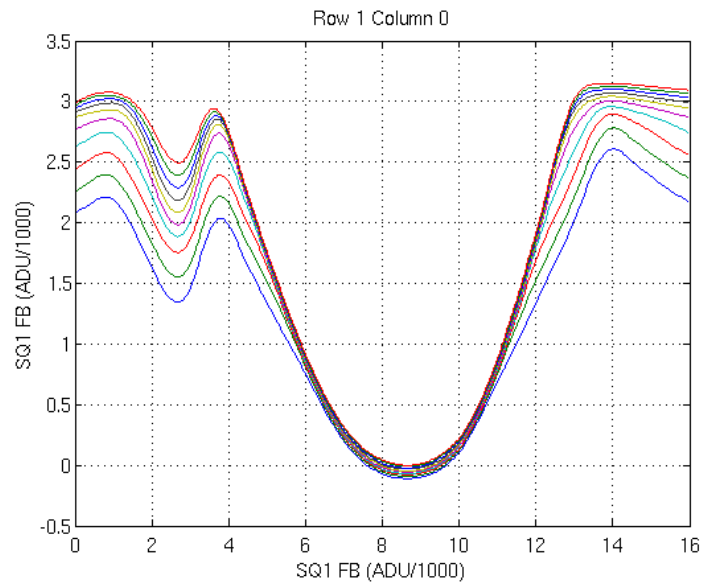
Figure 4.14: Example of damaged RS $V - \phi$ curve. This shows the channel stays on even at zero bias.
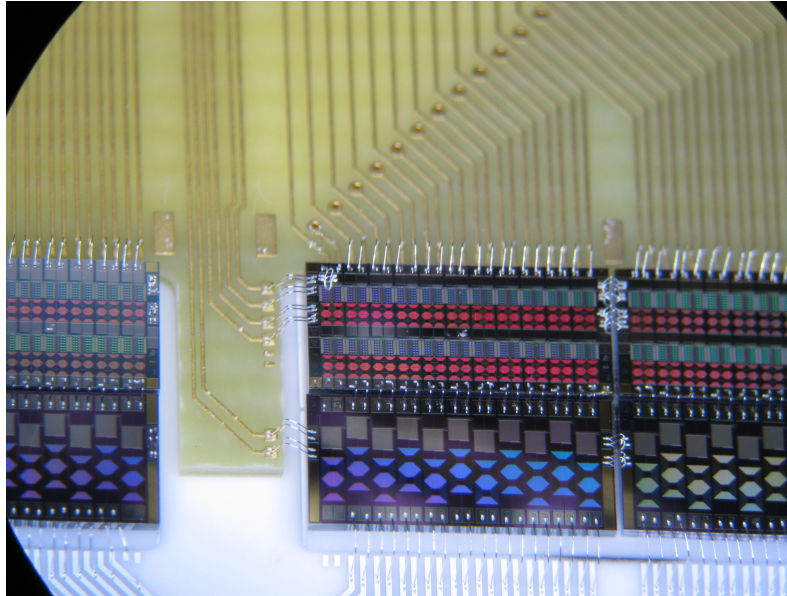
Figure 4.15: Wirebond fixes for damaged MUX. After identify the damaged MUX, we can short the channel by physically unplug the wirebonds from the devices. This photo shows the fix in row 0 at the top left corner.

There are two main shielding systems in the receiver; first, is the high permeability shield lines the inside wall of the vacuum jacket and the Cryoperm that wraps around the 4 K FPU shell (Section 3.2). The second level of shielding is done at the detector focal plane, with the module largely made out of Niobium, and interlayed with high-μ A4K sheet underneath the MUX chips (Section 3.3).

Helmholtz coil measurement

During lab testing, we measured the level of magnetic pick up by using a custom made Helmholtz coil, which produces a uniform magnetic field B:

$$B = \left(\frac{4}{5}\right)^{3/2} \frac{\mu_0 N I}{R} \tag{4.11}$$

where $N = 26$ wraps of 14 gauge wire, with the outer-diameter of the top coil is 27" and that of the bottom coil is 24". At 5 amps of current, it generates about 350 μT of magnetic field at the focal plane in the boresight direction. We measured the SQ1 responses with an modulated current through the coil. The median SQ1 response is about $1 \times 10^{-6} \phi_0/\mu$T, where ϕ_0 is the flux quanta on SQ1. In the end, the important thing is to assess the potential contamination of this pickup into the CMB data, which we can calculate using absolute calibration. At the time of testing in 2015, the calibration of BICEP3 was about 3800 μK$_{\mathrm{cmb}}$/fpu, where fpu is the SQ1
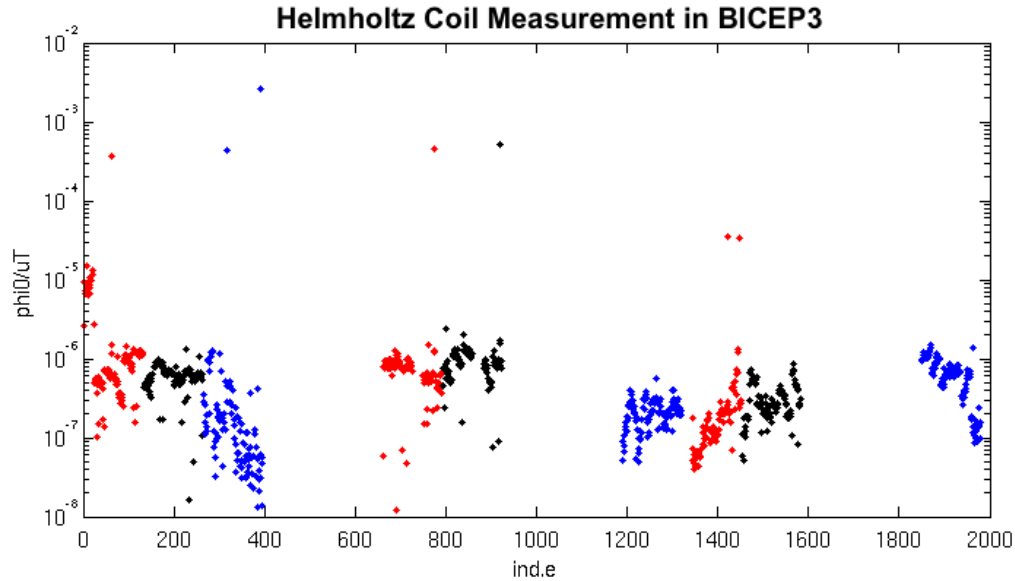
Figure 4.16: Helmholtz coil measurement in 2015. Each color representing a MCE readout unit in the receiver. Only 3 MCE, and 9 detector tiles are installed in this run.

feedback units. With this, we estimate the median pickup of $\sim 6.8\ \mu K_{cmb}/\mu T$, or $350\ \mu K_{cmb}/B_{Earth}$. This is similar to the level of pickup in BICEP2, which has shown sub-dominant in systematic.

Dark SQUIDs response during scan

We also estimate the magnetic pickup by analyzing dark SQUID channels in the receiver. These SQUID channels are located at the same MUX chips as other detector readout SQUIDs, but are not connected to any TES bolometers. The only signal these dark SQUID channels pick up would be either from crosstalk from other detectors through multiplexing, or magnetic pickup during scans.

The average dark SQUID response shows a slope of ~5 mK across a single 60 degree azimuth scan.

Figure 4.17 shows the raw magnetic shielding performance of the BICEP3 cryostat while scanning. But the final CMB maps are heavily filtered, ground template subtracted, and coadded with different deck angles. These steps would further suppress the pickup. Here we estimate the amplitude of the pickup after these analysis procedure.

The noise level in an CMB polarization map is about 0.1 μK-deg. Figure 4.18 shows
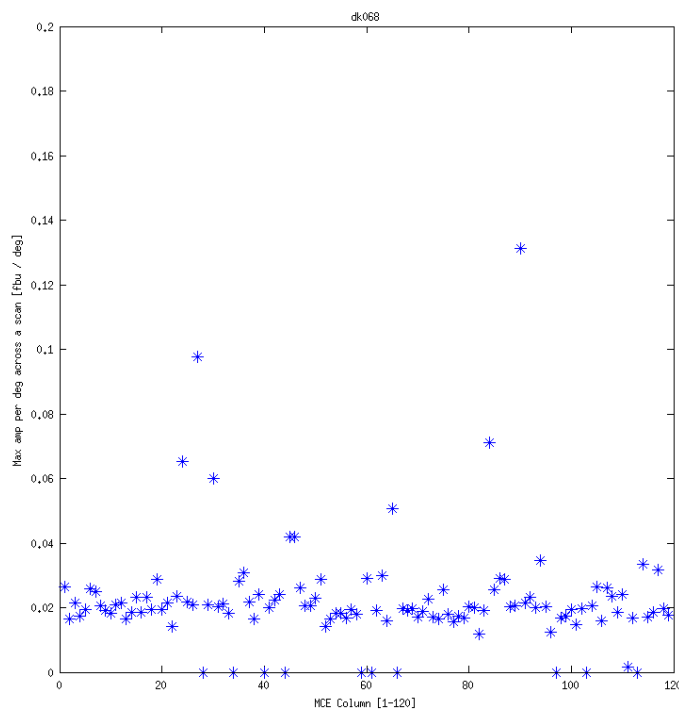
Figure 4.17: Dark SQUID responses during scan. Each point in the plot represents a 60 degree scan on azimuth, with an average of ∼ 0.02 fpu/deg. The calibration is ∼ 4200 μK$_{cmb}$/fpu, which gives an estimate of ∼ 5 mK across a 60 degree scan.

the dark SQUID map, substituted with pixel with the dark SQUID response in the corresponding readout column, with the noise about 0.03 μK-deg, factor of 3 lower than the polarization map noise.

While the noise rms is sub-dominated compared to observation noise, it is also crucial to make sure the noise is not concentrated in the science band at $l \sim 100$. Figure 4.19 shows the angular power spectra of the dark SQUID map comparing noise of the polarization, which shows the noise is also sub-dominated.

4.7 Detector linearity

The detector in BICEP3 contains two TES in series, the titanium is used for sky observation while the higher T_c aluminum is used in beam maps and optical efficiency calibration to avoid saturation. It is important that the current response during Al transition is linear of the input power to ensure the accuracy of the calibration measurements.
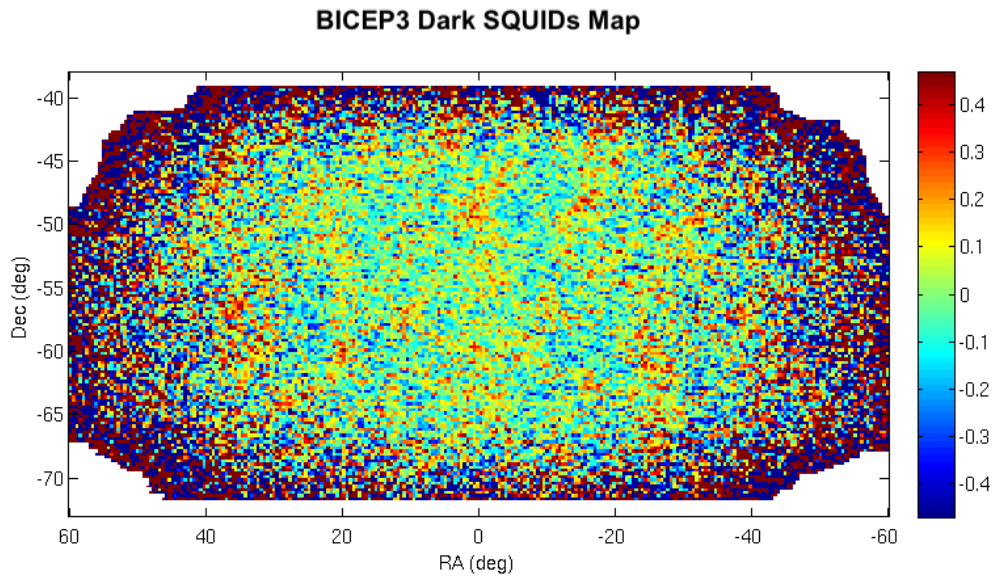
Figure 4.18: Dark SQUID map
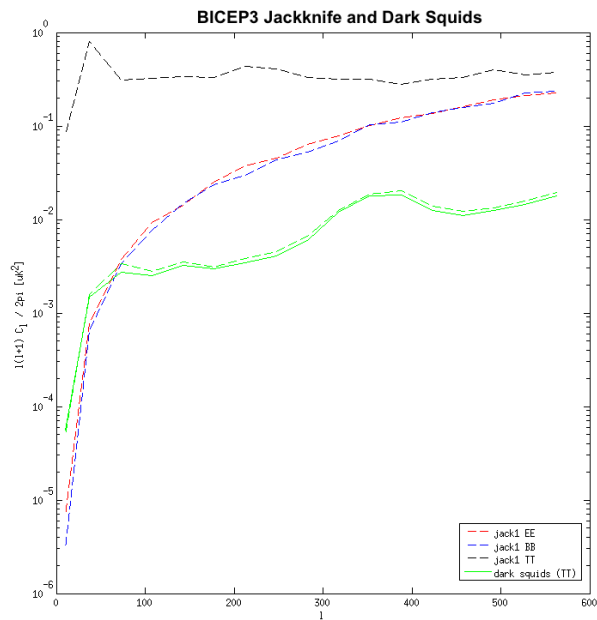
Figure 4.19: Dark SQUID angular power spectra. The black, red and blue lines show the amplitude from temperature and E/B scan direction jackknife map, representing the noise of the corresponding map, green lines show two different set of measurement of the dark SQUID channel. Signal at $l < 100$ in polarization and dark SQUID channel are suppressed by polynomial filter.
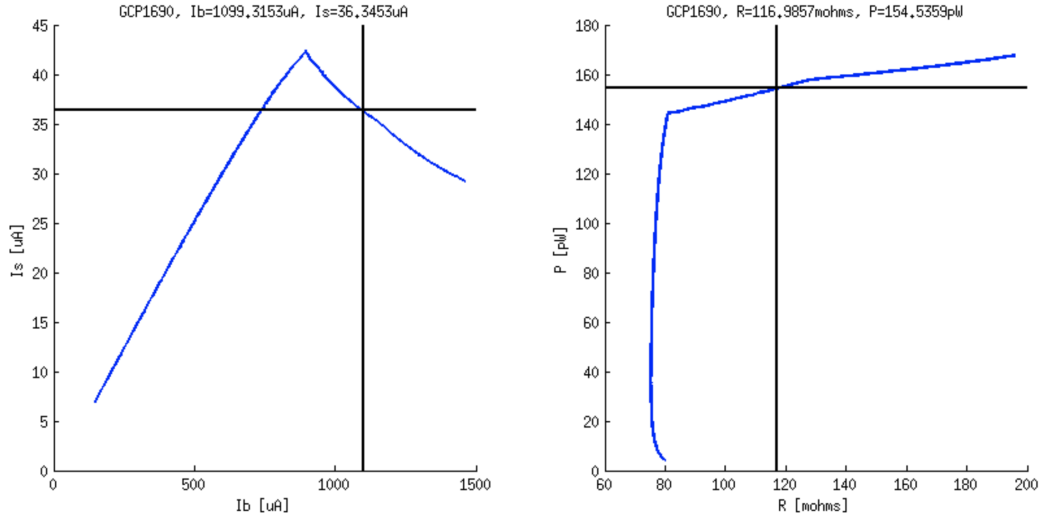
Figure 4.20: Left: Aluminum TES load curve. Right: The power verse resistance response. The cross mark the bias current I_{b0} chosen during calibration.

Figure 4.20 shows the detector aluminum load curve and the power verse resistance response, it also shows the bias current I_{b0} chosen for during measurement. We can convert the power P into temperature T (Figure 4.21):

$$P + P_{\text{opt}} = P_b = \frac{G}{(1+n)T^n}\left(T^{1+n} - T_b^{1+n}\right) \tag{4.12}$$

where P_b is the power flow from the TES to bath, or P_{legs}. We can rearrange this to:

$$T = T_0 \left[\frac{(P + P_{\text{opt}})(1+n)}{G_0 T_0} + \left(\frac{T_b}{T_0}\right)^{1+n} \right]^{\frac{1}{1+n}} \tag{4.13}$$

We used the bias point I_{b0} and its resistance R_0. For each T and $R(T)$, we can find the change in optical power necessary to reach thermal equilibrium:

$$P_{\text{legs}}(T) = P_{\text{joule}} + dP_{\text{opt}}$$

$$dP_{\text{opt}} = P_{\text{legs}} - P_{\text{joule}}(R(T), I_{b0}) \tag{4.14}$$

where

$$P_{\text{legs}} = \frac{G_0 T_0}{1+n} \left[\left(\frac{T}{T_0}\right)^{1+n} - \left(\frac{T_b}{T_0}\right)^{1+n} \right] \tag{4.15}$$
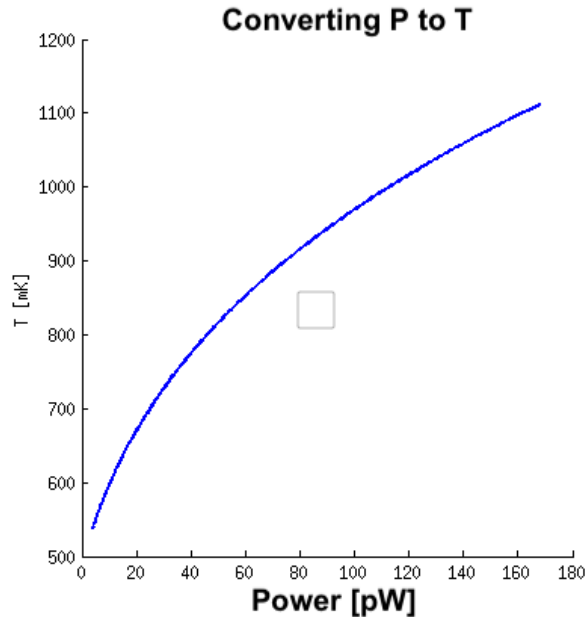
Figure 4.21: Converting power response to temperature. Equation 4.13.

and

$$P_{\text{joule}} = R \left(\frac{I_{b0}}{R/R_{\text{sh}} + 1} \right)^2 + T_{\text{loadcurve}} \left(\frac{dP}{dT} \right) \qquad (4.16)$$

We can compare the power response given a small optical power change, at the lock bias point of the detector. Figure 4.22 shows the expected change in device joule power with changing optical power, measured from the quiescent bias point, and figure 4.23 shows the deviation of the response from a fitted small-signal linear response, and shows the linearity is with in around 2%. This analysis is repeated with other detectors in BICEP3 and shows similar response.

4.8 BICEP3 sensitivity and noise performance

Time stream based NET

The sensitivity of an instrument can be define as the Noise Equivalent Temperature (NET), or as mapping speed (NET^{-2}). We measure the sensitivity of the detectors in several ways, during normal science observation, the data timestreams are multiplexed, filtered and downsample to 31 Hz (Section 3.5). The degree scale CMB mode features is range from $l \sim 30 - 300$, combining with the scan speed of ~ 1.6 deg/s in azimuth, the science frequencies band of BICEP3 is between 0.1 to 1 Hz in recorded timestreams.
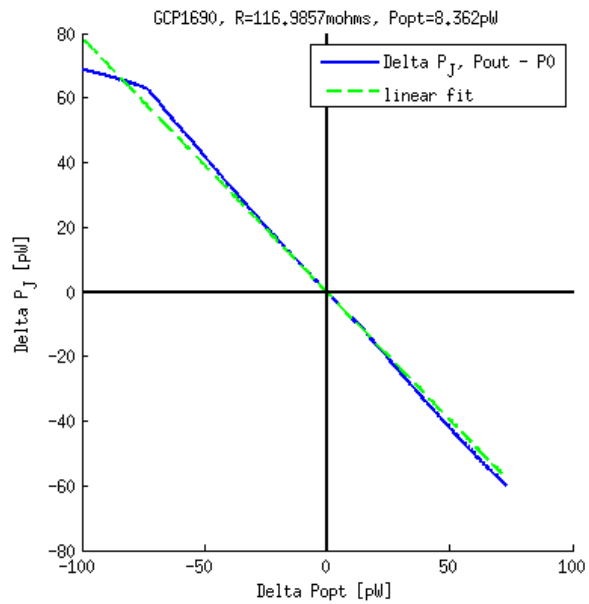
Figure 4.22: Current response with change in optical power.
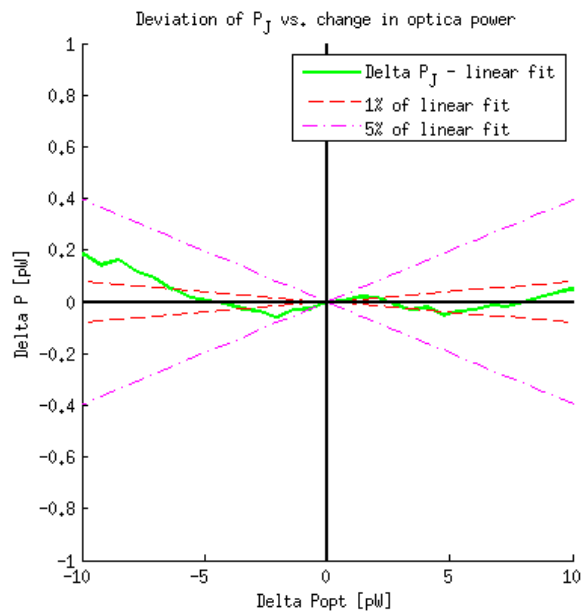
Figure 4.23: Deviation of I_s with change in optical power. Dotted lines show the 1% and 5% fit, which shows the deviation, or the linearity, is about 2% for this detector.
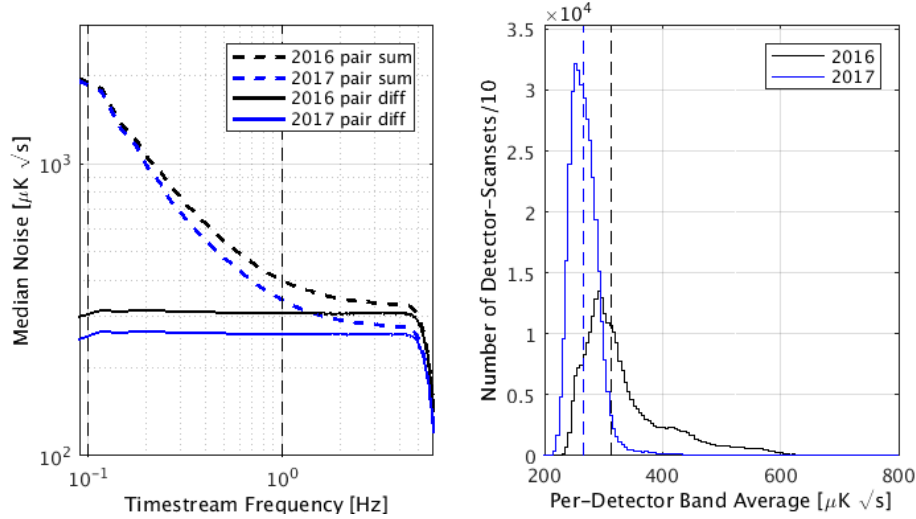
Figure 4.24: Left: Median per-detector noise spectra for Bɪᴄᴇᴘ3 2016 and 2017 season data, from both pair-summed and pair-differenced timestreams, showing $1/f$ noise rejection of the differenced polarization measurement. Right: Histrogram of the per-detector per-scanset noise, with minimal data filtering, and averaged across the 0.1-1 Hz science band. This plot is uniformly sample 10% of the scansets from both years.

Bɪᴄᴇᴘ3 is focusing on measuring the polarization signature of the CMB, which is achieved by taking the pair differenced of the co-located polarization sensitive detectors. This reduces the $1/f$ noise induced from the atmosphere, and other contaminations are further reduced by polynomial filter and ground template subtraction (Section 5.1).

Figure 4.24 shows the median noise spectrum and per-detector, per-scanset noise distribution, based on the timestreams for all CMB data in 2016 and 2017 season. Pair-summed spectra are shown to demonstrate the $1/f$ noise rejection of the pair-difference polarization data. Conversion to CMB temperature is done by calibration of the Bɪᴄᴇᴘ3 CMB temperature map to *Planck* data (Section 5.2). The histogram shows science-band average noise after basic processing of the data.

The median per-detector sensitivity is 312 $\mu K_{cmb} \sqrt{s}$, and 265 $\mu K_{cmb} \sqrt{s}$ for the 2016 and 2017 season, respectively. *Keck Array*, with similar detector and receiver design, has an average per-detector sensitivity at 288 $\mu K_{cmb} \sqrt{s}$.

The biggest reason of the sensitivity improvement between the 2016 and 2017 is because of the reduction of internal loading, caused by switching the 300 K filters (Section 3.1). Replacing delaminated edge filters above the focal plane module
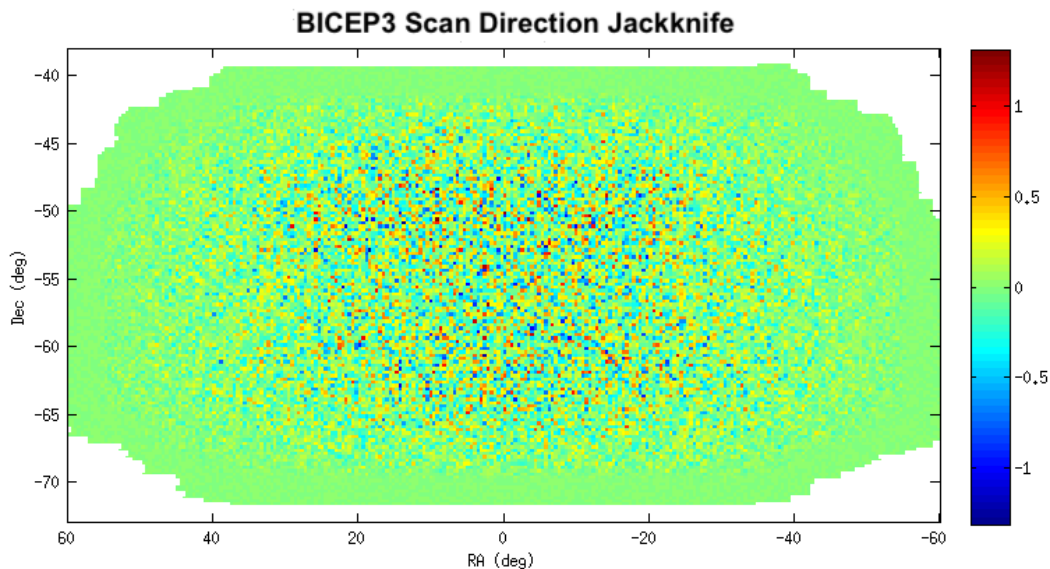
Figure 4.25: Scan diection jackknife Q map from 2016 BICEP3. The jackknife map removed any signals but retained the noise, the variance of the map gives an estimate of the sensitivity of the instrument.

improved the uniformity of detector NET.

Map based NET

Another method to estimate the sensitivity of the instrument is by evaluating the noise within the map. We use the scan direction jackknife map (Section 5.6), which are created by difference the polarized maps made with data taken in the opposite azimuth scan directions. The resulting maps contain instrument noise, but all the signals are removed.

Figure 4.25 shows the jackknife map used to calculate the sensitivity, it shows the BICEP3 instrument NET is 9.1 $\mu K_{cmb}\sqrt{s}$ and 7.3 $\mu K_{cmb}\sqrt{s}$ for 2016 and 2017, respectively. The overall improvement comes from increasing detector yield by $\sim 20\%$, and by fixing some of the cryogenic wiring problem in 2017. Five of the worst performed detector modules are also replaced to improve overall performance of the telescope.

The per-detector NET can be estimated base on the CMB maps, by multiplied the noise in the jackknife Q/U maps with the square root of the integration time map [47]. In the apodizted maps, the weighting of each pixel is the inverse variance of the time stream (Section 5.2). Figure 4.26 shows the histogram of the scan direction jackknife map, times the square root of the total integration time, which is the total
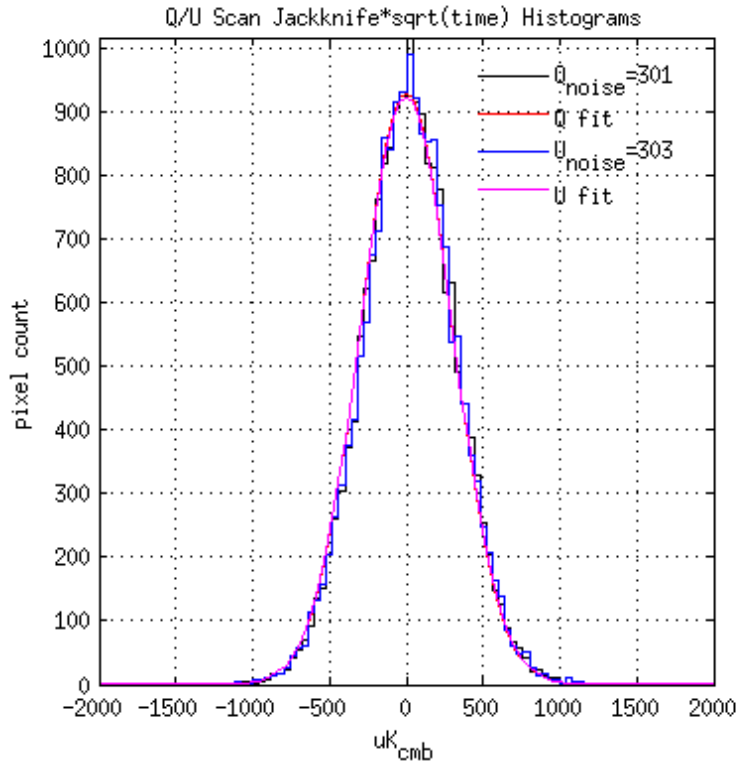
Figure 4.26: Histogram

detector time on each pixel for the entire array, making a good estimate of the per-detector NET.

Table 4.2 summarized the map based NET estimate for BICEP3. The NET calculated with this method is better than using the time-stream method because the low frequency noise has less weight. The number of effective (n_{eff}) is the total integration time, divided by the time on source, which is a way for us to include many of the data quality cut (weather, readout etc), and proper weighting of each detector (noisier detectors are weighted less in the map) into the estimate of array sensitivity. This is different than overall detector yield, which only determines the number of working detector.

Map depth

The map depth gives the final sensitivity of an experiment. It accounts for the mapping speed of the instrument, mapping area, and the observing efficiency. The coverage of the map in BICEP3 is not uniform, Figure 4.27 shows the integration time in each pixel for the 2016 season. Due to the large instantaneous field of view

Table 4.2: BICEP3 sensitivity in 2016/ 2017 using scan-direction jackknife Q/U maps

	2016	2017
Per-detector NET ($\mu K_{cmb}\sqrt{s}$)	302.5	275.2
Receiver NET ($\mu K_{cmb}\sqrt{s}$)	9.11	7.28
Effective pixel	550.9	712.3
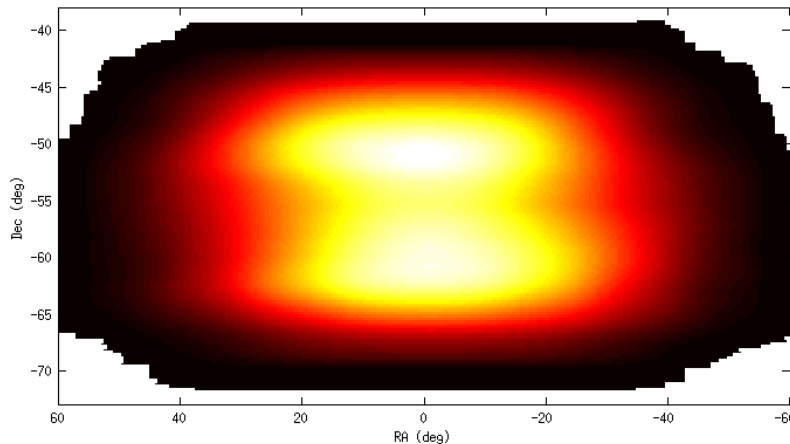
Figure 4.27: Integration time in 2016. The effective area is calculated using the same apodization mask that is used in the power spectrum analysis, which is constructed from the maps of variance in Q and U.

of the instrument, the central region is much deeper than near the edges. Following the same definition used in the BICEP2, we define map depth D in the deepest part of the map in the middle, and calculate an effective area A_{eff} that accounts for the higher variance and lower weight in other parts of the map.

Table 4.3 shows the map depth, effective area and total sensitivity of BICEP3 in 2016. Because of the bigger field of view, the total sensitivity of BICEP3 in 2016 alone already surpassed 2 season (4-receiver year total) of *Keck Array*.

High frequency noise modeling

Although the frequency region for the science band is $\sim 0.1 - 1$ Hz, it is important to understand the noise performance at high frequency to avoid aliased noise above the Nyquist frequency of the multiplexing rate. The BICEP3 detectors were characterized in a special data taking mode at 400 kHz by turning off the multiplexing step in our SQUIDs readout electronic. We took high frequency noise spectra from

Table 4.3: Map depth and effective area of Bicep3, with comparison of *Keck Array* 95 GHz. First season of Bicep3 has better total sensitivity than 2 season of *Keck Array* in 95 GHz.

	Keck Array	Bicep3 2016	Bicep3 2017
Map depth (nK-deg)	87	99	81
Effective Area (deg)	387	599	658
Total sensitivity (nK)	3.1	2.9	2.2
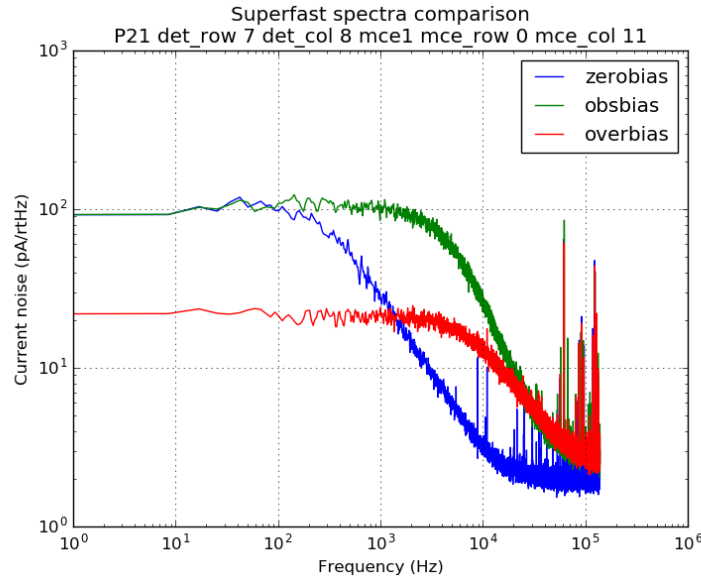
Figure 4.28: High frequency noise spectra for a single detector at different detector bias.

every detector deployed in 2016, at different bias region, to characterize their noise performance (Figure 4.28).

Furthermore, by taking noise spectra at different data rate, we can study the aliasing noise to the science band from high frequency noise (Figure 4.29).

The noise model of these detectors were well studied back in Bicep2 and *Keck Array*[48] which have the same design as in Bicep3. Figure 4.30 shows noise spectra with different noise components model. We show that the detector is indeed dominant by photon noise at low frequencies. The noise-equivalent power is:

$$\text{NEP}^2_{\text{photon}} = 2h\nu Q_{\text{load}} + \frac{2Q_{\text{load}}}{\nu \frac{\Delta \nu}{\nu}} \tag{4.17}$$

where ν is the frequency, $\frac{\Delta \nu}{\nu}$ is the fractional bandwidth, and Q_{load} is the combination
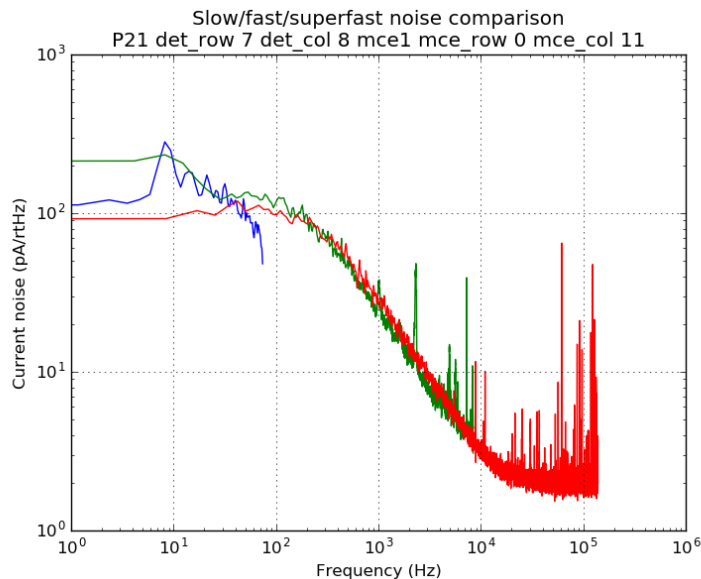
Figure 4.29: High frequency noise spectra for a single detector at different detector bias.

of the loading from the sky and internal loading from the receiver. Table 3.3 shows the noise largely comes from the atmosphere due to the low-loading design in BICEP3.

The next biggest contribution is the thermal fluctuations noise from the SiN legs of the detectors, which is proportional to the square root of the thermal conductance

$$\text{NEP}^2_{\text{phonon}} = 4kT_c^2 G_c F(T_c, T_{bath}) \tag{4.18}$$

where $F(T_c, T_{bath})$ accounts for non-linear thermal conductance and its estimate to be ~ 0.5. The thermal conductance G_c of the detector is designed to minimize noise while have enough safety margin to avoid saturation.

The Johnson noise is suppressed by the TES thermal feedback loop gain, and the SQUIDs amplifier noise has a broad spectrum white noise that is subdominant in the low frequency region.

4.9 Detector Yield

Different than the effective pixel definition described in Section 4.8, the detector yield shown in this section is the number of possible detector pair, which are the pixel that have working detectors on both polarization, regardless their noise performance. This gives an estimation on wiring yield inside the cryostat, and
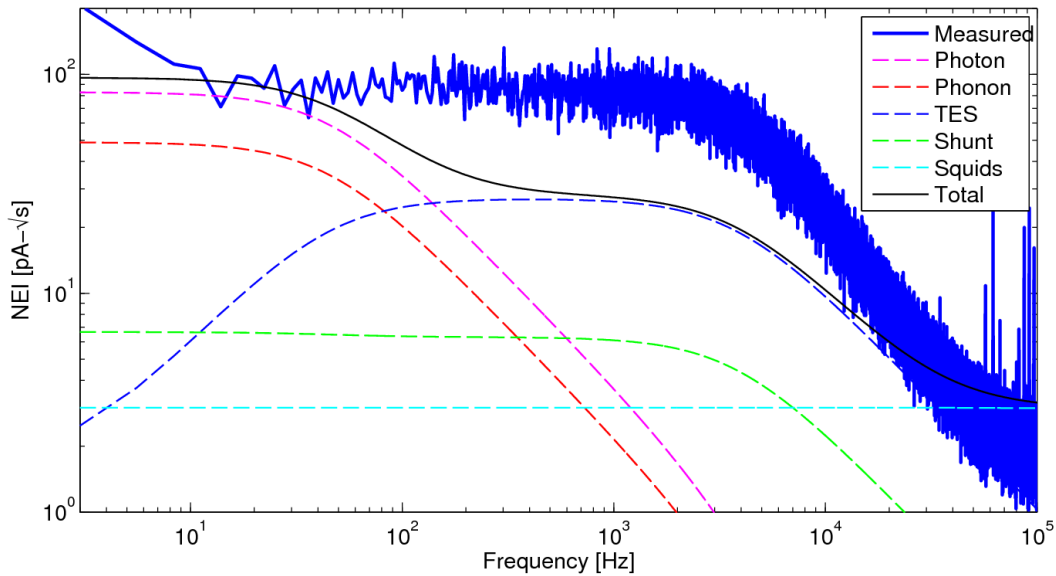
Figure 4.30: Measured and modeled noise for a individual light detectors in BICEP3. The $1/f$ knee at 8 Hz in the measured spectra is from atmospheric fluctuations, which get suppressed by an order of magnitude down to 0.1 Hz after pair-difference polarization pairs.

SQUIDs performance of the receiver, while the effective pixel (n_{eff}) includes the noise of individual detector, and overall observation efficiency.

Table 4.4 shows the detector yield of BICEP3. We achieved 64% and 71% yield in 2016 and 2017, respectively. Most of the missing detectors in 2016 are due to wirebonding failure at cryogenic temperature in MCE3. These wirebonds, connected between the MUX chips and the readout circuit board, disabled the entire MCE readout row if any of them were open. Since the detectors within the same polarization are wired in the same column (different row), each failure row also disabled the neighboring row, which furthermore decreased the overall yield. Each disabled row corresponded to 30 pixels in the focal plane.

This problem is fixed in the 2017 season, by examining and replacing the wirebonds at the South Pole.

4.10 Beam mapping

BICEP3 measures the CMB polarization by differencing the co-located, orthogonally polarized detector pairs in the focal plane. Mismatch in the beam shape between the two polarization detectors would leak the bright temperature signal into polarization, causing false B-mode signal [35].

Table 4.4: Bicep3 detector yield. Each tile has maximum 60 working pixel

2016	Yield	2017	Yield
P02	50	P25	56
P04	47	P04	47
P14	36	P26	51
P13	54	P13	54
P20	53	P20	52
P22	34	P22	34
P21	47	P21	44
P18	41	P18	43
P11	50	P24	52
P10	49	P10	49
P17	36	P17	46
P12	46	P12	42
P16	41	P27	47
P07	39	P07	40
P23	43	P23	42
P03	19	P16	32
P06	19	P06	32
P19	23	P19	38
P08	18	P08	37
P09	18	P09	18
	Total		Total
	763/1200		856/1200

We use 'deprojection' during analysis to minimize the temperature-to-polarization leakage. At the same time, we also developed techniques to characterize the beam profile in Bicep3. Full description of the measurements and results are listed in [49].

Far-field measurement setup

The optical far field of a telescope is $2D^2/\lambda$, where D is the aperture size and λ is the wavelength. One of the benefits of a small aperture telescope like Bicep3 which $D = 520$ mm and $\lambda = 3$ mm, is that the far field distance is at 180 m. This allows us to characterize the beam profile using sources on the ground.

Figure 4.31 shows the setup of the far-field measurement. We use a chopped thermal source for the measurement. The source is enclosed in a box with a rotating blade.
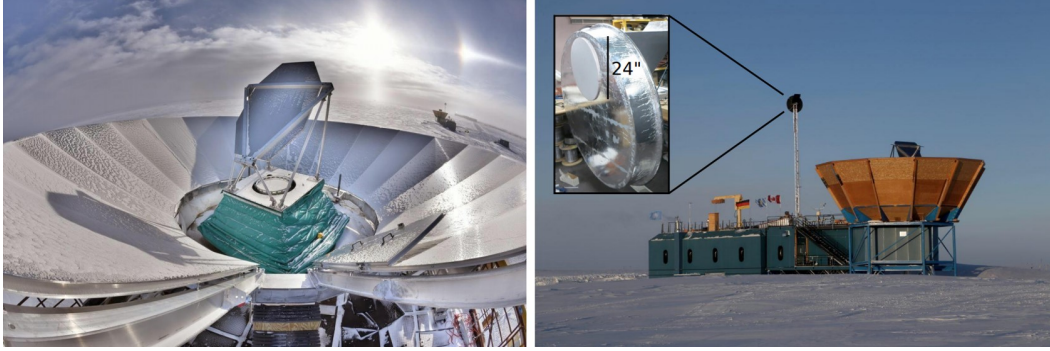
Figure 4.31: Far-field beam measurement setup. A flat aluminum mirror is installed on top of BICEP3 during the beam mapping campaign. The course is located 200 m away at MAPO, on a mask next to *Keck Array*.

Both the box and the blade are made with light weighted composite carbon fiber material. The source aperture is 24" in diameter, sealed with HD-30 Zotefoam. Behind the chopper is a flat mirror directed to zenith, so it is chopping between the cold sky at 10 K and ambient at 260 K. The large aperture and chopping rate at 14 to 18 Hz provides high signal to noise far field beam map.

Gaussian beam fit

Each beam is fit to a 2-D elliptical Gaussian model with six free parameters [50]:

$$B(x) = \frac{1}{\Omega} e^{-\frac{1}{2}(x-\mu)^T \Sigma^{-1}(x-\mu)} \tag{4.19}$$

where x is the location of the beam center with respects to the origin μ, Ω is the normalization and Σ is the covariance matrix:

$$\Sigma = \begin{pmatrix} \sigma^2(1+p) & c\sigma^2 \\ c\sigma^2 & \sigma^2(1-p) \end{pmatrix} \tag{4.20}$$

that σ is the beamwidth and p and c are the ellipticities in the plus and cross directions.

Figure 4.32 shows the far-field measurement of BICEP3 in 2016. This test is done with detector biased at Aluminum transition due to the higher loading of the source, thus have a lower yield compare to the science observation.

More than 70 partial beam maps are made in 2016, with multiple deck angle rotation to check for systematic. Results of the measurement are shown in Table 4.5. The
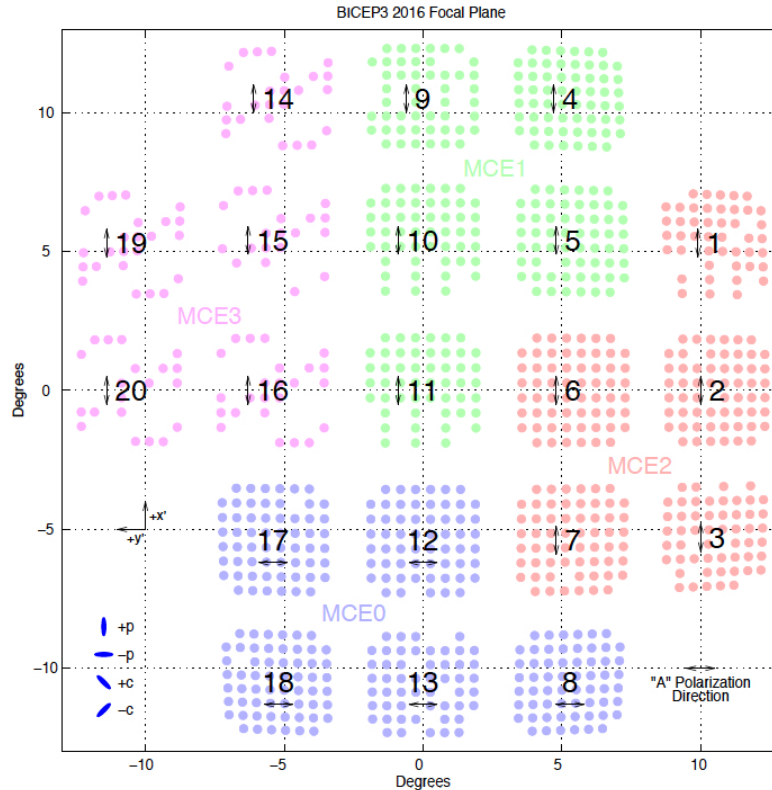
Figure 4.32: Far-field beam measurement yield in 2016 BICEP3. Tile number are labeled in black, *A* polarization detectors are indicated with arrows on each tile. MCE readout systems are separated by color. Low yield in MCE3 is due to wirebonding failure at cryogenic temperature, causing electrical opens. The legend in the bottom left shows the direction of the *p* and *c* ellipticity.

absolute beam center (x, y) are not measured, but rather the pointing is done by correlating with *Planck* temperature map (Section 5.2). Figure from Kirit Karkare.

Beam window function

We coadded the beam maps to form high signal-to-noise composite map, from which we can get the average BICEP3 beam (Figure 4.33). This beam is averaged in radial bins and Fourier transformed to obtain the circularly symmetric beam window function B_l. This beam window functions are then used to smooth various *Planck* and simulated maps in our analysis pipeline (Section 5).

Polynomial fit B_l correction

One of the uses for the beam window function B_l is to smooth the *Planck* temperature maps to absolute calibrate our observation (Section 5.2). In this analysis we found

Table 4.5: Bicep3 2016 beam parameter summary

Parameter	FPU Median	FPU Scatter	Measurement Uncertainty
Beamwidth σ (degrees)	0.167	0.002	0.002
Ellipticity plus $p(+)$	0.010	0.021	0.026
Ellipticity cross $c(\times)$	-0.004	0.016	0.026
Diff. X pointing dx (arcmin)	0.03	0.13	0.05
Diff. Y pointing dy (arcmin)	-0.12	0.17	0.05
Diff. Beamwidth $d\sigma$ (degrees)	-0.001	0.001	0.001
Diff. Ellipticity plus $dp(+)$	-0.006	0.017	0.004
Diff. Ellipticity plus $dp(+)$	-0.006	0.017	0.004
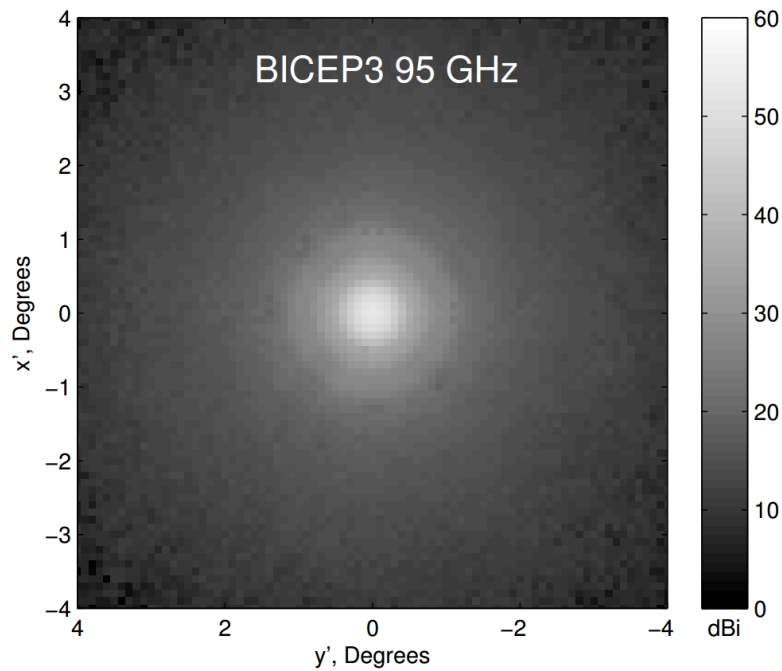
Figure 4.33: The Bicep3 average beam, made by coadding composite beam maps from all optically-active detectors.

negative slope in l range for BICEP3. We believe that this is because the beam profile used to smooth the input Planck maps does not match our real beam. While the underlying issue for this mismatch is still unclear, we developed a polynomial fit modification to correct our beam profile at high l range.

Chapter 5

DATA REDUCTION AND ANALYSIS PIPELINE

This chapter reviews the data analysis pipeline used in Bicep3, and some early 2016 season results. The same procedure are used in previous Bicep2 and *Keck Array*, but modification are made to accommodate the bigger sky faction, finer beams and different sets of systematic. For a detail description of the pipeline, see [51][52][53][54]. Observation terminologies used in this chapter can be found in Section 2.4.

The goal of the Bicep experiment is to measure the tensor-to-scalar ratio r from the degree scale polarization of the CMB. Overall, this pipeline describes how to process the time stream (TOD) data collected over detectors in Bicep3, transforming it to the polarization maps of the sky, and to angular power spectra which allow us to measure the tensor-to-scalar ratio r or its upper limit.

Most of the data processing are done in matlab, to implement a `MASTER` (Monte Carlo Apodized Spherical Transform Estimator) analysis [55]. The analysis pipeline can be divided up into these main steps: Timestreams data (TOD) are cut and filtered in low-level reduction. Construction of pairmaps from TOD and combination of them to form full season $[T, Q, U]$ maps through inverse variance weighting. Correlation with *Planck* temperature maps to calibrate detectors pointing and absolute calibration.

The simulation pipeline follows the same procedure as before, except the TOD are created through a simulated map by using the `MASTER` style algorithm to related the measured power spectra to full sky C_l. Then the simulated data go through the same filtering and map construction as the real, observed data. Noise simulations are also created with the full data set, they provide an estimation for the contribution of noise in the power spectra of the real data.

Finally, the angular power spectrum is calculated from combination of the real and simulated maps. Figure 5.1 shows a simplified analysis flowchart.

This standard pipeline has E to B leakage on the same level as instrument noise, because of partial sky coverage, and data filtering. As in Bicep2, we use a matrix base technique to construct the 'purification matrix' that separates out the true, pure
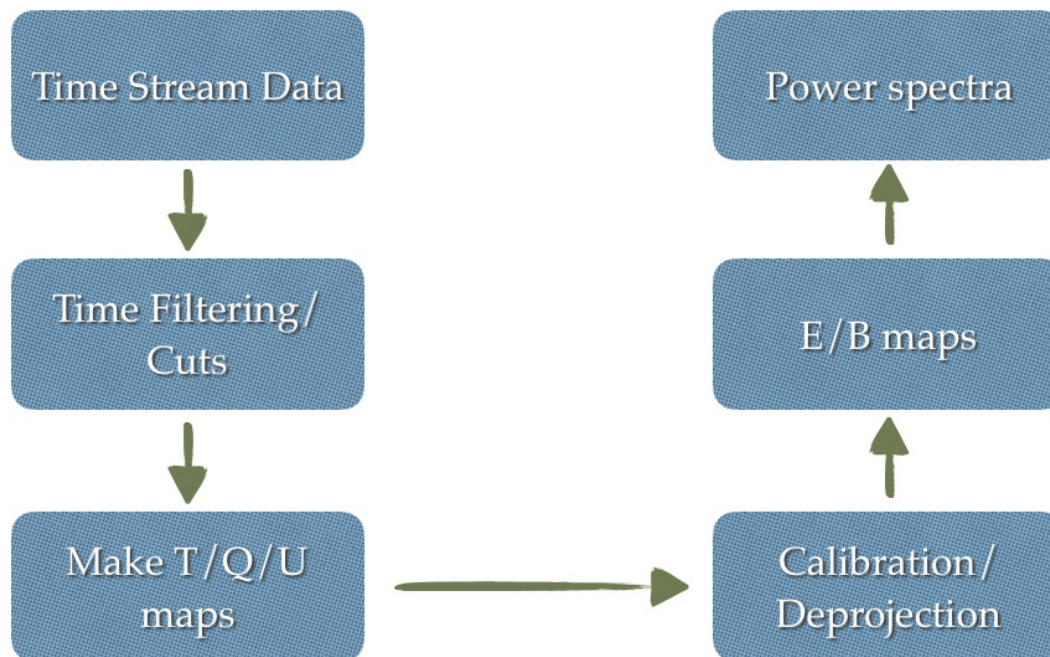
Figure 5.1: A simplified version of the analysis flowchart, showing how the timestreams data are turned into maps and finally power spectra

B mode from the rest of the signal.

Finally, to test against instrument systematics, a series of jackknife tests are formed, and we can statistically measure the systematics associated with the instrument and atmosphere by comparing the jackknife power spectra to a distribution of simulated signal plus noise spectra.

5.1 Low-level reduction

Timestream data from all the detectors are down-sampled, stored, and transferred from the South Pole to North America via satellite. They are stored and analyzed at the Odyssey cluster at Harvard University.

De-glitching

The first step of the analysis chain is to de-glitch the data, which removes and corrects spikes and discontinuous steps in the signal. These imperfections in the data are generally caused by cosmic ray hits on the TES island, or a 'flux jump' in a SQUID, causing it to jump from one lock point to another.

For spikes, TOD is cut one second before and after glitch. For discontinuous steps caused by flux-jump, the step is removed by matching the DC level of TOD before

and after the glitch.

Relative gain

Data through this step is stored in analog to digital units (ADU), which are non-uniform for all the detectors in BICEP3. The relative gain between these detectors are calibrated by performing an elevation nod ('elnod') at constant azimuth before and after every scanset. This ~1.2 degrees elevation motion resulted the detector respond in a well modeled, *secant* function, caused by the elevation gradient in sky temperature. This relative gain, η, is calculated and corrected for each detector. The final CMB temperature calibration of the instrument is done by correlation with *Planck* temperature map and is performed later in the pipeline.

Time stream pair sum and difference

After each channels are relatively normalized, the timestream can be described by

$$d = g\left[T + \gamma\left(Q\cos 2\psi + U\cos 2\psi\right)\right] \tag{5.1}$$

where g is the gain, γ is the polarization efficiency, ψ is the polarization orientation projected onto the sky and T, Q, U are the Stokes parameters.

Ultimately we are interested in polarization data, the pair-differenced signal from the orthogonal detector pair is

$$d_{\text{diff}} = \frac{1}{2}\left(\frac{d_a}{g_a} - \frac{d_b}{g_b}\right) = \frac{1}{2}\left(\alpha Q + \beta U\right) \tag{5.2}$$

where a and b are the two orthogonal detectors, and

$$\alpha = \gamma_a \cos 2\psi_a - \gamma_b \cos 2\psi_b \tag{5.3}$$

$$\beta = \gamma_a \sin 2\psi_a - \gamma_b \sin 2\psi_b \tag{5.4}$$

are the polarization orientation information.

Selection and cuts

Before the data are combined and coadded into maps, we use a multi-level data cutting algorithm to identify and remove low quality and corrupt data. These are the data affected by readout electronics, multiplexing, weather, and other atypical instrument behaviors. We do not remove noisy channels, those data are accordingly weighted by calculating the variance of each pairmap.

This selection process is divided into Round 1 and Round 2 cuts. Round 1 are applied for individual halfscans, and Round 2 cuts are calculated at each scanset. Table 5.1 and 5.2 show the cuts in 2016 for BICEP3 data.
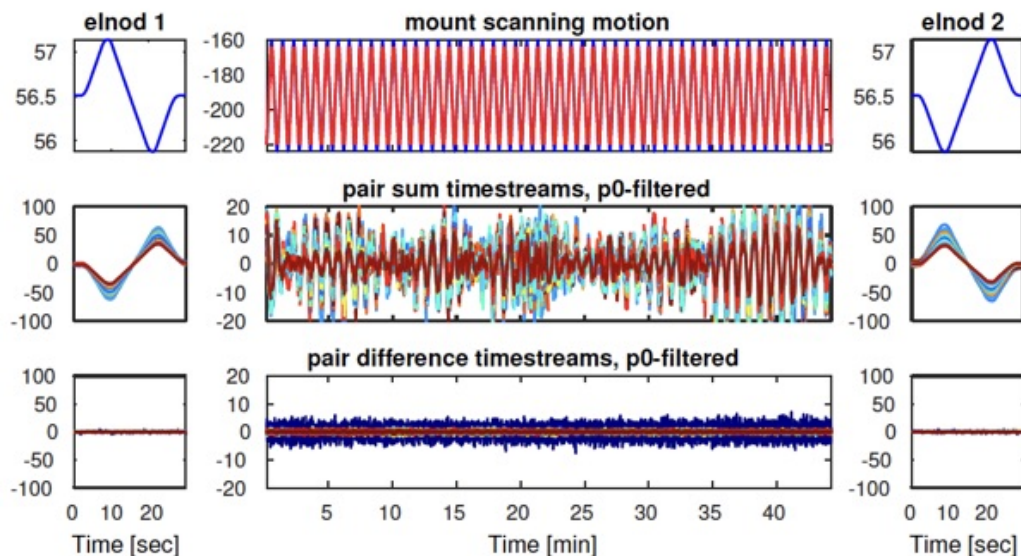
Figure 5.2: One scanset of the timestream data. Top panel shows the mount motion across azimuth, while scanning at a constant elevation. Middle panel is the pair sum data, which is heavily affected by atmospheric noise. Bottom panel is the pair difference data, because the atmosphere is mostly unpolarized, most of the common mode noise is removed. The left and right panels are the el-nod calibration step to calculate relative gain of each detector, as they are well modeled by a *secent* function. Different colors in the figure represent different detectors in BICEP3, each channels are weighted according to their noise variance. Figure from Justin Willmert.

Table 5.1: BICEP3 2016 Round 1 cut parameters and pass fraction

Cut parameter	Threshold	Pass fraction	Unique Cut fraction
fp_nancount	0	0.99	0.0001
fp_std_p0	[0 Inf]	0.99	0.0000
fp_std_p3	[0 Inf]	0.99	0.0000
fp_std_sd_p0	[0 Inf]	1.00	0.0000
fp_std_sd_p3	[0 Inf]	1.00	0.0000
fp_std_uncal	[0 Inf]	0.86	0.0000
is_fj_row	1.5	1.00	0.0000
fp_fj_col	1.5	1.00	0.0000
syncsampnum_diff1	0	1.00	0.0000
syncsampnum_diff2	0	1.00	0.0000
passfrac_col	> 0	1.00	0.0000
passfrac_chan	> 0	1.00	0.0000
Round 1 Overall		0.99	

Table 5.2: Bɪᴄᴇᴘ3 2016 Round 2 cut parameters and pass fraction

Cut parameter	Threshold	Pass fraction	Unique Cut fraction
manual		1.00	
elnod_mean	[90 30000]	0.81	0.0009
elnod_fracdel	0.3	0.85	0.0000
elnod_ab_ba	0.04	0.79	0.0040
elnod_median	[2000 5000]	0.99	0.0000
elnod_nancount	0	0.96	0.0000
elnod_gof	75	0.86	0.0044
elno_chisq_dif	10	0.92	0.0012
fb_wn_sd_p0	Inf	0.98	0.0000
fb_1f_sd_p0	Inf	0.98	0.0000
skewness_dif	0.2	0.88	0.0030
satcom	6	0.97	0.0002
fp_cor	1	1.00	0.0000
scanset_std	2.5	0.76	0.0173
stationarity_ab	[0 0.7]	0.92	0.0005
stationarity_dif	[0 0.2]	0.86	0.0009
tfpu_mean	[0.25 0.35]	1.00	0.0000
tfpu_std	5e-5	0.99	0.0000
az_range	100 deg.	1.00	0.0000
num_fj	5	0.99	0.0000
num_destep	5	0.87	0.0092
max_fj_gap	1000 sample	1.00	0.0016
rtes_frac	[0.10 0.95]	0.97	0.0071
rnorm	[0 Inf]	1.00	0.0000
pjoule	[0 Inf]	1.00	0.0000
passfrac_halfscan	> 0.9	0.98	0.0071
passfrac_scanset	> 0.3	0.87	0.0112
Round 2 Overall		0.61	
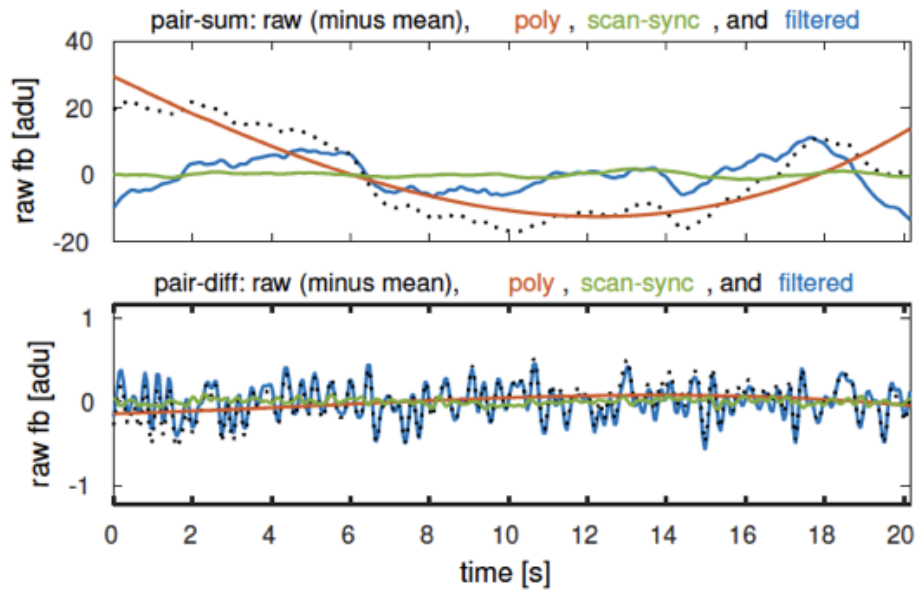
Figure 5.3: Sample pair-sum and pair-difference timestreams. It highlights the third order polynomial, scan-sync, filtered components that subtracted from the TOD. Figure from Justin Willmert.

Filtering and ground subtraction

Each halfscan of data are filtered with a third order polynomial to account for the weather variation. A fixed-azimuth ground template is formed by taking the average over the hour of data and removed from each scan.

5.2 Map making

To make maps from TOD, data are binned into a 0.25 degree pixel with appropriate declination and right ascension.

Inverse variance weighting

The filtered, pair differenced TOD are binned into 0.25 degree pixels, the Stoke Q and U maps are related to the pair differenced maps:

$$\sum \omega \begin{pmatrix} d_{\text{diff}}\alpha \\ d_{\text{diff}}\beta \end{pmatrix} = \frac{1}{2} \sum \omega \begin{pmatrix} \alpha^2 & \alpha\beta \\ \alpha\beta & \beta^2 \end{pmatrix} \begin{pmatrix} Q \\ U \end{pmatrix} \tag{5.5}$$

where ω is the weighting for each detector pair and scanset. It is the inverse variance of the data set. Figure 5.4 shows the weighting in the 2016 data set that used in the final coadded map.
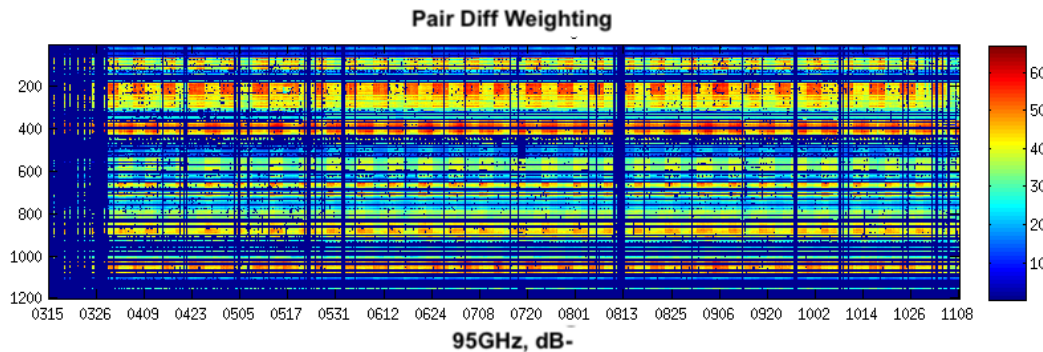
Figure 5.4: Data weighting used in Bicep3 2016 data. Left: Y-axis shows the detectors, and X-axis is the observing time in 2016. The blue straps usually indicate bad weather cut, while the red block pattern is showing known elevation gain dependance on the detector.

The Q and U maps are produced by inverting equation 5.5, which will need multiple deck angles since a single polarization matrix is not invertible.

Pairmaps

"Pairmaps" are constructed from the TOD data, these are individual tag map that have not been combining with other time period. These pairmaps are formed on a per-scanset basis, and coadded over a phase to form a per-phase pairmap.

This data storage structure allow us to form many different combination of maps with freedom of applying different filtering and cuts without repeating the low-level reduction. Typically the deprojection [56] and Round 2 cuts are applied while these pairmaps are formed.

Coadding maps

The final step of the map making procedure is to combine (coadd) all the pairmaps, and form a final $[T, Q, U]$ map for the entire season. Different coadded map are formed to test data consistency (Section 5.6) as well as final science maps. Figure 5.5 compares E-modes measured by Bicep3 and *Keck Array*.

CMB-derived pointing

The overall pointing of the telescope is monitored by a optical star camera installed next to the Bicep3 receiver. We use the *Planck* CMB temperature to correct the individual detector pointing within the receiver. The *Planck* 100 GHz temperature is smoothed to the Bicep3 beam profile as an input map.
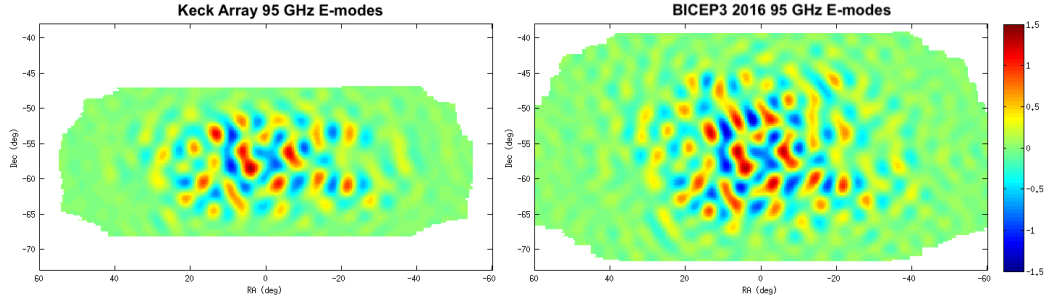
Figure 5.5: *E*-modes map measured by Bɪᴄᴇᴘ3 and *Keck Array*. Single receiver-year of Bɪᴄᴇᴘ3 achieved similar map depth as four receiver-year of *Keck Array*.

Table 5.3: Absolute calibration in Bɪᴄᴇᴘ3

Year	Absolute calibration [μK/fpu]
2016	4285
2017	3295

Pairmaps from Bɪᴄᴇᴘ3 are produced using the ideal beam centers, then is it split into different deck angles, and individual detector maps. Correlations for each detector from each map are calculated with respect to the reference *Planck* map. These correlations provide us a corrected observed detector beam centers, differential pointing, and χ angles which correction the overall rotation of beam pointing. Figure 5.6 shows the pointing offset we observed in 2016 Bɪᴄᴇᴘ3.

Absolute calibration

The absolute calibration of the data is performed by comparing the power spectrum of the temperature map with the smoothed *Planck* 100 GHz map describes in Section 5.2. The map is cross correlated with the *Planck* 145 GHz temperature to avoid a noise bias in the auto-correlation. Each multiple bin is calibrated as:

$$g_l = \frac{\sum_m \left\langle a_{lm}^{Planck145} a_{lm}^{\text{Bicep3}} \right\rangle}{\sum_m \left\langle a_{lm}^{Planck145} a_{lm}^{Planck100} \right\rangle} \tag{5.6}$$

The final calibration number is average over the l range of 30-210. Table 5.3 shows the absolute calibration for the 2016 and 2017 data. The decrease in number in 2017 is largely due to the instrument sensitivity improvement in 2017 (Section 4.8).

During this analysis, we found the calibration factor decreased about 20% over the l bins (Figure 5.7). This is partly due to the possibility that the beam profile
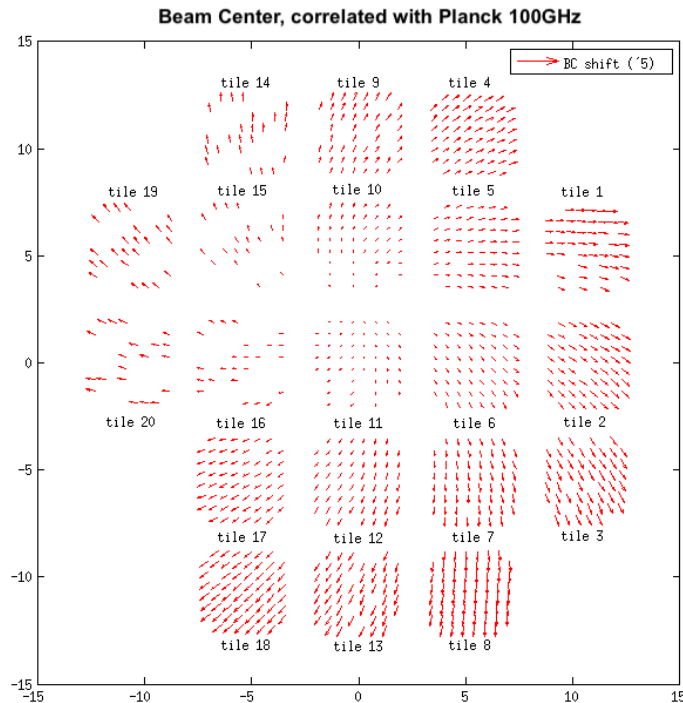
Figure 5.6: CMB-derived pointing correction for Bicep3 in 2016. The radially outward correction is due to the large area, flat focal plane and causes the edge pixels be slightly out of focus. Yield hit in MCE3 (top left modules) are clearly visible due to cold wiring opening.

(Section 4.10) used to smooth the input *Planck* temperature maps does not match the real beam. It is possible that the far field flat mirror used in the measurement curved and distorted the beams during calibration. We modified the beam map-derived B_l by using a polynomial fit model to correct the beam profile at high l so the absolute calibration is constant across all the l bins. While the polynomial fit is not physically motivated, the multiple degrees of freedom allows us to flatten the calibration factors while keeping the power at high l relatively small (Figure 5.8).

5.3 Simulation

The error in the power spectrum is calculated by performing monte carlo simulations of the noise and the signal. We generated 499 realization for each simulate map types.

Four types of simulations are created: unlensed ΛCDM, lensed ΛCDM, dust, and tensor *B*-mode with $r = 0.1$.
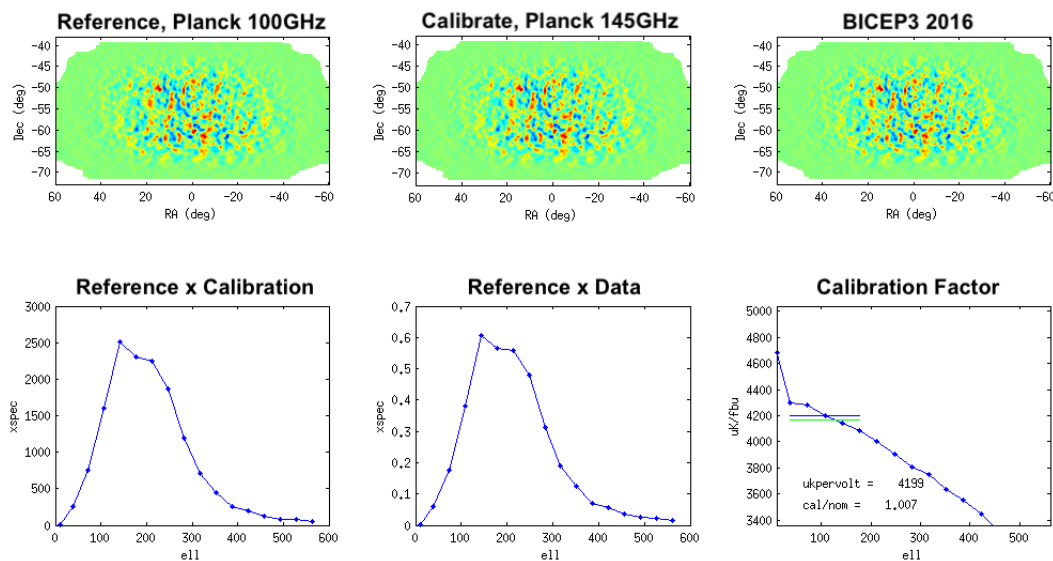
Figure 5.7: Absolute calibration using *Planck* input maps that are smoothed by a measured BICEP3 far-field beam profile. The 145 GHz temperature map is used as reference, and the 100 GHz is used for calibration. The decrease of the calibration factor over the l bins is due to inaccurate calibration of the BICEP3 beam profile.
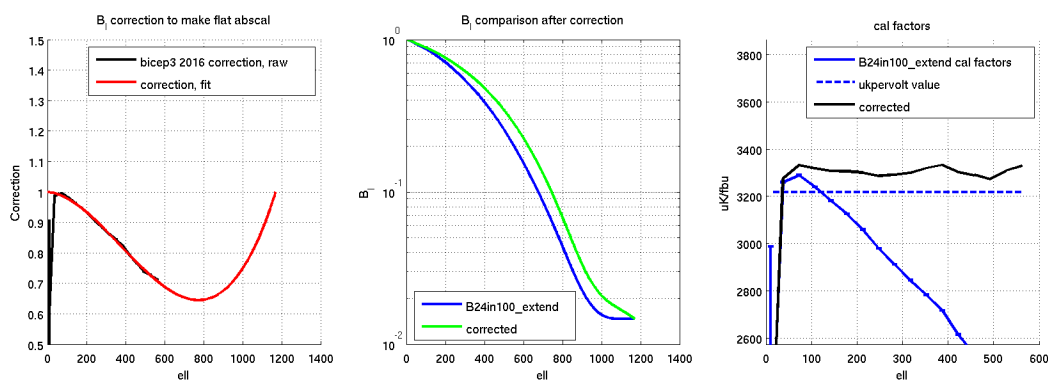
Figure 5.8: Left: Correction factor comparing to the measured beam profile. Middle: Measured and polynomial fit beam window function B_l. Right: Absolute calibration factor of the two methods over l bins. Figure from: Tyler St. Germaine.

Signal simulations

The signal only simulated map was first created by calculating the C_l for the current best fit parameters in ΛCDM cosmology. The C_l are used to generate high resolution `Healpix` maps that serve as the starting point for each realization of the simulations.

The *Planck* temperature maps are used as the starting point for the realization of the polarization field, by using the *Planck* needlet internal linear combination (NILC) T map. By fixing the temperature constrain, only the polarization field varies in these realization, this is because the true CMB temperature sky has been measured to extremely high precision and the main goal of the experiment is to measure the polarization field of the CMB.

After the a_{lm}^T was calculated using the `synfast` software from the `Healpix` package. A E-mode realization sky is made from the measured temperature sky with known TE correlation. The coefficients of the spherical harmonics, a_{lm}, for the E-modes sky are:

$$a_{lm}^E = \frac{C_l^{TE}}{C_l^{TT}} a_{lm}^T + \sqrt{C_l^{EE} - \left(C_l^{TE}\right)^2 / C_l^{TT}} \, n_{lm} \tag{5.7}$$

where the C_l's are ΛCDM spectra from `CAMB` with cosmological parameteres taken from *Planck*, and the n_{lm} are normally distributed complex random numbers.

The temperature map in the *Planck* NILC map have been lensed by the intervening structure between us the the surface of last scattering. This means the a_{lm}^T calculated from it contain the effects of lensing and propagated through to the constrained a_{lm}^E. Hence we used a lensed C_l^{TT} to correct this effect. In practice, the multipole range of interest in BICEP, even up to $l = 600$, lensing has a very small impact on a_{lm}^T.

After these maps are generated, the simulated maps are smoothed with the measured far-field beam profile from BICEP3, and the last step is to re-observe these maps with the same map making procedure describes in Section 5.2.

Noise simulation

The noise in BICEP3 comes from many different sources: detector photon and phonon noise, SQUIDs readout electronic, cryogenic pulse tube and others. It is difficult and unnecessary to model each noise source independently, because the noise models used in our analysis are indifferent to the source. Instead the data itself is used as the template to create the noise model.

The noise model in the pipeline is simulated through a "sign-flip realizations". For each noise realization, a positive and negative sign is randomly assigned to each

per-phase maps, such that the positive and negative halves are equally weighted. When the maps are coadded together, the signal is averaged out, but the noise level remains the same. This noise simulation is also repeated for 499 realizations and combining with the signal simulated maps.

5.4 Power Spectra

The maps are converted into the angular power using the `MASTER` procedure, it provides a way to transform one dimensional spectra $\tilde{C}_{l'}^{XX}$ into an estimate for the full sky spherical harmonic coefficients, $C_{l'}^{XX}$.

After coadding, calibrating and deprojecting all the pairmaps. We now have these pixelized, partial temperature, and polarization (Q,U) sky maps. The flat sky estimate for the angular power spectra is calculated using the Discrete Fast Fourier Transform:

$$\tilde{T}(l) = \sum_{x,y} W(x, y) T(x, y) e^{-i(l_x x + l_y y)} \tag{5.8}$$

where x, y is the position in the map and l is the position in the Fourier Plane. The window function W apodizes the full sky map by using the binned weights.

To form a one dimension angular spectra, the radial $l = \sqrt{l_x + l_y}$ are binned into top hat bins l'

$$\tilde{C}_{l'}^{XX} = \left\langle \tilde{X}(l) \tilde{X}(l) \right\rangle_{l'} \tag{5.9}$$

The measured one dimension angular spectra $\tilde{C}_{l'}^{XX}$ relates to the true CMB power spectrum

where X and Y refer to T, Q and U maps, and the band power window function F accounts for the filtering filtering that removes and mixes power and N is the ensemble average of the noise contribution to the spectra.

Noise N is calculated through the noise simulation and subtracted from the real points. The band power window function F is calculated from special signal simulations. Single l simulations are produced and observed using the observation matrix. The filtering and the pixelization mix and suppress the resulting bandpower. 499 simulations were used to calculate the band-power window functions and suppression factors.
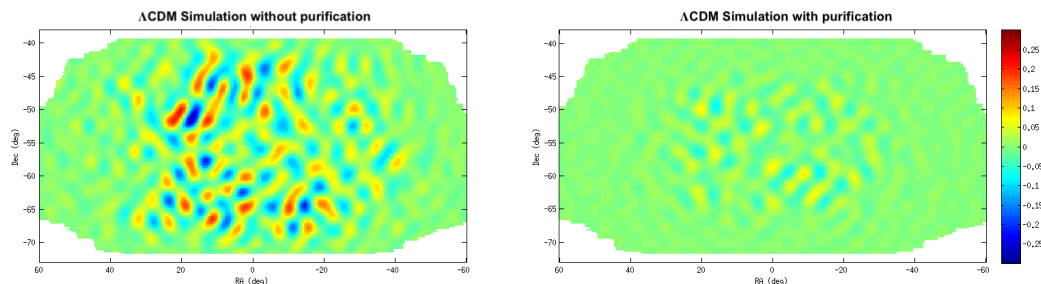
Figure 5.9:   Example of leaked *B*-modes. Left: A ΛCDM simulation process through the standard pipeline, showing E to B leakages due to partial sky coverage and filtering of the data. Right: Same simulation with purification matrix applied. The noise level is much smaller than instrument noise.

5.5   Matrix based E/B Separation

Section 5.2 shows the steps to separate the polarization field into E and B modes, but this mathematical framework only work in an ideal case. Figure 5.9 shows an example of leaked *B*-modes from *E*-modes, using a simulated ΛCDM map, the leak amplitude is similar to the instrument noise level.

The leakages come from the fact that we did not measure the full 4π steradians of sky, and our data are heavily filtered. These non-idealities in the analysis mix the much brighter *E*-modes into the faint *B*-modes we want to detect.

While [57] presents an estimator that fixes E to B leakage arise from partial sky coverage. This does not prevent leakages due to data filtering. BICEP2 developed a set of analysis techniques based on matrix operators (Matrix based separation), allowing us to separate the true sky *E* and *B*-modes with orders of magnitude less leakage. The detail of this procedure is described in detail in [53] and [52]. This section describes how this technique is applied to BICEP3's data.

Observing matrix

Section 5.2 describes low-level data process and map making steps, including data selection, polynomial filtering, scan-synchronous signal (ground) subtraction, inverse variance weighting, binning into map pixels, and deprojection of leaked temperature signal. These operations are performed sequentially in the standard pipeline, in this matrix base procedure, an matrix is constructed to represent each of these steps. The final observation matrix *R* is the multiply of these matrices, which
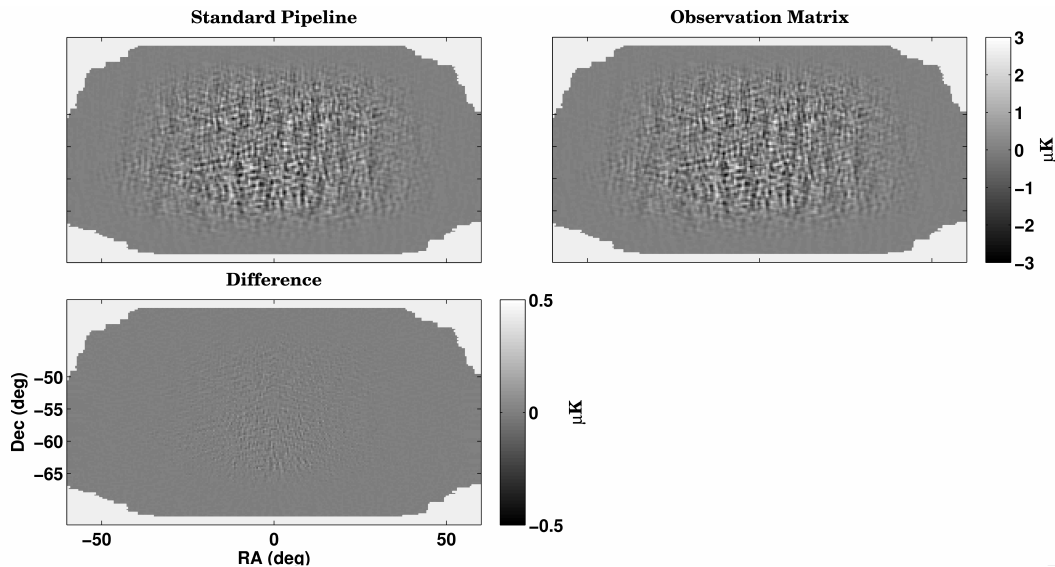
Figure 5.10: Comparison between the observation matrix and standard pipeline. The input map for both is from the same simulation realization. Figure from Jae Hwan Kang.

performs all of the operations at once. The matrix R is a 3×3 block of matrices:

$$
R = \begin{bmatrix} R_{TT} & 0 & 0 \\ 0 & R_{QQ} & R_{QU} \\ 0 & R_{UQ} & R_{UU} \end{bmatrix} \tag{5.10}
$$

Each block acts on a cut-sky `Healpix` map vector and produces a BICEP3 map vector. A single column in the matrix is the `Healpix` map pixel contribution to the BICEP3 map pixels. Figure 5.10 demonstrates the matrix operation produce the same result as the standard analysis pipeline.

Observed signal pixel-pixel covariance matrices

Section 5 in [52] details the same analysis done in BICEP2. The signal covariance matrix C_l contains the pixel-pixel convariances of a map for a given spectrum of Gaussian fluctuations. Its diagonal entries contain the variance of each pixel, and each row describes the convariance of a given pixel with the other pixels in the map.

We generate C_B and C_E from $1/l^2$ theory B and E mode only power spectrum. The observed pixel-pixel theory covariance $\tilde{C}$ is:

$$
\tilde{C}_B = R C_B R^T \tag{5.11}
$$

$$
\tilde{C}_B = R C_B R^T \tag{5.12}
$$
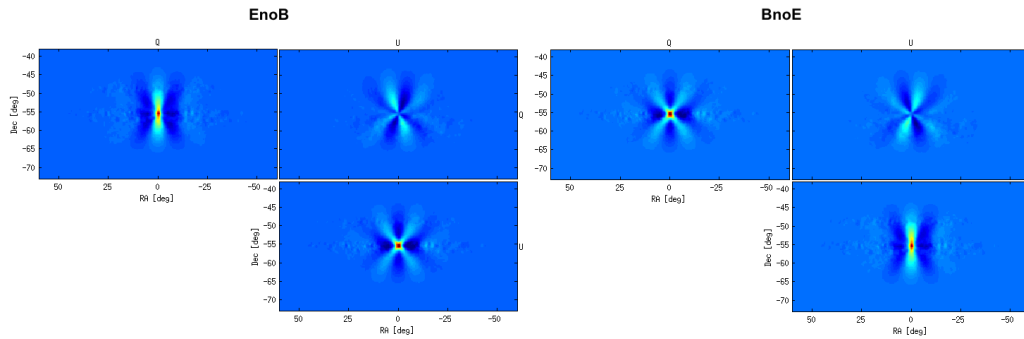
Figure 5.11: Reobserved pixel-pixel covariance matrices. Figure from Jae Hwan Kang.

where R is the observation matrix. If we consider the matrix as a series of column vectors, each column represents the map vector that contains the covariance for a particular pixel with every other pixel in the map. Figure 5.11 shows pixel-pixel covariance matrices after being reobserved by the observation matrix for the center map pixel.

Purification matrix

After constructing the observed signal covariance matrices, we can solve for the generalized eigenvalue problem that allow us to seperate the pure E and B mode.

$$\left(\tilde{C}_\mathrm{B} + \sigma^2 I\right) x_i = \lambda_i \left(\tilde{C}_\mathrm{E} + \sigma^2 I\right) x_i \tag{5.13}$$

that $\sigma^2 I$ is added to make the matrix non-singular.

Followed the same definition, the pure E-modes are kept upto the cutoff $\lambda = 0.98$, and the same number of B-modes are kept. Figure 5.12 is the result of solving the generalized eigenvalue problem. The smaller beam size of BICEP3 comparing to *Keck Array*, we were able to retain larger number of pure B-modes, showing better sensitivity to small scale features. Figure 5.9 compares a simulated ΛCDM input map using the standard pipeline and matrix purification, demonstrates the effectiveness of this technique.

Band power window function

The matrix based analysis transforms an input `Healpix` map into an observed map. The input maps m_l are delta functions in multipole l, and observed using the matrix R. The procedure uses two sets of `Healpix` maps, where first one set
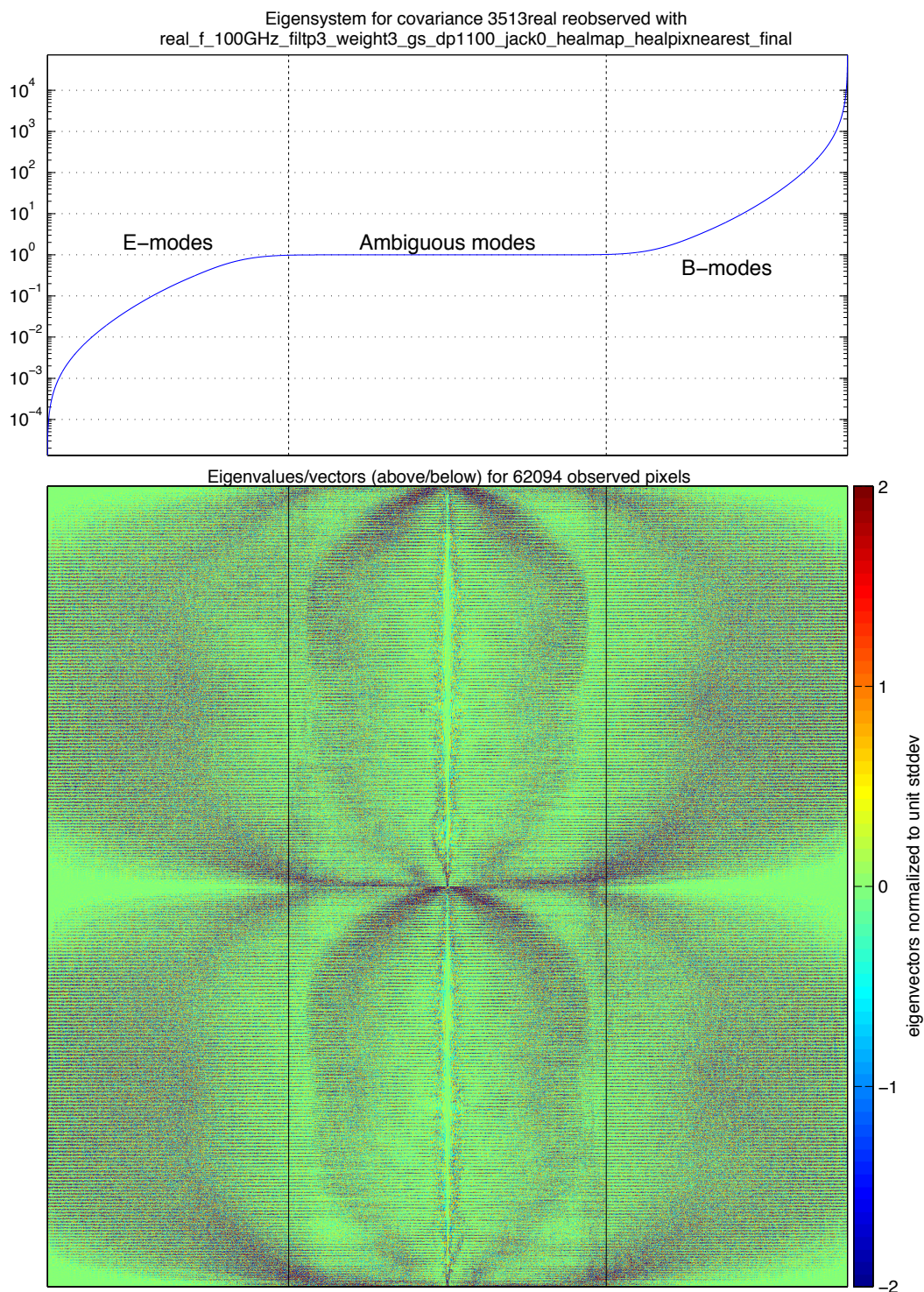
Figure 5.12: Generalized eigenvalue problem for the purification matrix. Top panel is the eigenvalues in order of their value. Bottom is the corresponding eigenvectors as columns with color shows the magnitude of the components.

Table 5.4: Band power window function

Bin Number	Nominal			Measured		
	low	center	high	low	center	high
1	20.0	37.5	55.0	35.0	44.6	52.0
2	55.0	72.5	90.0	59.0	72.4	84.0
3	90.0	107.5	125.0	90.0	105.1	119.0
4	125.0	142.5	160.0	120.0	137.7	155.0
5	160.0	177.5	195.0	150.0	169.6	190.0
6	195.0	212.5	230.0	179.0	200.8	226.0
7	230.0	247.5	265.0	209.0	232.2	261.0
8	265.0	282.5	300.0	238.0	264.2	296.0
9	300.0	317.5	335.0	268.0	296.5	332.0

$TT = TE = EE = 1$, and the second one set with $TT = BB = 1$. Maps are created using the observation matrix for $l = 1$ through 700, with 100 random realizations for each l.

The band power window function, $M_{ll'}^{XX}$ for band power l', is a function of input multipole of the delta function, l:

$$M_{ll'}^{XX} = \frac{\sum^{N} F_{ll'} (Rm_l)}{N} \tag{5.14}$$

where $F_{ll'}$ is the analysis transformation from map to power spectra and $XX = \{TT \rightarrow TT, TE \rightarrow TE\ EE \rightarrow EE, EE \rightarrow BB, BB \rightarrow BB, BB \rightarrow EE\}$. Calculating the band power window functions accounts for all aspects of our instrument and analysis. Table 5.4 shows the "nominal" and "measured" centers and edges of the band power bins; where nominal refers to the defined range of annular rings in the two dimensional power spectra and measured is the center and $\pm 1\sigma$ range found in the end to end calculation.

5.6   Internal consistency

Internal consistency checks are performed to test our data against instrumental systematics. A series of 15 jackknifes are performed by splitting the data into two equally weighted halves, and then subtracting the two. The differenced data result are then run through the same analysis pipeline to the final power spectra.

If a signal exists in only half of the data, then it should show up with as much significance in the jackknife as in the final science product. However, some of

the jackknifes are more sensitive to systematics than the sum because of inherent cancelation effects.

Here is a brief summary of the jackknifes:

- **1. Deck angle:** The telescope is rotated about its boresight every 2-3 days. Signals change sign under rotation are amplified by differencing orientations. This jackknife splits the data of 23, 68 degree vs 23, 248 degree.

- **2. Scan direction:** This splits the data based on the scanning direction. This is sensitive to slow transfer function and differential scan rate.

- **3. 1st/ 2nd half weight:** This splits the data based on observation date, into first half and second half equally weighted data. This is sensitive to temporal systematic.

- **4. Detector Tile:** Splits data by detector tile, to check for systematics arising from differences in tile fabrication (Figure 5.13).

- **5. Phase (az):** Splits data according to scan schedule phases. The two group are only partially overlap in azimuth. This is sensitive to fixed azimuth (ground) contamination.

- **6. Mux column:** Splits data according to readout SQUID columns. This is sensitive to readout crosstalk contamination.

- **7. Alt deck:** Splits data similar to **deck angle**, but separate the data into 68, 203 degree vs 23, 248 degree.

- **8. Mux row:** Splits data according to readout SQUID rows, similar to **mux column**.

- **9. Tile/deck:** Splits data from detectors on tiles on different deck angles.

- **a. Focal Plane inner/outer:** Splits data based on radial position in the focal plane. This is sensitive to forebaffle reflections and sidelobes contamination.

- **b. Tile top/bottom:** Splits data from detectors in the top of the tile vs. the bottom of the tile to check for detector fabrication.

- **c. Tile inner/outer:** Splits data from detectors in the center of the tile vs. edge of the tile to check for detector fabrication.
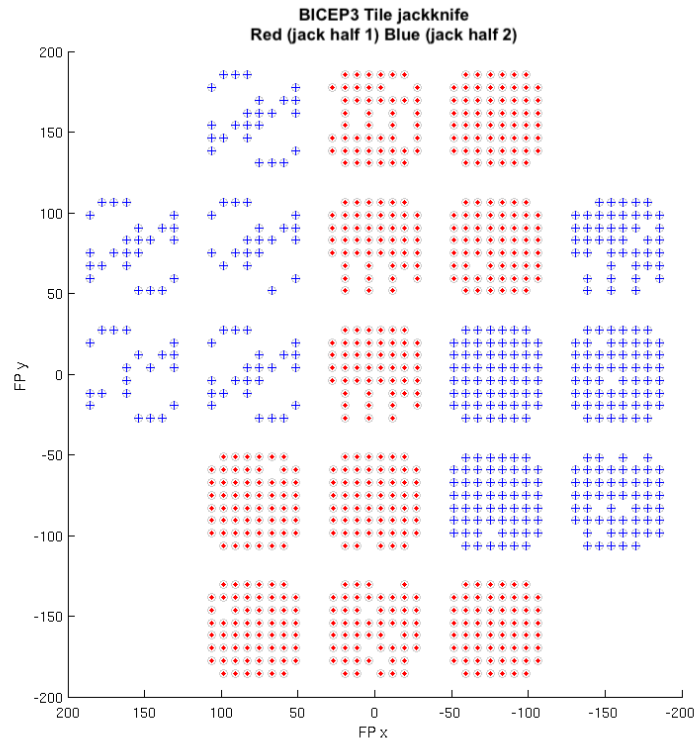
Figure 5.13: Tile jackknife definition in BICEP3. This jackknife splits the data into two groups base of detector tile, shown in red and blue in focal plane map. This allow us to probe systematic arise from tile fabrication.

- **d. Moon up/down:** Splits data based on the position of the moon, to examine contamination from the moon.

- **e. Differential pointing best/worst:** Splits data based on beam mapping measurement. The first half are pairs with the worst differential A/B pointing, and second half are the reverse. This is to check the effectiveness of the deprojection.

Comparing the jackknife power spectra to a distribution of simulated spectra from sugnal plus noise simulations, we statistically determine wether a jackknife is considered passing or failing. Though these jackknifes, we test our systematic associate with the instrument, ground and atmosphere.

We evaluate whether a jackknife passes using Probability To Exceed (PTE), which states what the probability is of having a simulation with the same band power as the real data.

The χ^2 statistic is calculated base on the measured jackknife band powers against the mean of the signal plus noise simulations:

$$\chi^2 = (d - \langle m \rangle)^T M^{-1} (d - \langle m \rangle) \tag{5.15}$$

where M^{-1} is the band power covariance matrix, d are the observed band powers and $\langle m \rangle$ is the mean of the ΛCDM signal + noise simulations.

The standard χ^2 statistic computes deviation from expectation, but does not include sign information. For that, we calculate the χ statistic:

$$\chi = \sum_i \frac{d_i - \langle m_i \rangle}{\sigma_{m_i}} \tag{5.16}$$

Given a set of Monte Carlo simulations, the PTE can be found directly from a histogram of simulations. The full analysis uses 499 realizations to calculate the PTE, but only 49 realizations have been simulated by the time of this dissertation.

The preliminary result below are calculated using 49 realizations. The PTEs from jackknife χ^2 and χ tests for the polarization-only (EE, BB, EB) spectra are presented in Table 5.5 and 5.6. We evaluate the results of the jackknife tests as pass if the PTEs are > 0.01 and < 0.99, and the PTE from all jackknifes should be uniformly distributed between zero and one. Out of 84 testes using the first 5 band powers, the temporal split EE χ is > 0.99 and Azimuth (phase) BB χ^2 is < 0.01. Figure 5.15 show the χ distribution of these two jackknife, which show that it is very close to the edge of the distribution and will require more data to draw an conclusive result.

Figure 5.14 is the distribution of the jackknife χ^2 and χ PTE values over the 14 tests and three spectra, and it is consistent with uniform.

Table 5.5: Jackknife PTE values from χ^2 and χ (sum of deviation) test with 49 realizations

Jackknife	Band powers 1-5 χ^2	Band powers 1-9 χ^2	Band powers 1-5 χ	Band powers 1-9 χ
Deck				
EE	0.408	0.408	0.490	0.347
BB	0.531	0.163	0.898	**1.000***
EB	0.796	0.796	0.143*	0.163
Scan Dir				
EE	0.796	0.082	0.224	0.041
BB	0.388	0.224	0.673	0.939
EB	0.898	0.755	0.878	0.327
Temporal split				
EE	0.102	0.327	**0.999***	0.959
BB	0.306	0.245	0.245	0.327
EB	0.694	0.551	0.898	0.469
Tile				
EE	0.143	0.469	0.163	0.245
BB	0.735	0.571	0.735	0.633
EB	0.918	0.735	0.653	0.490
Azimuth				
EE	0.327	0.531	0.592	0.898
BB	0.020	0.041	**0.002***	**0.004***
EB	0.714	0.122	0.224	0.367
Mux col				
EE	0.265	0.204	0.367	0.367
BB	0.776	0.571	0.592	0.306
EB	0.980	0.959	0.429	0.816
Alt deck				
EE	0.224	0.306	0.980	0.983*
BB	0.143	0.082	0.061	0.735
EB	0.306	0.531	0.163	0.102

Table 5.6: Jackknife PTE values from χ^2 and χ (sum of deviation) test with 49 realizations cont'

| Jackknife	Band powers 1-5 χ^2	Band powers 1-9 χ^2	Band powers 1-5 χ^2	Band powers 1-9 χ
Mux row				
EE	0.061	0.122	0.714	0.776
BB	0.776	0.939	0.653	0.673
EB	0.061	0.204	0.816	0.551
Tile and deck				
EE	0.796	0.878	0.612	0.306
BB	0.429	0.184	0.959	0.939
EB	0.735	0.694	0.204	0.388
Focal plane inner/outer				
EE	0.531	0.143	0.592	0.796
BB	0.490	0.408	0.837	0.878
EB	0.102	0.286	0.653	0.714
Tile top/bottom				
EE	0.184	0.041	0.918	0.633
BB	0.735	0.163	0.837	0.286
EB	0.592	0.592	0.347	0.735
Tile inner/outer				
EE	0.347	0.653	0.755	0.714
BB	0.265	0.531	0.082	0.367
EB	0.980	0.959	0.612	0.816
Moon				
EE	0.327	0.224	0.143	0.612
BB	0.490	0.816	0.985*	0.939
EB	0.694	0.755	0.286	0.857
A/B offset best/worst				
EE	0.612	0.939	0.837	0.816
BB	0.061	0.041	0.918	0.980
EB	0.204	0.245	0.694	0.469
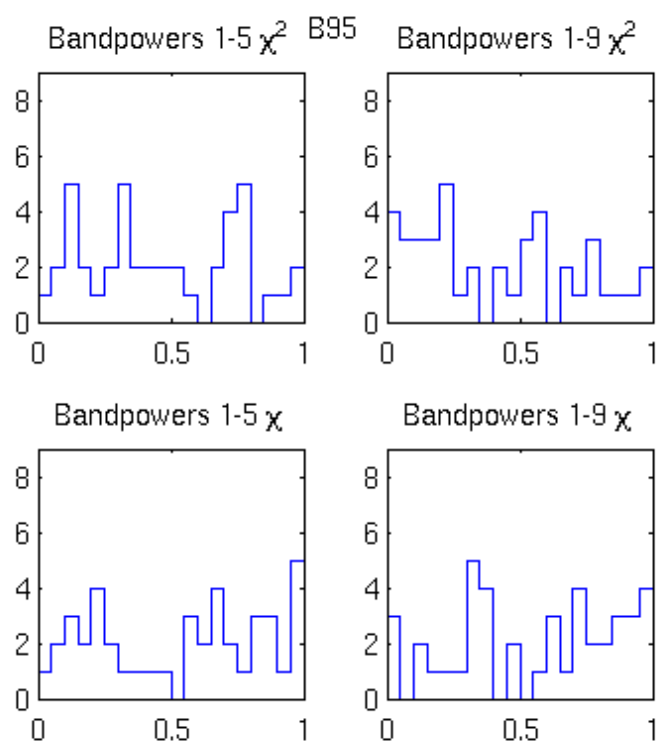
Figure 5.14:   Distribution of the jackknife χ^2 and χ PTE values over the 14 tests and three spectra.
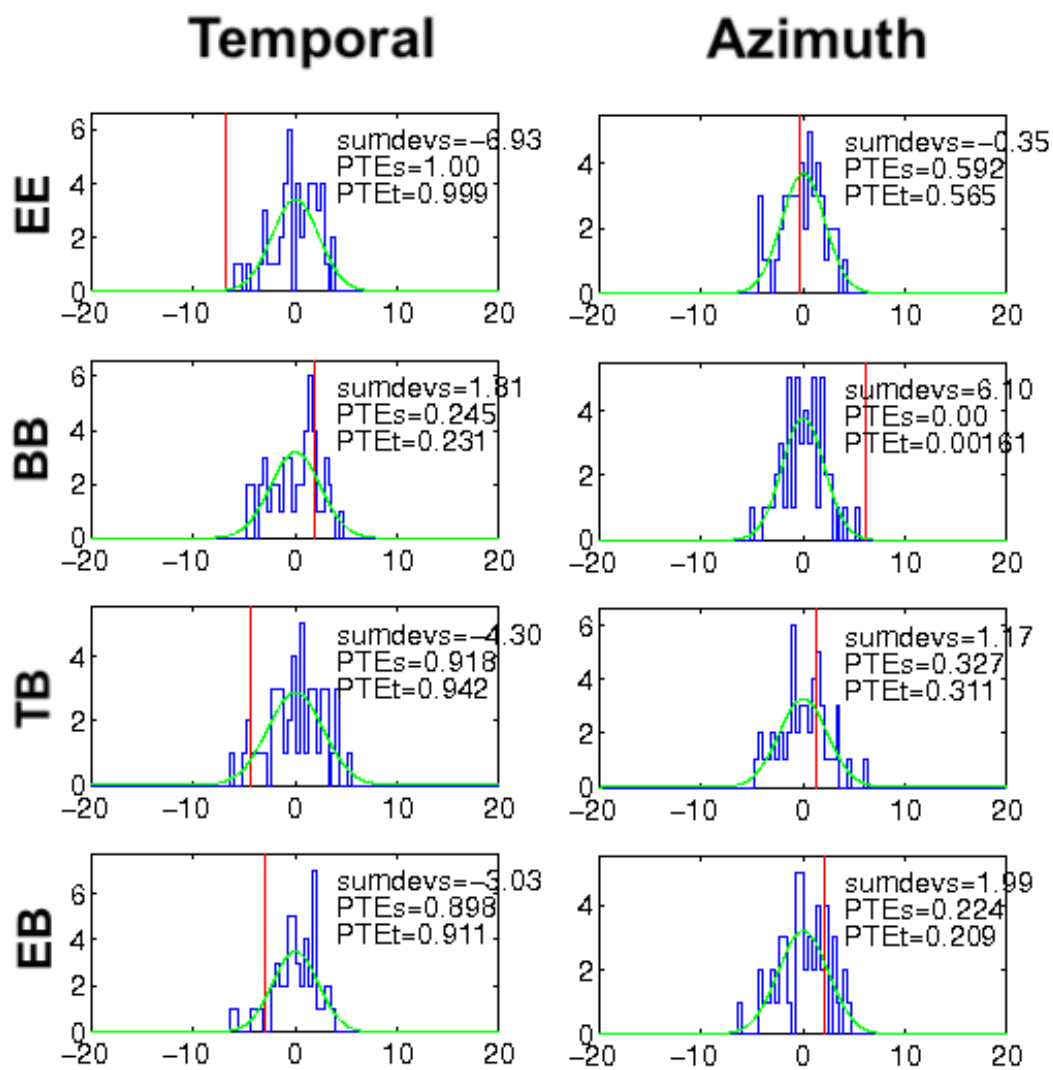
Figure 5.15: Temporal and azimuth jackknife χ PTE using 49 realizations

Chapter 6

PATH FORWARD

6.1 Cosmology constraint

Latest result from Bicep/*Keck Array* 2015

The latest published result from our collaborations includes all the observation up to the 2015 season (BK15). We produced CMB polarization maps reach depths of 5.2, 2.9, and 26 μK_{cmb}-arcmin at 95, 150, and 220 GHz, respectively over an effective area of 400 square degree. The likelihood analysis yields the constraint on tensor-to-scalar ratio $r < 0.06$ at 95% confidence in conjunction with *Planck* temperature measurements and other data (Figure 6.1).

Combining with Bicep3 data

At the time of writing this dissertation in May of 2018, the data collected from Bicep3 is still being analyzed, and it is not included in the latest published BK15 result. The next data release for the collaboration is projected to directly proceed to BK17, adding data in 2016 and 2017 from both *Keck Array* and Bicep3.

In Section 4.8, we demonstrated Bicep3 reaches depth of 3.8 μK_{cmb}-arcmin over an effective area of 600 square degree with two season of data, this already exceeds the sensitivity of *Keck Array* in 95 GHz and is expected to have the same sensitivity in 150 GHz with additional data in 2018. By adding Bicep3 data, we project to improve the constraint on $\sigma(r) = 0.011$ compared to 0.020 in the current BK15 result.

Probing at 95 GHz with 2500 detectors allows us to better constrain synchrotron. The baseline analysis in BK15 shows $A_{\text{sync, 23}} = 1.0^{+1.2}_{-0.8} \mu K^2$, Figure 6.1 also indicates the detection of synchrotron from BK15 at low significance. With 2500 detectors at 95 GHz in Bicep3, we expect to improve the constraint on $A_{\text{sync, 23}}$. Figure 6.2 is a fisher matrix forecast by adding one year of Bicep3 data.

6.2 Bicep Array

The Bicep/*Keck Array* experiment produced the deepest CMB Polarization maps to date. Table 6.1 shows the progression of published sensitivity to r over time from CMB polarization [58][17][15][59][16][60][61][62][19][63].
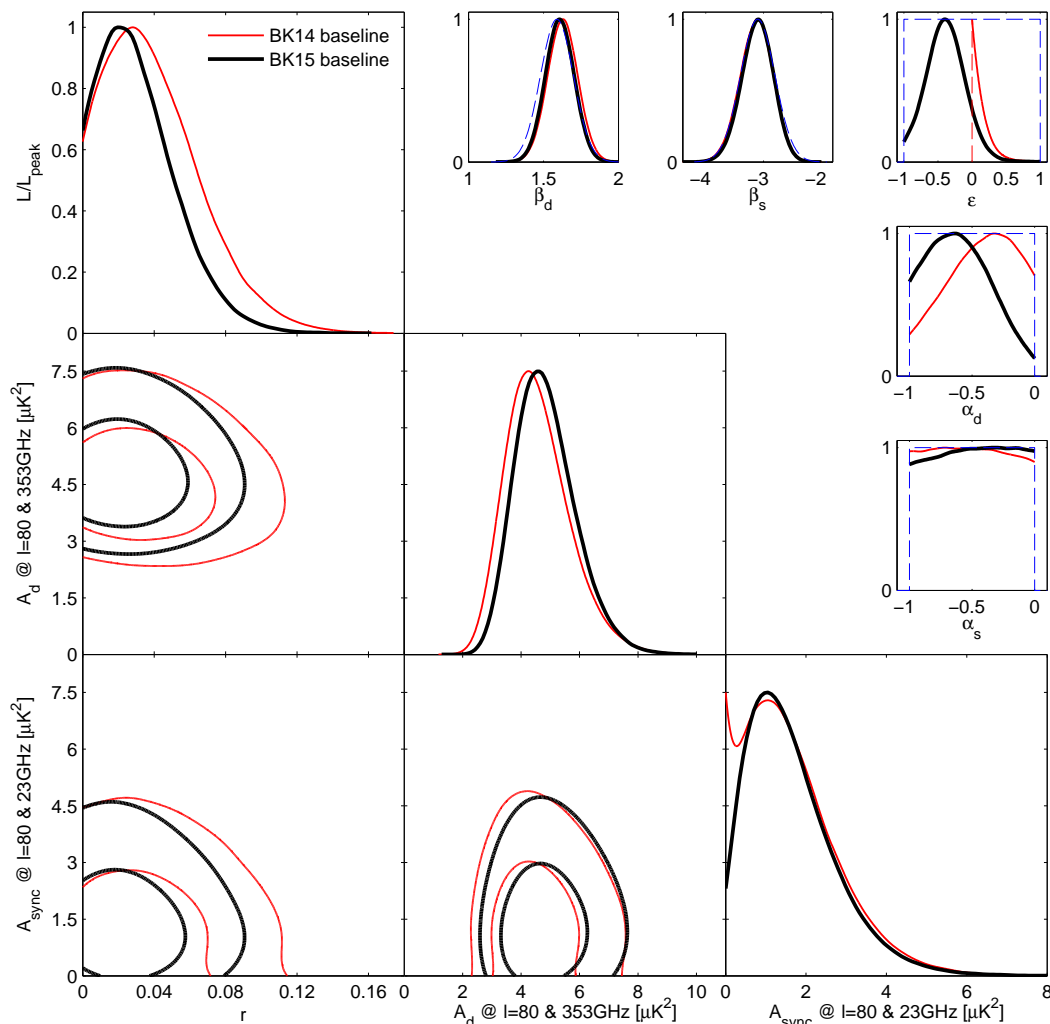
Figure 6.1:   BK15 likelihood analysis result, figure 4 in BK15

BICEP2 was the first of our receivers that used antenna-coupled transition-edge sensor (TES) bolometers. Five 25 cm aperture receivers, each similar to BICEP2, formed the *Keck Array*, and has been taking data since 2012 in a board range of frequencies. BICEP2 was replaced by BICEP3, a 0.5 m aperture receiver in 2015. Observing at 95 GHz, it has the same number of detectors as the entire *Keck Array*. This dissertation describes the design and performance of the instrument, demonstrates the increased field of view, angular resolution, and sensitivity compared to previous generation receiver.

We continue the same expansion concept used in BICEP2 to the *Keck Array*. BICEP ARRAY, which will make up by four copies of the BICEP3 design, each optimized for a single atmospheric window. Between the 2019 and 2020 observing season
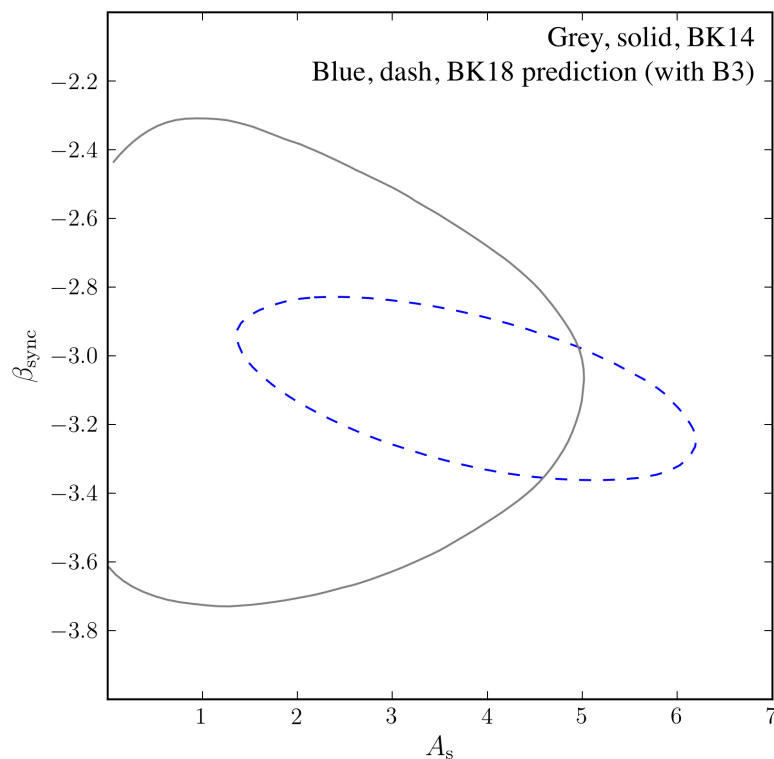
Figure 6.2: Constraints on synchrotron with BICEP3. Figure from Cheng Zheng.

Table 6.1: Published sensitivity of r to date from CMB Polarization. BICEP/*Keck Array* results set the lowest constrain for r

	date	arXiv	bands (GHz)	Inflation $\sigma(r)$
Dasi	Sep 2004	0409357	26...36	7.5
BICEP1	Jun 2009	0906.1181	100,150	0.28
WMAP 7yr	Jan 2010	1001.4538	30...60	1.1
Quiet-Q	Dec 2010	1012.3191	43	0.97
Quiet-W	Jun 2012	1207.5034	95	0.85
BICEP1 3yr	Oct 2013	1310.1422	100,150	0.25
BICEP2	Mar 2014	1403.3985	150	0.10
BK + *Planck* (BKP)	Feb 2015	1502.00612	150 (+30...353)	0.034
BK14 + WMAP	Oct 2015	1510.09217	150,95 (+23...353)	0.024
ABS	Jan 2018	1801.01218	150	0.7
BK15 + WP	Apr 2018		100,150,220	0.020

4 Receivers:
- 30, 40 GHz
- 95 GHz
- 150 GHz
- 220, 270 GHz
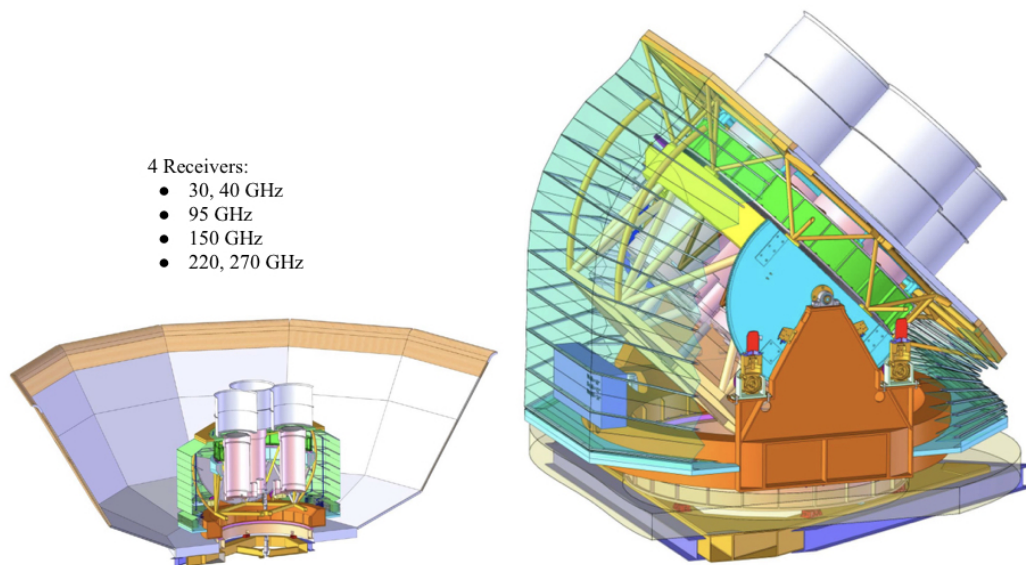
Figure 6.3: BICEP ARRAY Mount. This will replace the *Keck Array* mount in 2019, and house four BICEP ARRAY receivers from 30 to 270 GHz.

we will start replacing *Keck Array* with BICEP ARRAY. First, we will replace *Keck Array* telescope mount with BICEP ARRAY mount, a new machine able to carry four BICEP3 class receivers (Figure 6.3). At the sensitivity which we will be able to reach, the low frequency channels of WMAP and *Planck* will no longer be adequate to constrain synchrotron. Therefore, the first BICEP ARRAY receivers will be a new design operating in bands centered at 30 and 40 GHz, and on 2021 season onward the 95, 150 and 220/270 GHz receiver installed at the South Pole to complete the full deployment of BICEP ARRAY.

The parameters of the *Keck Array*, BICEP3 and BICEP ARRAY receivers are given in Table 6.2. The sensitivity estimation for BICEP ARRAY are based on the achieved survey weight from *Keck Array* and BICEP3.

Receiver overview

Each BICEP ARRAY receiver is housed in a custom-designed vacuum cryostat 2.1 m tall and 0.9 m in diameter (not including the MCE readout electronic and pulse-tube cooler. This design is modeled heavily on BICEP3. Figure 6.4 is a CAD cross-section of the receiver. The vacuum jacket and the 50 K stages are constructed with a short base stage, and the main section tube for simple machining. The top of the vacuum jacket is capped by a HDPE vacuum window and a stack of Zotefoam IR filters behind it. An infrared-absorptive alimina filter is installed at the top of the 50 K

Receiver Observing Band (GHz)	Nominal Number of Detectors	Nominal Single Detector NET ($\mu K_{cmb}\sqrt{s}$)	Beam FWHM (arcmin)	Survey Weight Per Year ($(\mu K_{cmb})^{-2}$ yr^{-1})
Keck Array				
95	**288**	288	**43**	**24,000**
150	**512**	313	**30**	**30,000**
220	**512**	837	**21**	**2,000**
270	512	1310	17	800
Bicep3				
95	**2560**	288	**24**	213,000
Bicep Array				
30	192	221	76	19,500
40	300	301	57	20,500
95	3456	288	24	287,000
150	7776	313	15	453,000
220	8112	837	11	37,000
270	13068	1310	9	15,000

Table 6.2: Receiver parameters as used in sensitivity projections. Boldface numbers are actual/achieved quantities for existing receivers. The remaining values in the survey weight column are scaled from the achieved survey weights using only the ratio of the number of detectors, plus, if necessary to change frequency, the ratio of nominal NET values squared.

stage.

The 4 K stage is sectioned into two lengthwise segments for ease of access; the top optic section houses the optical elements, including alumina lenses, and nylon infrared filter. The lower camera section houses the sub-kelvin cryogenic system, SQUID readout electronic, and the sub-kelvin focal plane with the associated thermo-mechanical structure.

The 50 K and 4 K volumes are supported by G-10 trusses, providing robust structural support while maintaining low thermal conductivity between temperature stages. The sub-Kelvin structures are supported by carbon fiber trusses for its high ratio of stiffness to thermal conductivity at the corresponding temperature.

Thermal Architecture

Bicep Array's thermal architecture minimizes non-CMB loading on the detectors. Most of the optical elements are cooled to 4 K or below. The 50 K and 4 K stages are heat sunk to the first and second stages of a Cryomech PT-415 cooler, with cooling
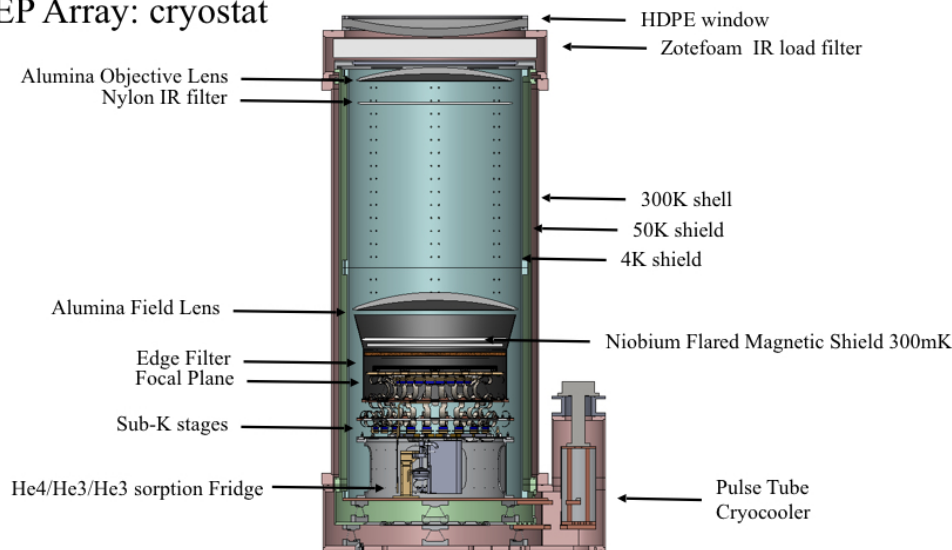
Figure 6.4: BICEP ARRAY receiver cutaway.

capacity of 40 W and 1.5 W, respectively.

The large window aperture presents ~110 W of infrared loading going into the receiver. Following the lesson learned in BICEP3, we use a combination of Zotefoam filters, alumina optics and a nylon filter to reduce sky infrared loading to an acceptable level for the sub-Kelvin stages to function. Combining with actual measurements from BICEP3and thermal model, the total calculated loading on the 50 K and 4 K stages are estimated about 21 W and 0.38 W, respectively. This suggests it will have base temperature of 34 K and 3.1 K at these stages.

Sub-Kelvin cooling for the detectors is provided by a three-stage helium sorption fridge from CEA Grenoble at 2 K (4He stage), 340 mK (intercooler), and 250 mK (ultracooler), with cooling capacity of 230 μW, 70 μW, and 15 μW receptively (Figure 6.5). Detector modules and the focal plane are heat sunk to the ultracooler via a flexible high-purity copper-foil heat strap and a low pass stainless steel filter, and estimated with 0.2 μW on the ultracooler stage (Table 6.3).

Thermal monitoring for the cryostat is done using calibrated diodes and resistance thermometers (cernox) at the radiation shields, critical cryogenic junctions, and some of the optical elements. The focal plane temperature is maintained at a stable temperature by passive and active filtering similar to BICEP3. Active control is implemented in a feedback loop using Ge NTD thermometers and resistive heater. Figure 6.7 shows the housekeeping layout in BICEP ARRAY.
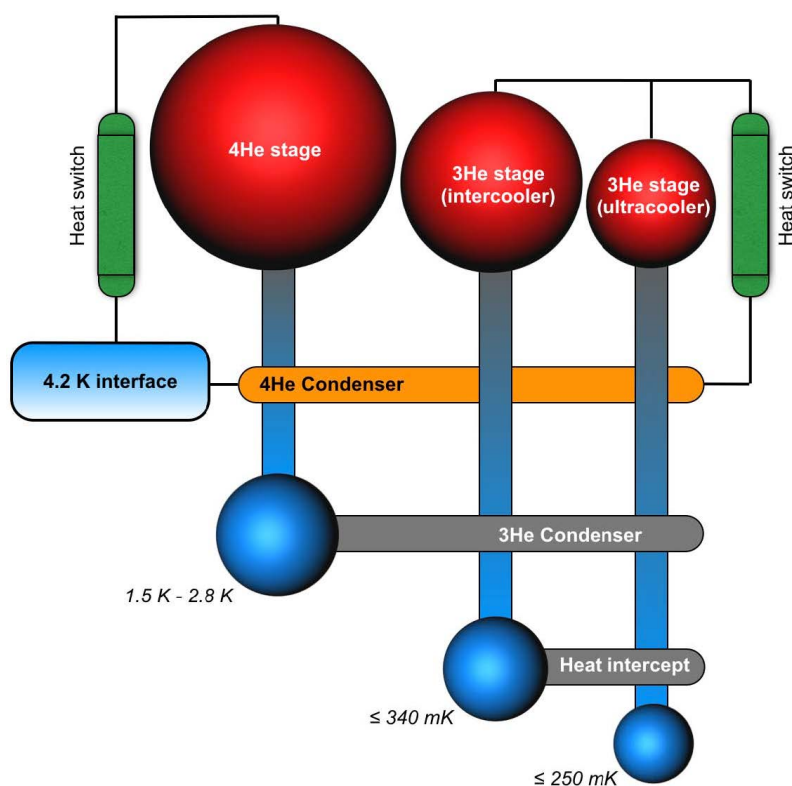
Figure 6.5: Schematic of a three stages 3He sorption fridge. It has 230, 70 and 15 μW of cooling power at the 2 K, 340 mK and 250 mK stage, respectively. (Credit: CEA Grenoble)

Table 6.3: Sub-Kelvin loading for BICEP ARRAY. This calculation is based on the maximizing cable counts for high frequencies receiver, the loading is expected to be smaller with less readout cables for low frequency receiver.

	2 K (μW)	340 mK (μW)	230 mK (nW)
16 NbTi cables	110.7	27.7	99.6
4 Manganin cables	3.2	0.9	3.5
Cernox cables	11.0	2.1	3.0
Heater cables	4.6	0.8	2.3
Carbon fiber trusses	44.0	16.9	47.1
Aluminize mylar shield	52.9	23.4	97.8
Total	226.5	71.7	253.2
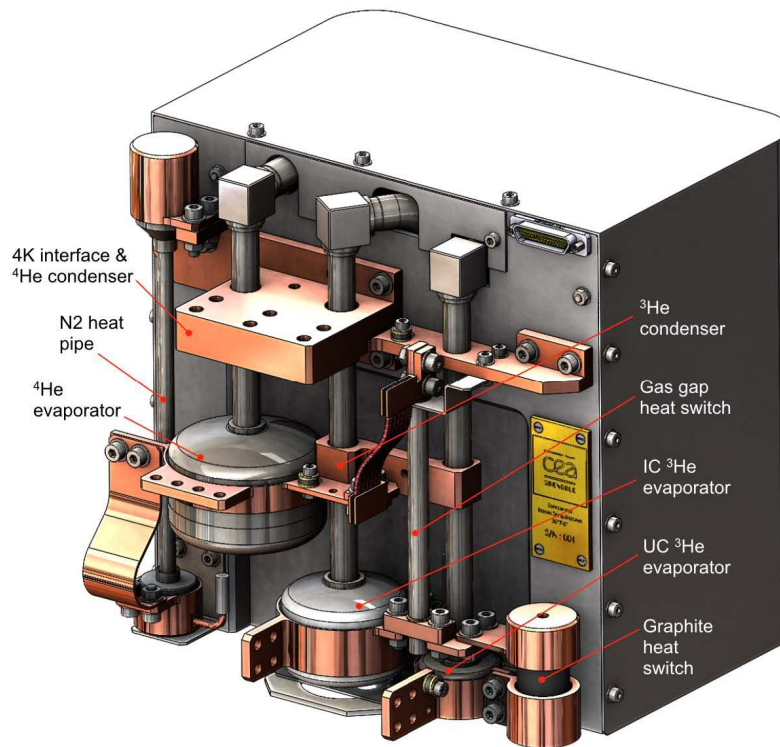
Figure 6.6: CAD model of the BICEP ARRAY fridge. Each stage is equipped with removable heat switch sunk at 4 K for accelerated initial cool down. (Credit: CEA Grenoble)

Optics

Following the same design concept in BICEP/*Keck Array* experiment, most of the optical elements in BICEP ARRAY are cooled to 4 K to minimize loading on the detectors. The telescope is a simple two-lens, diffraction-limited, on-axis telecentric refractor to keep aberration and distortions subdominant. It has a mean f-ratio of $f/1.6$. The alumina lenses are 650 mm in diameter with clear aperture of 630 mm. The maximum thickness of each lens is 68.8 mm, figure 6.8 is a optical diagram of the 35 GHz design. The 4 K space between the objective and the field lens are covered in epoxy-encapsulated Eccosorb HR-10 microwave absorber to suppress far-sidelobes reflection. The same Eccosorb is also used to define the optical stop for the system, located behind the objective lens.

Simulation shows the beams width $\sigma \sim 9'$, with the field of view of 29.6 degree, given the similarly to the BICEP3 design, we expect the actual result to be well behaved compared to the design model.

Figure 6.7: BICEP ARRAY housekeeping layout.

Figure 6.8: BICEP ARRAY optical diagram.

Focal plane and detector module

Similar to BICEP3, the sub-Kelvin structure is located on top of the 4 K base plate, above the sorption fridge. It is separated into three thermal, wedding cake shape stages at 2 K, 350 mK, and 260 mK. Each stage provides radiative shielding and room for cables heat sinking to the respective cooler stages, allowing low loading environment for the focal plane and detectors. The copper focal plane is mounted at the ultracool stage, separated by a low pass stainless steel filter and carbon fiber trusses.

The housekeeping electronics and second stage SQUID readout electronic are housed at the 4 K base plate. Modular readout electronic circuit allow the same design to be use in the 30/40 GHz, 95 GHz, and 150 GHz receiver. A single circuit board is mounted underneath the copper focal plane, gathering all the readout cabling and distributing to the corresponding detector module.

Twelve detector modules are tiled onto the focal plane, each containing 32 to 2178 detectors, depending on its observation frequencies (Table 6.2). The module is based on the design from BICEP3 [33], except the detector is fabricated on a 6" silicon wafer, compared to previously 3" wafer for better packing density (Figure 6.9). The first stage SQUID readout multiplexing chips are housed on a silicon/ alumina nitride circuit board inside the module. Figure 6.10 shows the exploded view of the module design.

Interaction between the edge antenna and the metal frame causes differential ellipticity, resulting in potential T to B leakage in the polarization data. We designed corrugated walls to minimize this effect [64]. The 30/40 GHz receiver uses a double corrugations to eliminates the differential ellipticity caused by the metal frame over 57% bandwidth, from 25 GHz to 45 GHz.

Extensive finite element simulations are done on the truss structure in BICEP ARRAY to validate the vibrational resonances. The minimum resonance frequency from carbon fiber trusses is 55 Hz, a maximum displacement of less than 70 μm at the focal plane under 90 degree gravity load, and first buckling mode at 9 times the nominal load.

BICEP ARRAY (up to 150 GHz) continues to use time-domain multiplexed (TDM) readout of the TES bolometers, via SQUID 11-row MUX chips developed by NIST, in order to reduce the total number of lines entering the cryostat and their associated heat load. Details of the multiplexing design are found in [31][33]. Table 6.4 shows
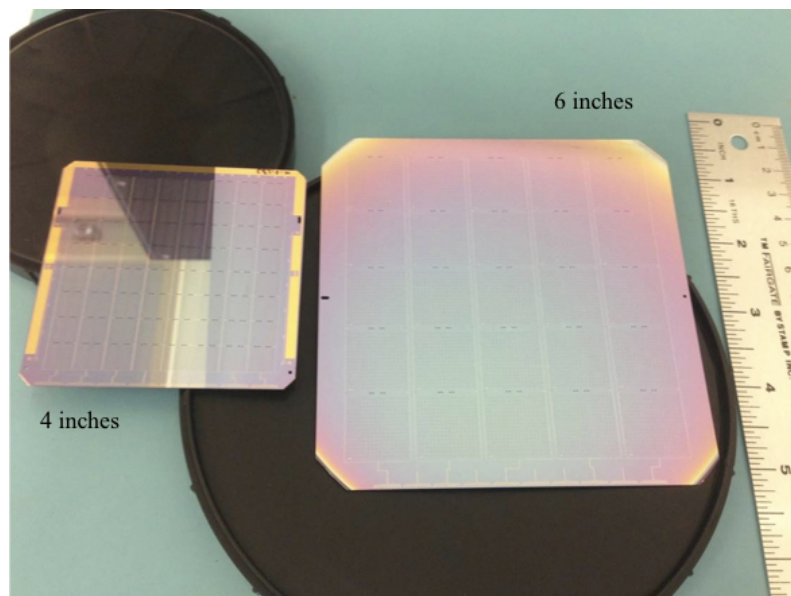
Figure 6.9: 4" and 6" detector wafer used in Bicep3 and Bicep Array, respectively. The larger wafer allows even better packing density. The 95 GHz Bicep Array receiver will house 4000+ detectors compare to 2560 detectors in Bicep3.
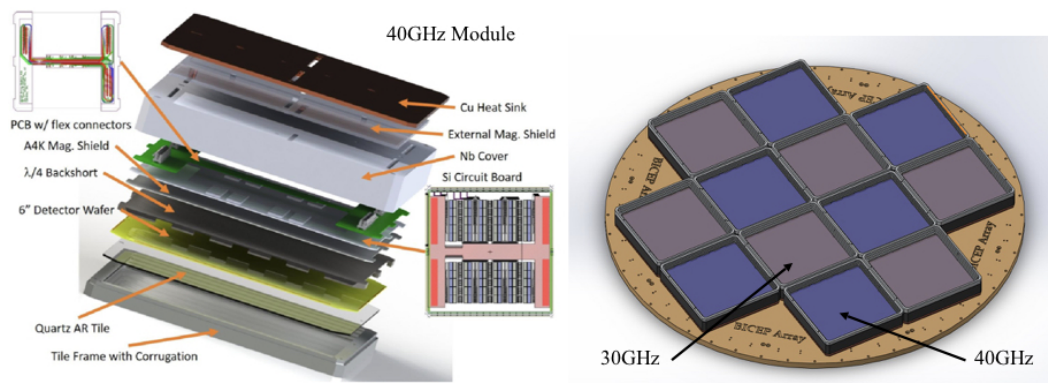
Figure 6.10: Left: An exploded view of the Bicep Array module. The design is based on Bicep3 but utilizes bigger detector wafer. Right: A CAD model of the 30/40 GHz focal plane layout. The receiver has six 30 GHz and six 40 GHz module layout in a checker board pattern.

Table 6.4: Multiplexing schematic for Bicep Array in each receiver

Frequency	30/40 GHz	95 GHz	150 GHz
# Tiles	12	12	12
# Detectors	192 + 300	3456	7776
# Det/Tile	32 + 50	288	648
# MUX chips/ Tile	6	28	64
# MCE	1	3	6
# Columns/MCE	24	28	32
# Rows	33	43	42

Table 6.5: Magnetic shield in Bicep Array

Parts	Axial Residual Flux	Transverse Residual Flux
50K and 4K shield	0.24%	0.52%
Detector module	0.12%	0.20%
Final shielding	0.0003%	0.001%

the multiplexing layout in Bicep Array in different frequencies.

Magnetic shielding

Bicep Array's magnetic shield architecture protects the SQUID readout out system from external magnetic field. The configuration is designed using COMSOL Multiphysics[1], which allowed us to simulate the Meissner behavior of a superconducting material.

First stage of shielding is done by a 1 mm thick high-μ A4K sheet wrapped around the 50 K stage, and a 2 mm thick niobium flare cup on the 350 mK stage. This provides a 200 plus shielding factor (Figure 6.11).

The detector and first stage SQUIDs are further protected by the module housing. A combination of niobium box and a A4K sheet placed 0.5 mm underneath the MUX chip provides an additional 500 of shielding factor inside the detector module.

6.3 Conclusion

We often describe the attempt to measure the *B*-mode polarization from inflationary gravitational waves as a "wild goose chase", as we don't have a lower bound of the

50 K high-μ A4K shield

300 mK Niobium superconductive flared cup

Niobium 2mm thick flared cup

Slotted holes on the
rim with 2" overlay

Niobium 4mm RF shielding retainer

Niobium 2mm thick layer
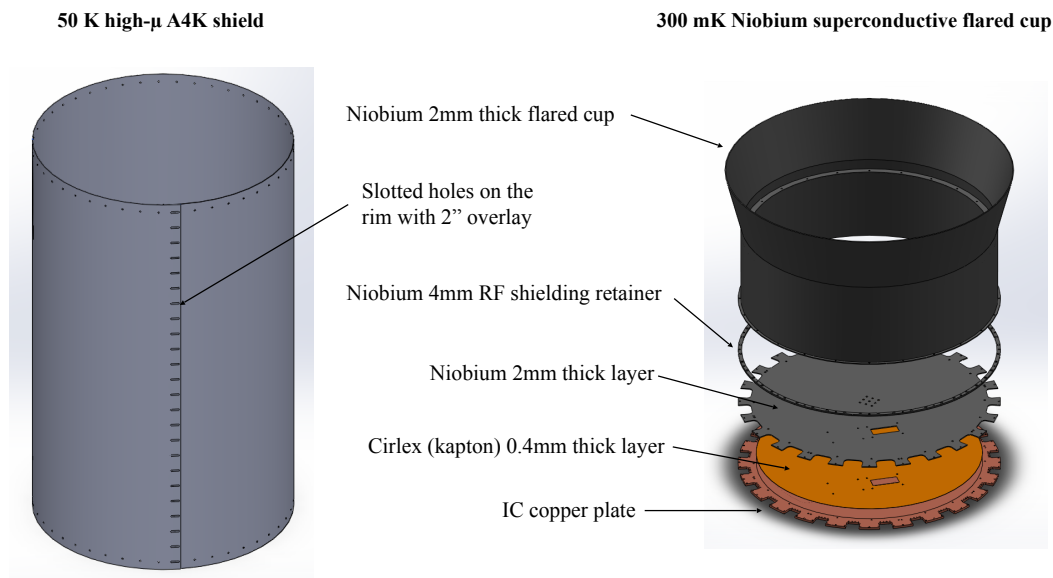
Cirlex (kapton) 0.4mm thick layer

IC copper plate

Figure 6.11: First stage BICEP ARRAY magnetic shield.

tensor-to-scalar ratio r, or absolute confidence of its existence. However, most of the inflationary model generally predicts a detectable level of r above approximately 0.01. A measurement of primordial B-modes allows us to probe the early Universe, $\sim 10^{-35}$s after the Big Bang. The amplitude of the signature determines the energy scale of inflation, and potentially further increases our understanding of quantum gravity. Although, pushing the upper limit without a detection would also be significant.

The BICEP experiment's singular goal is to detect this unique primordial signature. Over the years, every telescope in this experiment has been the leader in the field. BICEP1, deployed in 2006, set the upper limit on inflation from B-modes at $r < 0.7$ at 95% confidence. BICEP2 detected a 5σ excess of B-mode polarization at degree angular scale in 2014; and the *Keck Array* current leading limit on $r < 0.06$ at 95% confidence by adding combining the multi-frequencies receivers data.

This dissertation describes the newest member in this experiment, BICEP3; a 550 mm aperture refracting telescope with 2500 detectors at 95 GHz. With a throughput 15 times higher than a *Keck Array* style receiver in the same frequency, it achieved
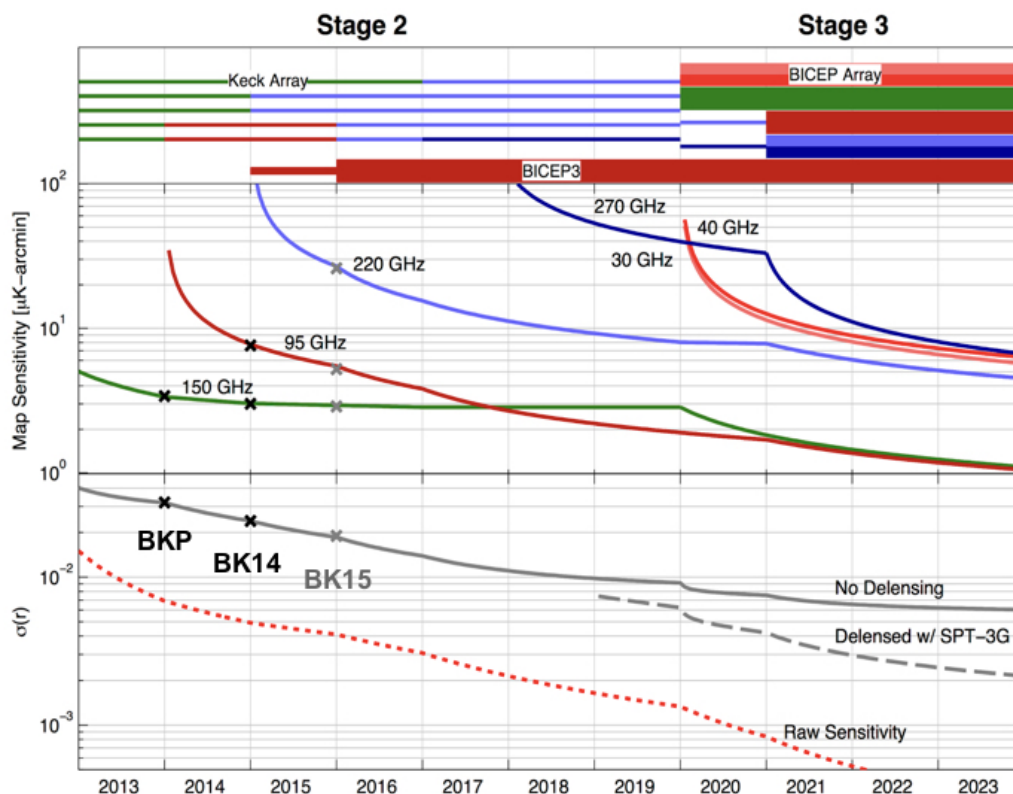
Figure 6.12: Projected sensitivity of the ongoing and planned BICEP experiment. Top: Different telescope of the experiment at various frequencies, from 30/40 GHz to 270 GHz. Middle: Map depth at each frequency as a function of time. Bottom: Sensitivity to *r* with different de-lensing efficiency and raw sensitivity.

instantaneously sensitivity at $7.3\mu K_{cmb}\sqrt{s}$, and reaches depth of 3.8 μK_{cmb}-arcmin after two years of science observation.

As expected, *Keck Array* will replace BICEP ARRAY beginning of fall of 2019. BICEP ARRAY is made up by four BICEP3 class receivers in a board range of frequencies; allowing us to cleanly separate foreground contamination from CMB, and achieve sensitivity of $\sigma(r) < 0.004$ by the end of 2023 (Figure 6.12). This will detect evidence for inflationary gravitational waves, or allow us to look into new and unknown physics.

BIBLIOGRAPHY

[1] T. Misner and K. Thorne, *Wheeler.: 1973, gravitation*, 1973.

[2] P. de Bernardis, P. A. Ade, J. Bock, J. Bond, J. Borrill, A. Boscaleri, K. Coble, B. Crill, G. De Gasperis, P. Farese, *et al.*, "A flat universe from high-resolution maps of the cosmic microwave background radiation," *Nature*, vol. 404, no. 6781, p. 955, 2000.

[3] P. A. Ade, N. Aghanim, M. Arnaud, M. Ashdown, J. Aumont, C. Baccigalupi, A. Banday, R. Barreiro, J. Bartlett, N. Bartolo, *et al.*, "Planck 2015 results-xiii. cosmological parameters," *Astronomy & Astrophysics*, vol. 594, A13, 2016.

[4] S. M. Carroll, *Spacetime and geometry. An introduction to general relativity*. 2004.

[5] J. C. Mather, E. Cheng, D. A. Cottingham, R. Eplee Jr, D. J. Fixsen, T. Hewagama, R. Isaacman, K. Jensen, S. S. Meyer, P. D. Noerdlinger, *et al.*, "Measurement of the cosmic microwave background spectrum by the cobe firas instrument," *The Astrophysical Journal*, vol. 420, pp. 439–444, 1994.

[6] R. Adam, P. Ade, N. Aghanim, Y. Akrami, M. Alves, F. Argüeso, M. Arnaud, F. Arroja, M. Ashdown, J. Aumont, *et al.*, "Planck 2015 results-i. overview of products and scientific results," *Astronomy & Astrophysics*, vol. 594, A1, 2016.

[7] A. H. Guth, "Inflationary universe: A possible solution to the horizon and flatness problems," *Physical Review D*, vol. 23, no. 2, p. 347, 1981.

[8] M. Kamionkowski and E. D. Kovetz, "The quest for b modes from inflationary gravitational waves," *Annual Review of Astronomy and Astrophysics*, vol. 54, pp. 227–269, 2016.

[9] D. Baumann, "Tasi lectures on inflation," *arXiv preprint arXiv:0907.5424*, 2009.

[10] S. Weinberg, "Effective field theory for inflation," *Physical Review D*, vol. 77, no. 12, p. 123 541, 2008.

[11] W. Hu and S. Dodelson, "Cosmic microwave background anisotropies," *Annual Review of Astronomy and Astrophysics*, vol. 40, no. 1, pp. 171–216, 2002.

[12] D. Hanson, S. Hoover, A. Crites, P. Ade, K. Aird, J. Austermann, J. Beall, A. Bender, B. Benson, L. Bleem, *et al.*, "Detection of b-mode polarization in the cosmic microwave background with data from the south pole telescope," *Physical Review Letters*, vol. 111, no. 14, p. 141 301, 2013.

[13] R. Keisler, S. Hoover, N. Harrington, J. Henning, P. Ade, K. Aird, J. Austermann, J. Beall, A. Bender, B. Benson, *et al.*, "Measurements of sub-degree b-mode polarization in the cosmic microwave background from 100 square degrees of sptpol data," *The Astrophysical Journal*, vol. 807, no. 2, p. 151, 2015.

[14] P. Ade, Y. Akiba, A. Anthony, K. Arnold, M. Atlas, D. Barron, D. Boettger, J. Borrill, S. Chapman, Y. Chinone, *et al.*, "A measurement of the cosmic microwave background b-mode polarization power spectrum at sub-degree scales with polarbear," *The Astrophysical Journal*, vol. 794, no. 2, p. 171, 2014.

[15] D. Barkats, R. Aikin, C. Bischoff, I. Buder, J. Kaufman, B. Keating, J. M. Kovac, M. Su, P. Ade, J. Battle, *et al.*, "Degree-scale cosmic microwave background polarization measurements from three years of bicep1 data," *The Astrophysical Journal*, vol. 783, no. 2, p. 67, 2014.

[16] P. A. Ade, R. W. Aikin, D. Barkats, S. J. Benton, C. A. Bischoff, J. J. Bock, J. A. Brevik, I. Buder, E. Bullock, C. D. Dowell, *et al.*, "Detection of b-mode polarization at degree angular scales by bicep2," *Physical Review Letters*, vol. 112, no. 24, p. 241 101, 2014.

[17] P. A. Ade, N. Aghanim, Z. Ahmed, R. Aikin, K. D. Alexander, M. Arnaud, J. Aumont, C. Baccigalupi, A. J. Banday, D. Barkats, *et al.*, "Joint analysis of bicep2/keck array and planck data," *Physical review letters*, vol. 114, no. 10, p. 101 301, 2015.

[18] P. A. Ade, R. Aikin, M. Amiri, D. Barkats, S. Benton, C. A. Bischoff, J. Bock, J. Brevik, I. Buder, E. Bullock, *et al.*, "Bicep2. ii. experiment and three-year data set," *The Astrophysical Journal*, vol. 792, no. 1, p. 62, 2014.

[19] P. Ade *et al.*, "Improved constraints on cosmology and foregrounds from bicep2 and keck array cosmic microwave background data with inclusion of 95 ghz band," *Phys. Rev. Lett*, vol. 116, p. 031 302, 2016.

[20] R. Ogburn, P. Ade, R. Aikin, M. Amiri, S. Benton, C. A. Bischoff, J. Bock, J. Bonetti, J. Brevik, E. Bullock, *et al.*, "Bicep2 and keck array operational overview and status of observations," in *Millimeter, Submillimeter, and Far-Infrared Detectors and Instrumentation for Astronomy VI*, International Society for Optics and Photonics, vol. 8452, 2012, 84521A.

[21] Z. Staniszewski, R. Aikin, M. Amiri, S. Benton, C. Bischoff, J. Bock, J. Bonetti, J. Brevik, B. Burger, C. Dowell, *et al.*, "The keck array: A multi camera cmb polarimeter at the south pole," *Journal of Low Temperature Physics*, vol. 167, no. 5-6, pp. 827–833, 2012.

[22] I. Buder, P. Ade, Z. Ahmed, R. Aikin, K. Alexander, M. Amiri, D. Barkats, S. Benton, C. Bischoff, J. Bock, *et al.*, "Bicep2 and keck array: Upgrades and improved beam characterization," in *Millimeter, Submillimeter, and Far-Infrared*

Detectors and Instrumentation for Astronomy VII, International Society for Optics and Photonics, vol. 9153, 2014, p. 915 312.

[23] L. Knox, "Determination of inflationary observables by cosmic microwave background anisotropy experiments," *Physical Review D*, vol. 52, no. 8, p. 4307, 1995.

[24] P. A. Ade, Z. Ahmed, R. Aikin, K. D. Alexander, D. Barkats, S. Benton, C. A. Bischoff, J. Bock, J. Brevik, I. Buder, *et al.*, "Bicep2/keck array v: Measurements of b-mode polarization at degree angular scales and 150 ghz by the keck array," *The Astrophysical Journal*, vol. 811, no. 2, p. 126, 2015.

[25] P. A. Ade, G. Pisano, C. Tucker, and S. Weaver, "A review of metal mesh filters," in *Millimeter and Submillimeter Detectors and Instrumentation for Astronomy III*, International Society for Optics and Photonics, vol. 6275, 2006, 62750U.

[26] Z. Ahmed, J. Grayson, K. Thompson, C.-L. Kuo, G. Brooks, and T. Pothoven, "Large-area reflective infrared filters for millimeter/sub-mm telescopes," *Journal of Low Temperature Physics*, vol. 176, no. 5-6, pp. 835–840, 2014.

[27] Z. Ahmed, M. Amiri, S. Benton, J. Bock, R. Bowens-Rubin, I. Buder, E. Bullock, J. Connors, J. Filippini, J. Grayson, *et al.*, "Bicep3: A 95ghz refracting telescope for degree-scale cmb polarization," in *Millimeter, Submillimeter, and Far-Infrared Detectors and Instrumentation for Astronomy VII*, International Society for Optics and Photonics, vol. 9153, 2014, 91531N.

[28] D. Rosen, A. Suzuki, B. Keating, W. Krantz, A. T. Lee, E. Quealy, P. L. Richards, P. Siritanasak, and W. Walker, "Epoxy-based broadband antireflection coating for millimeter-wave optics," *Applied optics*, vol. 52, no. 33, pp. 8102–8105, 2013.

[29] C. E. Tucker and P. A. Ade, "Thermal filtering for large aperture cryogenic detector arrays," in *Millimeter and Submillimeter Detectors and Instrumentation for Astronomy III*, International Society for Optics and Photonics, vol. 6275, 2006, 62750T.

[30] W. Wu, P. Ade, Z. Ahmed, K. Alexander, M. Amiri, D. Barkats, S. Benton, C. Bischoff, J. Bock, R. Bowens-Rubin, *et al.*, "Initial performance of bicep3: A degree angular scale 95 ghz band polarimeter," *Journal of Low Temperature Physics*, vol. 184, no. 3-4, pp. 765–771, 2016.

[31] J. Grayson, P. Ade, Z. Ahmed, K. D. Alexander, M. Amiri, D. Barkats, S. Benton, C. A. Bischoff, J. Bock, H. Boenish, *et al.*, "Bicep3 performance overview and planned keck array upgrade," in *Millimeter, Submillimeter, and Far-Infrared Detectors and Instrumentation for Astronomy VIII*, International Society for Optics and Photonics, vol. 9914, 2016, 99140S.

[32] D. V. Wiebe, *BLAST: A balloon-borne, large-aperture, submillimetre telescope*, 04. 2008, vol. 71.

[33] H. Hui, P. Ade, Z. Ahmed, K. D. Alexander, M. Amiri, D. Barkats, S. Benton, C. A. Bischoff, J. Bock, H. Boenish, *et al.*, "Bicep3 focal plane design and detector performance," in *Millimeter, Submillimeter, and Far-Infrared Detectors and Instrumentation for Astronomy VIII*, International Society for Optics and Photonics, vol. 9914, 2016, 99140T.

[34] B. Benson, P. Ade, Z. Ahmed, S. Allen, K. Arnold, J. Austermann, A. Bender, L. Bleem, J. Carlstrom, C. Chang, *et al.*, "Spt-3g: A next-generation cosmic microwave background polarization experiment on the south pole telescope," in *Millimeter, Submillimeter, and Far-Infrared Detectors and Instrumentation for Astronomy VII*, International Society for Optics and Photonics, vol. 9153, 2014, 91531P.

[35] P. A. Ade, R. Aikin, D. Barkats, S. Benton, C. A. Bischoff, J. Bock, K. Bradford, J. Brevik, I. Buder, E. Bullock, *et al.*, "Bicep2/keck array. iv. optical characterization and performance of the bicep2 and keck array experiments," *The Astrophysical Journal*, vol. 806, no. 2, p. 206, 2015.

[36] R. O'Brient, P. Ade, Z. Ahmed, R. Aikin, M. Amiri, S. Benton, C. Bischoff, J. Bock, J. Bonetti, J. Brevik, *et al.*, "Antenna-coupled tes bolometers for the keck array, spider, and polar-1," in *Millimeter, Submillimeter, and Far-Infrared Detectors and Instrumentation for Astronomy VI*, International Society for Optics and Photonics, vol. 8452, 2012, 84521G.

[37] J. Bonetti, A. Turner, J. Bock, J. Brevik, P. Day, J. Filippini, S. Golwala, W. Holmes, W. Jones, M. Kenyon, *et al.*, "Characterization and fabrication of the tes arrays for the spider, keck and bicep2 cmb polarimeters," *Journal of Low Temperature Physics*, vol. 167, no. 3-4, pp. 146–151, 2012.

[38] A. Orlando, R. Aikin, M. Amiri, J. Bock, J. Bonetti, J. Brevik, B. Burger, G. Chattopadthyay, P. Day, J. Filippini, *et al.*, "Antenna-coupled tes bolometer arrays for bicep2/keck and spider," in *Millimeter, Submillimeter, and Far-Infrared Detectors and Instrumentation for Astronomy V*, International Society for Optics and Photonics, vol. 7741, 2010, 77410H.

[39] J. Bonetti, A. Turner, M. Kenyon, A. Orlando, J. Brevik, A. Trangsrud, R. Sudiwala, H. Leduc, H. Nguyen, P. Day, *et al.*, "Microfabrication and device parameter testing of the focal plane arrays for the spider and bicep2/keck cmb polarimeters," in *AIP Conference Proceedings*, AIP, vol. 1185, 2009, pp. 367–370.

[40] P. A. Ade, R. Aikin, M. Amiri, D. Barkats, S. Benton, C. A. Bischoff, J. Bock, J. Bonetti, J. Brevik, I. Buder, *et al.*, "Antenna-coupled tes bolometers used in bicep2, keck array, and spider," *The Astrophysical Journal*, vol. 812, no. 2, p. 176, 2015.

[41] K. D. Irwin and G. C. Hilton, "Transition-edge sensors," in *Cryogenic particle detection*, Springer, 2005, pp. 63–150.

[42] S. Kernasovskiy, "Measuring the polarization of the cosmic microwave background with the keck array and bicep2," PhD thesis, Stanford University, 2014.

[43] K. D. Irwin, "Squid multiplexers for transition-edge sensors," *Physica C: Superconductivity*, vol. 368, no. 1-4, pp. 203–210, 2002.

[44] E. Battistelli, M. Amiri, B. Burger, M. Halpern, S. Knotek, M. Ellis, X. Gao, D. Kelly, M. Macintosh, K. Irwin, *et al.*, "Functional description of readout electronics for time-domain multiplexed bolometers for millimeter and sub-millimeter astronomy," *Journal of Low Temperature Physics*, vol. 151, no. 3-4, pp. 908–914, 2008.

[45] K. Karkare, P. A. Ade, Z. Ahmed, R. Aikin, K. Alexander, M. Amiri, D. Barkats, S. Benton, C. Bischoff, J. Bock, *et al.*, "Keck array and bicep3: Spectral characterization of 5000+ detectors," in *Millimeter, Submillimeter, and Far-Infrared Detectors and Instrumentation for Astronomy VII*, International Society for Optics and Photonics, vol. 9153, 2014, 91533B.

[46] J. A. Grayson, "The bicep3 millimeter-wave polarimeter: Measuring the cosmic microwave background from the south pole," PhD thesis, Stanford University, 2016.

[47] S. Kernasovskiy, P. Ade, R. Aikin, M. Amiri, S. Benton, C. Bischoff, J. Bock, J. Bonetti, J. Brevik, B. Burger, *et al.*, "Optimization and sensitivity of the keck array," in *Millimeter, Submillimeter, and Far-Infrared Detectors and Instrumentation for Astronomy VI*, International Society for Optics and Photonics, vol. 8452, 2012, 84521B.

[48] J. Brevik, R. Aikin, M. Amiri, S. Benton, J. Bock, J. Bonetti, B. Burger, C. Dowell, L. Duband, J. Filippini, *et al.*, "Initial performance of the bicep2 antenna-coupled superconducting bolometers at the south pole," in *Millimeter, Submillimeter, and Far-Infrared Detectors and Instrumentation for Astronomy V*, International Society for Optics and Photonics, vol. 7741, 2010, 77411H.

[49] K. S. Karkare, P. Ade, Z. Ahmed, K. D. Alexander, M. Amiri, D. Barkats, S. Benton, C. A. Bischoff, J. Bock, H. Boenish, *et al.*, "Optical characterization of the bicep3 cmb polarimeter at the south pole," in *Millimeter, Submillimeter, and Far-Infrared Detectors and Instrumentation for Astronomy VIII*, International Society for Optics and Photonics, vol. 9914, 2016, p. 991 430.

[50] K. S. Karkare, B. A. Collaboration, *et al.*, "Multifrequency beam characterization and systematics for the keck array, bicep3, and future cmb polarization experiments," in *American Astronomical Society Meeting Abstracts*, vol. 229, 2017.

[51] P. Ade, R. Aikin, D. Barkats, S. Benton, C. A. Bischoff, J. Bock, J. Brevik, I. Buder, E. Bullock, C. Dowell, *et al.*, "Bicep2. iii. instrumental systematics," *The Astrophysical Journal*, vol. 814, no. 2, p. 110, 2015.

[52] P. Ade, Z. Ahmed, R. Aikin, K. D. Alexander, D. Barkats, S. Benton, C. A. Bischoff, J. Bock, R. Bowens-Rubin, J. Brevik, *et al.*, "Bicep2/keck array. vii. matrix based e/b separation applied to bicep2 and the keck array," *The Astrophysical Journal*, vol. 825, no. 1, p. 66, 2016.

[53] J. Tolan, "Testing inflationary cosmology with bicep2 and the keck array," PhD thesis, Stanford University, 2014.

[54] M. Tegmark, "How to measure cmb power spectra without losing information," *Physical Review D*, vol. 55, no. 10, p. 5895, 1997.

[55] E. Hivon, K. M. Górski, C. B. Netterfield, B. P. Crill, S. Prunet, and F. Hansen, "Master of the cosmic microwave background anisotropy power spectrum: A fast method for statistical analysis of large and complex cosmic microwave background data sets," *The Astrophysical Journal*, vol. 567, no. 1, p. 2, 2002.

[56] R. W. Aikin, *Testing inflationary cosmology with the BICEP1 and BICEP2 experiments*. California Institute of Technology, 2013.

[57] K. M. Smith, "Pseudo-cl estimators which do not mix e and b modes," *Physical Review D*, vol. 74, no. 8, p. 083 002, 2006.

[58] J. M. Kovac, E. Leitch, C. Pryke, J. Carlstrom, N. Halverson, and W. Holzapfel, "Detection of polarization in the cosmic microwave background using dasi," *Nature*, vol. 420, no. 6917, p. 772, 2002.

[59] H. C. Chiang, P. A. Ade, D. Barkats, J. O. Battle, E. M. Bierman, J. J. Bock, C. D. Dowell, L. Duband, E. F. Hivon, W. L. Holzapfel, *et al.*, "Measurement of cosmic microwave background polarization power spectra from two years of bicep data," *The Astrophysical Journal*, vol. 711, no. 2, p. 1123, 2010.

[60] D. Araujo, C. Bischoff, A. Brizius, I. Buder, Y. Chinone, K. Cleary, R. Dumoulin, A. Kusaka, R. Monsalve, *et al.*, "Second season quiet observations: Measurements of the cosmic microwave background polarization power spectrum at 95 ghz," *The Astrophysical Journal*, vol. 760, no. 2, p. 145, 2012.

[61] C. Bischoff, A. Brizius, I. Buder, Y. Chinone, K. Cleary, R. Dumoulin, A. Kusaka, R. Monsalve, L. Newburgh, *et al.*, "First season quiet observations: Measurements of cosmic microwave background polarization power spectra at 43 ghz in the multipole range 25 to 475," *The Astrophysical Journal*, vol. 741, no. 2, p. 111, 2011.

[62] N. Jarosik, C. Bennett, J. Dunkley, B. Gold, M. Greason, M. Halpern, R. Hill, G. Hinshaw, A. Kogut, E. Komatsu, *et al.*, "Seven-year wilkinson microwave anisotropy probe (wmap) observations: Sky maps, systematic errors, and basic results," *The Astrophysical Journal Supplement Series*, vol. 192, no. 2, p. 14, 2011.

[63] A. Kusaka, J. Appel, T. Essinger-Hileman, J. A. Beall, L. E. Campusano, H.-M. Cho, S. K. Choi, K. Crowley, J. W. Fowler, P. Gallardo, *et al.*, "Results from the atacama b-mode search (abs) experiment," *arXiv preprint arXiv:1801.01218*, 2018.

[64] A. Soliman, P. Ade, *et al.*, "Design and performance of single/wide band corrugated walls for the bicep array detector modules at 30/40 ghz," in *Millimeter, Submillimeter, and Far-Infrared Detectors and Instrumentation for Astronomy VIII*, International Society for Optics and Photonics, 2018.